Mix, A.C., Tiedemann, R., Blum, P., et al., 2003
Proceedings of the Ocean Drilling Program, Initial Reports Volume 202

7. SITE 1236[1]

Shipboard Scientific Party[2]

INTRODUCTION

Site 1236 (proposed Site NAZCA-10A) is located atop Nazca Ridge at 21°21.539′S, 81°26.165′W at a water depth of 1323 m. (Fig. **F1A**). This aseismic ridge, a fossil hotspot track with its modern expression at Easter Island, is especially well developed and shallow here at its intersection with the Nazca Fracture Zone.

The site occupies the center of a ~20-km-wide plateau that is punctuated by small volcanic spires that rise a few hundred meters above the relatively flat bathymetric surface (Fig. **F2**). These abrupt features likely represent small eroded remnants of an archipelago of volcanic islands that subsided below sea level after the site moved eastward over the active hotspot relatively early in its history. About 20 km southwest of Site 1236, a flat-topped guyot rises to within 350 m of present sea level. The presence of this relatively well-preserved, shallow bathymetric feature adjacent to the deeper, more eroded surface suggests multiple episodes of volcanism or the presence of a younger carbonate reef system that grew atop the volcanic edifice.

Nazca Ridge is covered with sediment to its shallowest reaches. The total thickness of the sedimentary section at Site 1236 is estimated to be 200 m based on site-survey seismic profiles (Fig. **F3**). The pelagic sequence reveals well-stratified strong reflective layers from the sediment surface to ~60 meters below seafloor (mbsf) and moderate reflective layers from ~60 to ~120 mbsf. Farther below to ~200 mbsf, deformed but almost continuous layers of moderate reflection are believed to smooth the relief of the acoustic basement.

Basement ages are expected to be between 30 and 35 Ma, based on magnetic anomalies of the surrounding oceanic crust (Cande and Haxby, 1991). If we assume that the Nazca Ridge was formed at the Easter Island hotspot, then the age difference between the basement of the ridge plateau and adjoining plate may only be a few million years. Tri-

F1. Sites 1236 and 1237 and oceanographic features off Peru and northern Chile, p. 23.

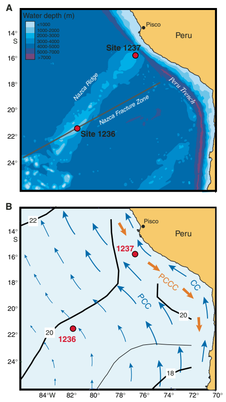

F2. High-resolution swath bathymetry at Site 1236, p. 24.

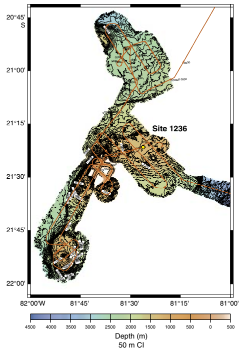

F3. Seismic profile at Site 1236, p. 25.

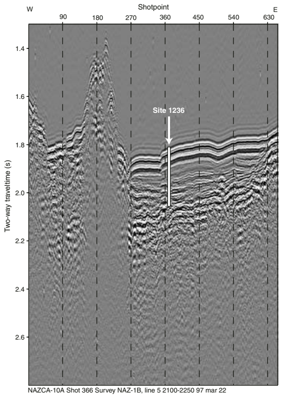

---

[1] **Examples of how to reference the whole or part of this volume.**
[2] **Shipboard Scientific Party addresses.**

Ms 202IR-107

ple coring at Site 1236 with the advanced piston corer (APC) therefore had the potential of providing a continuous pelagic record of 200 m that spans the entire Neogene and possibly the uppermost part of the upper Oligocene.

The tectonic backtrack path on the Nazca plate moves Site 1236 ~20° westward, approximately parallel to its modern latitudinal position (Fig. F4). Thermal subsidence would predict that the site was at shallower water depths during the early Miocene and perhaps was exposed above sea level very early in its history. Such subsidence is consistent with bathymetric evidence for erosion of the plateau surface. The implications of a late stage of volcanism (as suggested by the presence of shallower well-preserved guyots in the region) to paleobathymetric history are unknown.

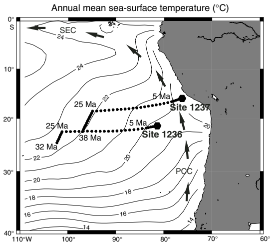
F4. Tectonic backtrack of Site 1236, p. 26.

Today, Site 1236 is situated near the western edge of the northward-flowing Peru-Chile Current (Fig. F1B). Its position relatively far from the productive upwelling systems places it in a modern oligotrophic region of the subtropical gyre. Plate tectonic backtrack locations can be used to predict general features of paleoceanographic change at Site 1236 under assumption that the modern overall conditions in the region remained almost constant through time and the only change in the system is drift of the site location (Fig. F5) relative to this fixed oceanographic background. In this analysis we ignore the relatively small changes in the position of the South American margin through time. Sampling of modern oceanographic atlas (Ocean Climate Laboratory, 1999) values at the paleosite locations suggests that 25 m.y. ago, sea-surface temperatures at Site 1236 should have been ~3°C higher (and salinities 0.6 psu higher) than today. Sea-surface nutrient concentrations would have been generally lower at the site location 25 m.y. ago than today, although it appears that the relative concentrations of silicate, nitrate, and phosphate at the sea surface vary somewhat differently along the backtrack path. Modern primary productivity roughly follows sea-surface silicate concentrations along this path and implies that primary productivity would have been ~50% lower 25 m.y. ago than at present. Thus, we expect lower biogenic sedimentation rates and relatively minor amounts of terrigenous sediment with greater age at Site 1236, with the exception of volcanics or shallow-water sediments early in the site's history. Significant deviations from these general trends, if detected in the sediment cores, would imply changes in regional oceanographic conditions or errors in the tectonic backtrack model.

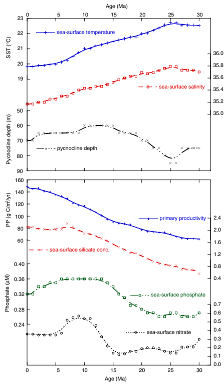
F5. Modern ocean properties at backtrack locations of Site 1236, p. 27.

The modern water depth of Site 1236 reflects the transition zone between the northernmost extension of oxygen-enriched (nutrient depleted) Antarctic Intermediate Water (AAIW) and the deeper oxygen-depleted (nutrient rich) Pacific Central Water (PCW). Its tectonic backtrack to shallower depths suggests that it may have been bathed in AAIW (or its paleoequivalent) during much of Miocene time (Fig. F6).

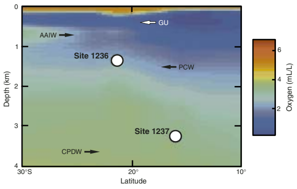
F6. Meridional cross section of water masses, p. 28.

The primary objectives at Site 1236 were to provide a continuous sedimentary sequence of the Neogene and Quaternary to

1. Improve on regional Neogene timescales by combining magnetostratigraphy, biostratigraphy, and isotopic stratigraphy (and perhaps orbital tuning) in a region midway between the tropical and high-latitude systems;
2. Assess climate changes of the southern subtropical Pacific over the past ~30 m.y., focusing on major intervals of changing climate (e.g., the early Miocene intensification in Antarctic glacia-

tion [~24 Ma], the middle Miocene climatic optimum [14–15 Ma], the glaciation of the East Antarctic Ice Sheet [~13 Ma], and the mid-Pliocene intensification of Northern Hemisphere glaciation [3.1–2.6 Ma]);

3. Examine the late Miocene to early Pliocene reorganization in South Pacific surface and intermediate water circulation in response to the closure of the Isthmus of Panama (10–4 Ma); and
4. Reconstruct changes in the boundary between PCW and AAIW (or in older intervals, the core of AAIW), in a subtropical area away from the continental margin, where primary production is low.

OPERATIONS

The 980-nmi voyage to Site 1236 (proposed Site NAZCA-10A) was accomplished in 86.0 hr at an average speed of 11.3 kt. The 3.5-kHz precision depth recorder (PDR) was used as a final check of site characteristics by comparison with precruise survey data. The vessel was on station at 1345 hr on 22 April 2002.

Hole 1236A

The drill string was deployed to a depth of 1309 meters below rig floor (mbrf), and Hole 1236A was initiated with the APC at 1815 hr on 22 April. The seafloor depth inferred from the recovery of the first core was 1334.9 mbrf. This value was 3.5 m shallower than the corrected PDR depth. Piston coring deepened the hole until Core 20H failed to achieve a full stroke at 173.1 mbsf. The recovery for the APC interval was 169.6 m (recovery = 98%) (Table T1). The nonmagnetic core barrel was used on all even-numbered cores (Table T1). Cores were oriented starting with Core 4H. Downhole temperature measurements were taken with the APC temperature (APCT) tool (Table T1). Coring in Hole 1236A continued with the extended core barrel (XCB) system to 207.7 mbsf, where the rate of penetration slowed markedly. XCB coring penetrated 34.6 m and recovered 27.4 m (recovery = 79%). A total of 207.7 m was cored and 197.2 m was recovered (Table T1) in Hole 1236A. The bit was pulled free of the seafloor at 1340 hr on 23 April.

T1. Operations summary, Site 1236, p. 58.

Hole 1236B

The vessel was moved 10 m west relative to Hole 1236A. Prior to coring in Hole 1236B, a bottom water temperature measurement was obtained with the APCT tool and the bit just above the seafloor. To obtain the desired stratigraphic overlap with the first hole, the bit was then positioned at 1333 mbrf and Hole 1236B was initiated with the APC at 1456 hr. The seafloor depth inferred from the recovery of the initial core was 1333.7 mbrf. Thirteen piston cores advanced to 122.8 mbsf.

When the driller attempted to cut Core 14H, the pressure in the drill string could not be raised above 2000 psi. The barrel was retrieved and the liner was found to be deformed, indicating that a large differential pressure had been applied across the liner. After two more coring attempts and an attempt to force the presumed obstruction out of the bottom-hole assembly (BHA), the drill string was retrieved. The flapper in the float valve was found resting on the bottom of the float valve assembly. Both hinges on the flapper had failed. The broken flapper prevented the end of the core barrel from entering the throat of the bit, causing the core barrel to land high in the BHA. These prevented a proper piston seal, and the firing pressure of 2700–2800 psi could not be achieved.

A total of 122.8 m was cored and 125.1 m was recovered (Table T1) in the aborted hole. The nonmagnetic core barrel was deployed with the odd-numbered cores. Cores were oriented starting with Core 3H. Downhole temperature measurements were taken at depths summarized in Table T1. All temperature measurements combined yielded a thermal gradient of ~3.9°C/100 m for Site 1236.

Hole 1236C

The vessel was offset 10 m west relative to Hole 1236B. At 1303 hr on 24 April, Hole 1236C was initiated with the APC, and the bit was positioned at 1336.5 mbrf (2.8 mbsf relative to Hole 1236B). Because this hole was initiated below the seafloor, the seafloor depth calculated from the previous hole was used (1333.7 mbrf). Piston coring advanced to the APC refusal depth of 167.3 mbsf). The nonmagnetic core barrel was deployed on every even-numbered core. The cores were oriented starting with Core 3H. Core 16H (145.3–154.8 mbsf) had to be drilled over. Of the 164.5 m cored, 167.7 m was recovered (recovery = 102%) (Table T1).

The vessel was secured for transit and left location at 0500 hr on 25 April.

COMPOSITE SECTION

We built a meters composite depth (mcd) scale to 222.89 mcd and a splice (as defined in **"Composite Section,"** p. 4, in the "Explanatory Notes" chapter) that ranges from the top of Core 202-1236C-1H to the bottom of Section 202-1236C-12H-7 (0–129.72 mcd) (see Tables T2, T3). Below Core 202-1236C-12H, little correlation exists between multisensor track (MST) measurements of magnetic susceptibility (MS), natural gamma ray (NGR), gamma ray attenuation (GRA) bulk density, or archive multisensor track (AMST) measurements of reflectance made in cores from different holes. Therefore, below Cores 202-1236A-12H, 202-1236B-12H, and 202-1236C-12H (131.44–223.19 mcd), cores were appended according to the cored interval, if nominal recovery was <100%, or to the recovered interval, if recovery was >100%.

The mcd scale and the splice are based on the stratigraphic correlation of split-core reflectance (a*) collected at 2.5-cm intervals using the AMST and whole-core MS measurements collected at 2.5-cm intervals using the MST. Measurements of magnetic susceptibility were also made with the OSU Fast Track (OSUS) using a 10-s integration time (Tables T4, T5), but because of some technical problems the MST-MS data were used here. No OSUS data are available from Hole 1236A, and partial data are available from Hole 1236B, starting at Section 202-1236B-7H-1. MS and a* data for Holes 1236A, 1236B, and 1236C and the splice constructed from them are presented on the mcd scale in Figures F7 and F8, respectively. The splice tie points (Table T3) were then used to construct representative spliced records for reflectance (L*, a*, and b*), MST-MS, and GRA bulk density data. The spliced records of reflectance (a*), GRA, and MS are presented in Figure F9.

T2. Composite depth scale, Site 1236, p. 59.

T3. Splice tie points, p. 60.

T4. OSUS-MS measurements, Hole 1236B, p. 61.

T5. OSUS-MS measurements, Hole 1236C, p. 62.

F7. MST-MS vs. mcd, p. 29.

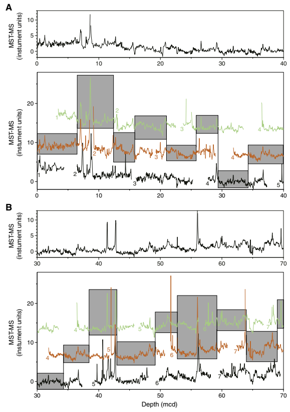

F8. Reflectance (a*) vs. mcd, p. 33.

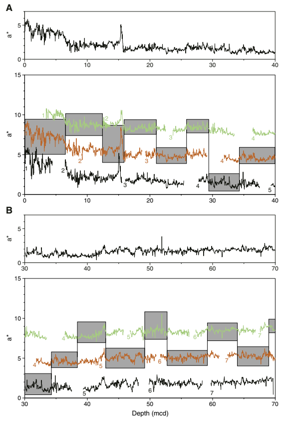

F9. Spliced records of a*, GRA density, and MST-MS, p. 37.

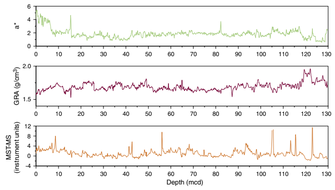

Reflectance (a*) was the most useful stratigraphic tool for correlation at Site 1236. We assumed that the uppermost sediment (the "mudline") in Core 202-1236C-1H was the sediment/water interface. A mudline was also recovered in Core 202-1236B-1H, which confirmed the fidelity of the top of the recovered section. Core 202-1236C-1H, the "anchor" in the composite depth scale, is the only core with depths that are the same on the mbsf and mcd scales. From this anchor we worked downhole, correlating records on a core-by-core basis. A comparison of the mcd and mbsf depth scales (Fig. **F10**) shows that the mcd scale is on average 14% longer than the mbsf scale.

F10. A comparison of the mbsf and mcd scales, p. 38.

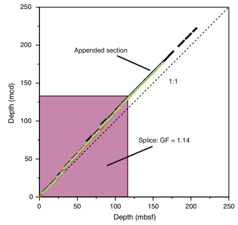

To facilitate the calculation of mass accumulation rates (MARs), we provide corrected meters composite depth in Table **T2** and in Table **T3** for depths within the splice. The mcd growth factor for the spliced interval at Site 1236 is 1.14.

LITHOSTRATIGRAPHY

At Site 1236, sediment was cored in three holes to 222.8 mcd (207.7 mbsf) in Hole 1236A, 136.7 mcd (122.8 mbsf) in Hole 1236B, and 180.9 mcd (167.3 mbsf) in Hole 1236C. Basaltic breccia (inferred basement) was reached at 222.3 mcd in Hole 1236A. The sediments at Site 1236 are primarily calcareous, with pelagic oozes predominant in the uppermost ~156 mcd. Farther downhole, nonpelagic grains become increasingly abundant except for the lowermost ~14 mcd, which is pelagic, primarily consisting of chalk.

T6. Lithologic units, p. 63.

F11. Lithostratigraphic summary, p. 39.

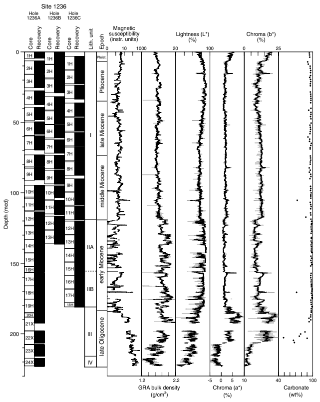

The sedimentary sequence at Site 1236 was subdivided into four major lithologic units (Units I–IV) with two subunits in Unit II (Table **T6;** Fig. **F11**). Unit I contains nannofossil ooze, which is rich in foraminifers, and partly clay bearing. Magnetic susceptibility decreases and lightness increases downhole to ~35 mcd. Unit II sediments primarily consist of nannofossil ooze (Subunit IIA) and unlithified mudstone (Subunit IIB), both partly foraminifer bearing and with numerous intercalations of nonpelagic calcareous sediments. The grain content varies significantly with intervals of unlithified packstone to rudstone and wackestone to floatstone. These lithologies often are present in fining-upward sequences. We distinguished two subunits in Unit II based on the transition from nannofossil-dominated to micrite-dominated sediments. Unit II is characterized by higher GRA bulk density and lightness as well as lower and more variable magnetic susceptibility when compared to Unit I. Coarse-grained nonpelagic calcareous sediments, partly glauconitic, predominate in Unit III. Unit IV includes a multicolored sequence of calcareous chalk with increased amounts of glauconite. Metalliferous sediments with volcanic glass lie directly above the basement, which consists of a basaltic drilling breccia. Magnetic susceptibility increases strongly downhole in Units III and IV, corresponding to decreasing lightness. Bulk density, grain density, and porosity measurements for all units are shown in Figure **F12.**

F12. Moisture and density, p. 40.

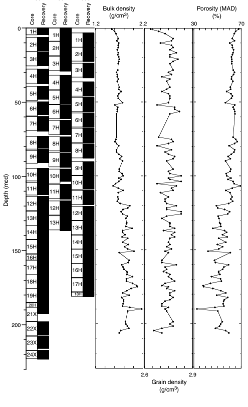

Description of Lithologic Units

Lithologic units are primarily defined by visual core description, smear slide examination, GRA bulk density, color reflectance, and magnetic susceptibility measurements. Calcium carbonate concentrations provided additional support.

Unit I

Intervals: Core 202-1236A-1H through Section 12H-5, 0 cm; Core 202-1236B-1H through Section 13H-2, 69 cm; and Core 202-1236C-1H through Section 11H-7, 56 cm
Depths: Unit I: 0–119.5 mcd; Hole 1236A: 0–105.6 mbsf; Hole 1236B); 0–106.0 mbsf; and Hole 1236C) 2.8–106.9 mbsf
Age: Pleistocene to early Miocene (0 to ~17 Ma)

Unit I is characterized by calcareous pelagic oozes of Pleistocene, Pliocene, and Miocene age. The major lithology defining Unit I is nannofossil ooze, which is rich in foraminifers and partly clay bearing (Table T6). Carbonate concentrations are generally >90 wt% (Figs. F11, F13). Sediments of Unit I display little visual variability and few sedimentary structures. Sediment color ranges from very pale brown to white with occasional light gray intervals. Color changes are typically subtle and gradational. Pale brown intervals often display color mottling, which indicates moderate bioturbation. Some of the mottles have dark halos that reveal the presence of finely dispersed iron sulfides.

The biogenic fraction is dominated by nannofossils; discoasters are abundant below 32 mcd. Nannofossil contents are ~50% in the uppermost ~15 mcd, increase to a maximum (>90%) between ~50 and 63 mcd, and gradually decrease to the bottom of Unit I (Fig. F13). Micrite, probably originating from the in situ recrystallization of nannofossils, becomes a significant component of the major lithology below ~90 mcd. Foraminifer contents decrease from >25% in the uppermost ~10 mcd to a few percent around 50 mcd. The lower half of Unit I is characterized by highly variable foraminifer contents averaging ~10%–15% (Fig. F13).

Siliciclastic components are mainly clay minerals, which are variable throughout Unit I. The clay mineral abundance decreases from values of ~10%–20% in the uppermost ~15 mcd to a minimum of negligible content between ~50 and 60 mcd. Farther downhole, the clay mineral abundance varies over a range of ~5%–15% (Fig. F13). Within the siliciclastic component, fine silt–sized feldspar and pyroxene are present in a few samples. Authigenic minerals include trace amounts of pyrite and iron oxides.

Two isolated layers rich in nonpelagic calcareous grains (primarily peloids) at ~65 and 99 mcd (Fig. F14), classified as unlithified wackestone, are a notable minor lithology in Unit I. Additionally, several volcanic ash layers are present, most of which can be correlated across the three holes. The ash layers appear as brownish intervals with a fairly sharp bottom and a gradational top (Fig. F15). They contain primarily brown glass and admixtures of the surrounding sediments. One layer at a depth of ~105 mcd consists of pale glass and minor amounts of biotite, pyroxene, and feldspar. An interval rich in volcanic ash from ~82 to 84 mcd is characterized by increased siliceous microfossil contents, primarily diatoms (see "Diatoms," p. 14, in "Biostratigraphy"), which are otherwise only occasionally present in trace amounts in Unit I (Fig. F13).

The magnetic susceptibility of Unit I sediments is low (<10 instrument units) (Figs. F11, F16) and decreases from the top of the section to ~35 mcd, roughly paralleling the decrease in siliciclastics and a slight increase in calcium carbonate concentrations (Fig. F13). Likewise, lightness increases downhole within this interval, whereas a* and b* decrease (Figs. F11, F16). In the a*-b* color space, all color measurements

F13. Major components, carbonate, and magnetic susceptibility, p. 41.

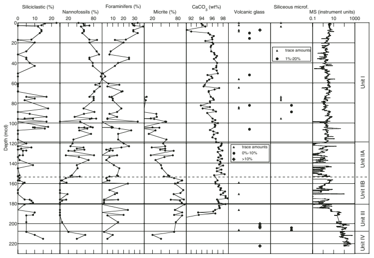

F14. Uppermost nonpelagic grain–rich layer in Unit I, p. 42.

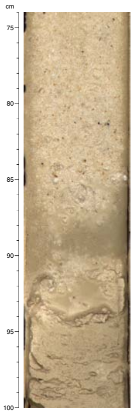

F15. Volcanic ash layer, p. 43.

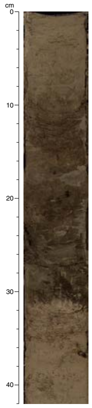

F16. Magnetic susceptibility, GRA bulk density, and L*, p. 44.

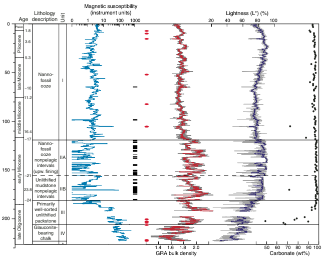

of Unit I sediments plot in the "yellow" domain (Fig. F17). The interval above ~35 mcd that is enriched in siliciclastic material is characterized by the highest a* and b* values (Fig. F17B).

Isolated maxima in the magnetic susceptibility mostly correspond to volcanic ash layers. The two layers rich in nonpelagic calcareous materials appear as susceptibility minima. Additional minima are probably disturbed intervals and/or section breaks.

F17. Color measurements plotted in the a*-b* color plane, p. 45.

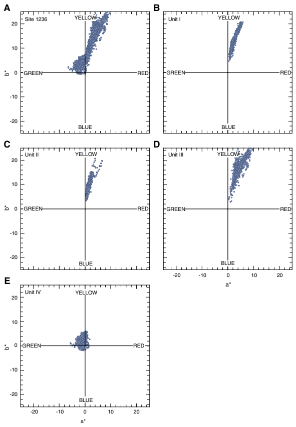

Unit II

Intervals: 202-1236A-12H-5, 0 cm, through 19H-4, 100 cm; 202-1236B-13H-2, 69 cm, through 13H-CC, 18 cm; and 202-1236C-12H-7, 56 cm, through 18H-CC, 21 cm
Depths: Unit II: 119.5–181.0 mcd; Hole 1236A: 105.6–166.1 mbsf; Hole 1236B: 106.0–122.8 mbsf; and Hole 1236C: 106.9–167.3 mbsf
Age: early Miocene to late Oligocene (~17–24 Ma)

Unit II is characterized by two major lithologies, pelagic and nonpelagic calcareous sediments. Pelagic sediments consist of nannofossil ooze and unlithified mudstone, both of which are partly foraminifer bearing. Nonpelagic sediments are present as abundant intercalations of nonskeletal and/or skeletal grain-rich intervals classified as unlithified wackestone, packstone, and grainstone (Table T6; Fig. F18). Grains are primarily coarse silt and sand sized, except for occasional intervals of unlithified floatstone and rudstone in which the grains reach >2 mm (Fig. F18). The transition to the overlying fine-grained calcareous sediments is gradational. The thickness of nonpelagic grain–rich intervals varies from meters to decimeters (Fig. F18). These intervals constitute ~60% of Unit II.

F18. Fining-upward sequence of unlithified rudstone to wackestone, p. 46.

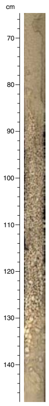

Nonskeletal grains are mostly peloids. Skeletal grains are present as bioclasts, primarily recrystallized benthic foraminifers, bryozoan fragments, and some remains and encrustations of red algae (Fig. F19). Calcium carbonate concentrations are >95 wt% throughout Unit II. Foraminifer contents vary but mostly range from ~10% to 20%. Sediments of Unit II lack siliceous microfossils and contain only minor to trace amounts of clay and extremely rare silt-sized siliciclastic minerals (Fig. F13). Volcanic glass is present in trace amounts, and no distinct ash layers were identified.

F19. Skeletal grain-rich rudstone, p. 47.

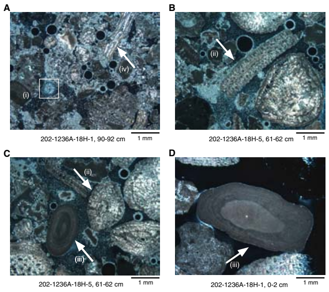

Unit II is clearly distinguishable by physical properties. GRA bulk density and lightness are higher in Unit II sediments than in Unit I, reflecting the increase in nonpelagic grain–rich intervals (Fig. F16). These intervals are also characterized by low magnetic susceptibility (Fig. F16). In the a*-b* color space, all color measurements of Unit II sediments plot in the "yellow" domain within a very narrow range (Fig. F17C).

Unit II is subdivided into two subunits, primarily on the basis of the relative abundance of pelagic microfossils vs. micrite. The subdivision is not clearly defined by physical properties.

Subunit IIA

Intervals: 202-1236A-12H-5, 0 cm, through 16H-1, 85 cm; 202-1236B-13H-2, 69 cm, through 13H-CC, 18 cm; and 202-1236C-12H-7, 56 cm, through 15H-5, 0 cm

Depths: Subunit IIA: 119.5–153.3 mcd; Hole 1236A: 105.6–138.5 mbsf; Hole 1236B: 106.8–122.8 mbsf; and Hole 1236C: 106.9–140.3 mbsf
Age: early Miocene (~17–21 Ma)

Subunit IIA is primarily foraminifer-bearing nannofossil ooze (Table T6). Micrite increases downhole as nannofossil abundance decreases. Micrite in Subunit IIA most likely originates from in situ recrystallized nannofossils. The sediment color of the pelagic oozes is primarily very pale brown to white with gradational color changes, except for sporadic mottling indicating intervals of moderate bioturbation. The nonpelagic grain–rich intervals are predominantly white.

Subunit IIB

Intervals: 202-1236A-16H-1, 85 cm, through 19H-4, 100 cm, and 202-1236C-15H-5, 0 cm, through 18H-CC, 21 cm.
Depths: Subunit IIB: 153.3–180.9 mcd; Hole 1236A: 138.5–166.1 mbsf; and Hole 1236B: 140.3–167.3 mbsf.
Age: early Miocene to late Oligocene (~21–24 Ma)

Sediments of Subunit IIB are macroscopically similar to those of Subunit IIA, except that the lower portions of nonpelagic grain–rich intervals more frequently contain nonpelagic grains >2 mm (unlithified rudstone and floatstone) (Figs. F18, F19). The major distinction between Subunits IIA and IIB is the dominance of micrite and the near absence of nannofossils in Subunit IIB. Micrite in the matrix of unlithified mudstones most likely originates from both in situ recrystallization of nannofossils and allochthonous supply together with the nonpelagic grains.

Unit III

Interval: 202-1236A-19H-4, 100 cm, through 22X-CC, 40 cm
Depths: 181.0–207.7 mcd (166.1–192.5 mbsf)
Age: late Oligocene (>24 Ma)

Unit III is characterized by nonpelagic grain–rich calcareous sediments, primarily unlithified packstone and less abundant unlithified rudstone. Unlithified packstones are dominated by well-sorted sand-sized grains (Fig. F20), which are primarily peloids and skeletal grains (recrystallized benthic foraminifers, bryozoan fragments, and some remains and encrustations of red algae). Unlithified rudstones typically fining upward to unlithified packstones. Sediment color varies but is predominantly pale yellow. Unit III sediments lack nannofossils and contain abundant micrite and variable minor amounts of benthic foraminifers (Fig. F13). Siliciclastic components include minor amounts of clay minerals and rare feldspar.

F20. Unlithified packstones with authigenic glauconite, p. 48.

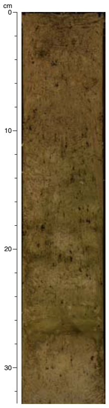

Minor lithologies in Unit III are intervals with pale yellow-brown and greenish gray layers that are increasingly abundant downhole. These are relatively rich in siliciclastic components (up to ~35%, primarily clay mineral and minor amounts of feldspar and pyroxene), volcanic ash, and/or authigenic glauconite. Three volcanic ash layers consisting of up to 80% volcanic glass (partly palagonized) are present near the base of Unit III. Abundant siliceous microfossils (up to 18%) consisting of spicules and diatoms are present in this interval (Fig. F13).

Downhole, carbonate concentrations and lightness decrease significantly and magnetic susceptibility increases (Figs. F11, F16). In the a*-

b* color space, all color measurements of Unit III sediments plot in the "yellow" domain (Fig. **F17D**) with higher variability than in Units I and II. Downhole variations of a* and b* are consistent with increasing abundance of authigenic glauconite, siliciclastic, and volcaniclastic material (Figs. **F11, F13, F16**).

Unit IV

Interval: 202-1236A-23X-1, 0 cm, through 24X-4, 45 cm
Depths: 207.7–222.3 mcd (192.5–207.2 mbsf)
Age: late Oligocene (>24 Ma)

Unit IV represents a complex succession of sediments directly overlying the basaltic basement at 222.3 mcd. Firm to indurated chalk is the dominant lithology in this unit. The chalk is characterized by abundant nannofossils (partly recrystallized in situ to micrite) and small amounts of foraminifers (Fig. **F13**). Authigenic glauconite is present throughout the unit and reaches up to ~50%, producing a range of greenish hues within decimeter-scale intervals. Centimeter-scale color banding of different greenish hues is present in Core 202-1236A-23X and the upper sections of Core 24X (Fig. **F21**). *Zoophycos* trace fossils were observed, particularly in Core 202-1236A-23X. Sediments directly overlying the basaltic basement are reddish brown and contain abundant iron oxides and reworked basalt fragments, as well as ~10% volcanic glass.

F21. Glauconite-bearing chalk color banding, p. 49.

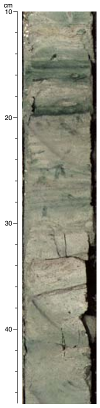

Magnetic susceptibility is high in Unit IV and increases downhole, and lightness decreases strongly over the same interval. In the a*-b* color space, almost all color measurements of Unit IV sediments plot in the "green" domain (Fig. **F17E**). These results are consistent with a significant siliciclastic and volcaniclastic component and the abundance of glauconite in Unit IV.

Interpretation and Depositional History

The primarily pelagic sedimentary sequence recovered at Site 1236 spans the entire Neogene and the uppermost part of the late Oligocene. The depositional history of the site (Fig. **F22**) is consistent with its tectonic backtrack path and is related to the evolution of the Nazca Ridge.

F22. Summary of depositional history, Site 1236, p. 50.

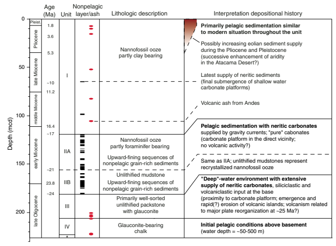

The fine-grained sediment, abundant nannofossils, and trace fossils suggest a low-energy pelagic depositional environment for Unit IV directly overlying the basement, without indications of any input of nonpelagic calcareous material. The presence of authigenic glauconite indicates water depths below the typical storm wave base to a maximum of 500 m (Fairbridge, 1967; Porrenga, 1967) during initial deposition. This depth constraint agrees with the range of paleowater depths calculated from the assumed thermal subsidence of the basaltic basement since the late Oligocene (see **"Introduction,"** p. 1).

After the initial pelagic phase, a major event in the depositional history of Site 1236 was the emergence of volcanic islands in the vicinity of the site (probably represented by a bathymetric high located southeast of the site) (see **"Introduction,"** p. 1), which was likely related to a major plate reorganization that resulted in enhanced volcanic activity in the late Oligocene (~25 Ma) (Duncan and Hargraves, 1984). This event is documented by several volcanic ash layers near the base of Unit III and an abrupt lithologic shift to predominantly unlithified nonpelagic grain–rich calcareous sediments in Units II and III. These sediments suggest that the islands were surrounded by carbonate platforms that supplied neritic calcareous material to Site 1236. Although the dominance of well-sorted packstones with skeletal grains indicates the proximity of a nearshore high-energy environment, the presence of authigenic glauconite might also suggest relatively calm water conditions below the storm wave base (Fairbridge, 1967; Porrenga, 1967). Hence, the coarse-grained carbonates at Site 1236 were most likely supplied by gravity currents (supported by occasional fining-upward sequences) originating from nearby carbonate platforms during that time. The uphole decrease in siliciclastic and volcaniclastic constituents and the strong decrease in magnetic susceptibility point to the erosion of the volcanic island(s) during the late Oligocene, when sedimentation rates were highest at Site 1236 (~1 cm/k.y.) (see **"Age Model and Mass Accumulation Rates,"** p. 19).

At the base of Unit II (~24 Ma), sediments are nearly pure carbonates, indicating already submerged volcanic islands. The downslope supply of neritic calcareous material, however, continues into the Miocene sequence, indicating continued proximity to carbonate platforms, causing slightly higher sedimentation rates in Unit II (~1 cm/k.y.) compared to Unit I (~0.4–0.9 cm/k.y.) (see **"Age Model and Mass Accumulation Rates,"** p. 19). Fine-grained calcareous sediments, at least in Subunit IIA, are clearly pelagic, as evidenced by the abundance of nannofossils. These sediments are dominated by micrite in Subunit IIB, which is most likely the product of in situ nannofossil recrystallization. Hence, pelagic carbonate sedimentation was established in the early Miocene.

Pelagic calcareous oozes of Unit I represent conditions similar to modern (i.e., low surface) productivity and resulting low sedimentation rates (~0.4–0.9 cm/k.y.) within the southeastern Pacific subtropical gyre. Two isolated layers containing nonpelagic grains at depths of ~65 and ~98 mcd represent the latest supply of neritic sediments to Site 1236, indicating the final submergence of carbonate platforms in the late Miocene at ~10 Ma. The submergence of the carbonate platforms is most likely primarily controlled by thermal subsidence of the oceanic crust, as the middle Miocene is characterized by long-term sea level lowering (Exon, Kennett, Malone, et al., 2001).

Pliocene and Pleistocene sediments (~0–40 mcd) are slightly enriched in siliciclastic clay as also indicated by uphole increasing magnetic susceptibility and decreasing calcium carbonate concentrations. The minor siliciclastic fraction probably represents eolian supply from the South American Atacama Desert, assuming that prevailing wind directions were similar to the modern conditions. Our record might therefore indicate successive enhancement of aridity in South America and/or increasing wind speeds since the early Pliocene, possibly related to the uplift history of the Andes.

The dominance of brown volcanic glass in the ash layers present in Units I and III indicates a primarily basaltic composition consistent with an oceanic source of the ash layers. This volcanic activity is most likely related to both submarine and subaerial volcanic eruptions within the Nazca Ridge hotspot track. Volcanic glass in Unit IV probably originates from the reworking of basaltic basement. Volcanism might have been decreased or absent during the early Miocene, as Unit II lacks ash layers. One ash layer of intermediate composition, which might originate from the Andes, was recovered. Some ash layers and the surrounding sediment contain abundant siliceous microfossils, which points to selective preservation and/or episodic production of siliceous material (see **"Diatoms,"** p. 14, in "Biostratigraphy").

BIOSTRATIGRAPHY

Calcareous nannofossil and planktonic foraminifer biostratigraphies indicate that the 220-m upper Pleistocene to upper Oligocene sediment succession recovered at Site 1236 is essentially complete (Table T7; Figs. F23, F29). The presence of *Sphenolithus ciperoensis* and *Sphenolithus distentus,* along with other Oligocene taxa in Samples 202-1236A-23X-CC and 24X-CC (216.1–223.1 mcd), suggests a basal age of 27.5–29.9 Ma for this interval.

T7. Age-depth control points, p. 64.

Calcareous nannofossils are generally abundant and moderately to well preserved throughout the interval. Planktonic foraminifers are common to abundant down to ~150 mcd (19–20 Ma). Below this depth, foraminiferal abundance decreases and preservation deteriorates markedly. Benthic foraminiferal assemblages document an oligotrophic, pelagic environment from Pliocene to middle Miocene time. Older intervals contain higher numbers of buliminids and nodosariids, reflecting shallower water depth and proximity to the oxygen minimum zone. The presence of poorly preserved larger benthic foraminifers, which have modern equivalents that host algal endosymbionts, indicates redeposition from a nearby carbonate platform during the Oligocene and early Miocene.

F23. Calcareous nannofossils and planktonic and benthic foraminifers, Hole 1236A, p. 51.

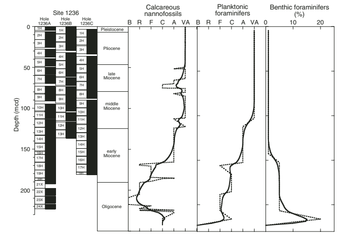

Diatoms are only found close to two ash layers at 82.3 and 206.7 mcd and indicate either increased diatom production near the time of ash deposition or anomalous preservation as a result of the presence of ash. A typical low-latitude diatom assemblage with an age between 13.5 and 12.5 Ma is present at 82.3 mcd. The assemblages from the two ash levels also include benthic and neritic diatoms that indicate redeposition from shallow-water environments.

Calcareous Nannofossils

Calcareous nannofossils are generally very abundant and well to moderately preserved at Site 1236 (Table T8; Fig. F23). Virtually no reworked nannofossil specimens were observed. Most of the standard nannofossil zonal markers, as well as some nonstandard markers, were recognized between core sections, which allows a relatively detailed nannofossil biostratigraphy for the entire sequence from the upper Oligocene to upper Pleistocene.

T8. Distribution of calcareous nannofossils, p. 65.

Sample 202-1236A-1H-1, 75 cm (0.78 mcd), contains a late Pleistocene assemblage dominated by *Gephyrocapsa* spp. The absence of *Emiliania huxleyi* and *Pseudoemiliania lacunosa* indicates Zone NN20 (0.24–0.46 Ma). The last occurrence (LO) of *P. lacunosa,* which defines the top of Zone NN20, is located between Samples 202-1236A-1H-1, 75 cm, and 1H-2, 75 cm (0.78–2.28 mcd). The LO and first occurrence (FO) of *Reticulofenestra asanoi* and *Gephyrocapsa* spp. large (>5.5 µm) and the LO of *Calcidiscus macintyrei* were recognized in the lower part of this core and allow subdivision of Zone NN19.

The topmost Pliocene datum, the LO of *Discoaster brouweri,* which defines the top of NN18 (1.96 Ma), is located between Samples 202-1236A-2H-1, 76 cm, and 2H-2, 75 cm (7.17–8.68 mcd). The next three standard zonal markers for the late Pliocene have been determined in the lower part of the same core: the LO of *Discoaster pentaradiatus* (base of Zone NN18; 2.44 Ma), between Samples 202-1236A-2H-3, 76 cm, and 2H-4, 76 cm (10.19–11.7 mcd); the LO of *Discoaster surculus* (base of Zone NN17; 2.61 Ma), also between Samples 2H-3, 76 cm, and 2H-4, 76 cm (10.19–11.7 mcd); and the LO of *Discoaster tamalis* (base of Subzone CN12b; 2.76 Ma), between Samples 2H-4, 76 cm, and 2H-5, 76 cm (11.7–13.22 mcd).

The late/early Pliocene boundary in terms of nannofossil biostratigraphy can generally be approximated by the LO of *Reticulofenestra pseudoumbilicus,* which is placed between Samples 202-1236A-3H-2, 76 cm, and 3H-3, 76 cm (18.1–19.61 mcd). Slightly below this boundary is another useful datum, the FO of *P. lacunosa* (4.0 Ma), which is located between Samples 202-1236A-3H-3, 76 cm, and 3H-4, 76 cm (19.61–21.12 mcd).

The LO of *Triquetrorhabdulus rugosus* (5.35 Ma), between Samples 202-1236A-5H-CC and 6H-1, 76 cm (48.17–50.54 mcd), may be an approximation for the Miocene/Pliocene boundary. A more widely used index for the top of the Miocene, *Discoaster quinqueramus,* was not found at this site. As the range of this species defines Zone NN11 (5.6–8.6 Ma), this means a significant hiatus if this standard zone is applied to this site. However, two nonstandard datums, the top of the *R. pseudoumbilicus* (>7 µm) "absence interval" and the FO of *Amaurolithus primus* (normally in this zone), were found to be present in succession, suggesting that a major hiatus probably does not exist here and the absence of *D. quinqueramus* may be a result of an anomalous biogeographic pattern in this part of the southeastern Pacific.

Abundant *Cyclicargolithus floridanus* was first encountered in Sample 202-1236A-8H-1, 79 cm (73.87 mcd), just one sample below the LO of *Coccolithus miopelagicus* and slightly above the LO of *Calcidiscus premacintyrei.* The relationship of the latter datum with that of the LO of *C. floridanus* is in a reverse sequence as indicated by Young (1998), and the age of the LO of *C. floridanus* appears to be over 1 m.y. younger at the site than previously thought.

The presence of *Sphenolithus heteromorphus* from Samples 202-1236A-9H-3, 76 cm, to 13H-3, 6 cm (85.41–131.8 mcd), indicates an age of 13.57 Ma for the top sample and an age of 18.2 Ma for the bottom sample. Similarly, the presence of *Sphenolithus belemnos* in Samples 202-1236A-13H-CC through 15H-3, 76 cm (132.9–146.4 mcd), firmly dates the interval as Zone NN3 (18.5–19.2 Ma).

Cores 202-1236A-16H through 22X (154.9–206.7 mcd) generally yielded rare to few poorly preserved nannofossils. However, the darker 20-cm interval from the top of Section 202-1236A-18H-4 contains abundant and moderately preserved nannofossils, which include such age-diagnostic species as *Reticulofenestra bisecta, Zygrhabdolithus bijugatus,* and *S. distentus.* This suggests an age of 23.9–24.75 Ma for the interval. No mixture of taxa of discordant ages was observed in any of the samples examined from this interval. Furthermore, the sample immediately below the darker interval and within the white carbonate sediment (Sample 202-1236A-18H-4, 25 cm; 170.7 mcd) also contains the Oligocene taxa *R. bisecta* and *Z. bijugatus*. The presence of these taxa indicates that the darker interval is most likely in situ, and it may represent a time interval with substantially less supply of shallower-water carbonate material from nearby carbonate platforms. The abruptness of this change is remarkable.

The last two core catcher samples (Samples 202-1236A-23X-CC and 24X-CC; 216.1–223.1 mcd) contain both *S. ciperoensis* and *S. distentus* along with other late Oligocene taxa and, thus, clearly belong to Zone NP24 (27.5–29.9 Ma), which straddles the lower/upper Oligocene boundary.

Planktonic Foraminifers

Planktonic foraminifers are abundant to common down to ~135.3 mcd (Cores 202-1236A-1H through 15H), but abundance decreases in the lower part of Hole 1236A (Table T9; Fig. F23). Preservation is good to that depth but deteriorates markedly below this level, and carbonate cement and recrystallized overgrowths frequently obscure test features. Sample 202-1236A-24X-CC (223.07 mcd) is barren. The FOs and LOs of marker species allow a preliminary biostratigraphy to be established for the entire Pleistocene–Miocene succession recovered at this site. However, Oligocene biozones were not recognized because of the generally poor preservation of planktonic foraminifers within this interval.

T9. Distribution of foraminifers, p. 68.

Pleistocene (Sample 202-1236A-1H-CC; 4.60 mcd)

The well-preserved Pleistocene planktonic foraminiferal assemblage includes *Globigerina bulloides, Globigerina falconensis, Globigerina quinqueloba, Globigerinoides ruber, Globigerinita glutinata, Globorotalia scitula, Globorotalia tosaensis, Globorotalia truncatulinoides, Globorotalia tumida, Orbulina universa,* and *Neogloboquadrina dutertrei*. Sample 202-1236A-1H-CC is placed in the lower Pleistocene Subzone Pt1a of Berggren et al. (1995) (Fig. F12, p. 63, in the "Explanatory Notes" chapter), based on the presence of *Globorotalia inflata, G. tosaensis,* and *G. truncatulinoides* and the absence of *Globigerinoides extremus*.

Pliocene (Samples 202-1236A-2H-CC through 4H-CC; 15.51–37.52 mcd)

The presence of *Sphaeroidinellopsis seminula,* with *G. extremus, G. tosaensis,* and *Dentoglobigerina altispira,* in Sample 202-1236X-2H-CC indicates upper Pliocene Zone Pl4. Samples 202-1236A-3H-CC and 4H-CC are assigned to lower Pliocene Zone Pl1, based on the presence of *Globoturborotalia nepenthes, G. tumida,* and *Globorotalia margaritae.*

Miocene (Samples 202-1236A-5H-CC through 18H-CC; 48.17–175.4 mcd)

Samples 202-1236A-5H-CC and 6H-CC contain *Globorotalia conomiozea, Globorotalia menardii, Globorotalia plesiotumida, G. nepenthes, D. altispira, O. universa, Sphaeroidinellopsis kochi,* and *S. seminula,* which indicate upper Miocene Zones M14–M13. The upper part of Core 202-1236A-7H is also probably of late Miocene age; however, this could not be determined by shipboard studies as a result of low-resolution sampling. Samples 202-1236A-7H-CC through 11H-CC are characterized by a relatively diverse assemblage including *Globoquadrina dehiscens, D. altispira,* and *S. seminula*. The FO of *Orbulina suturalis* and *Praeorbulina sicana* can be placed between Samples 202-1236A-9H-CC and 10H-CC and between Samples 11H-CC and 12H-CC, respectively, indicating the middle Miocene Zone M5 for this interval. The FO of *G. dehiscens,* between Samples 202-1236A-18H-CC and 19H-CC and the LO of *Globoturborotalia angulisuturalis* between Samples 17H-CC and 18H-CC indicate the lower Miocene Subzone M1b. The absence of some standard middle and early Miocene zonal markers in the shipboard samples examined probably reflects the low sedimentation rates at this site and the low-resolution sampling. The FO of *G. angulisuturalis* (29.4 Ma) occurs between Samples 202-1236A-20H-CC and 21H-CC. However, because of the poor preservation of the lowermost samples, it is impossible to ascertain whether this is truly the true FO of the taxon.

Benthic Foraminifers

Benthic foraminifers are rare in the upper part of Hole 1236A, and the benthic/planktonic foraminiferal ratio is extremely low (<1% of total foraminifers) down to 142.67 mbsf (Cores 202-1236A-1H through 14H) (Table T9). Below this depth, the proportion of benthic foraminifers increases to 5% and reaches 20% in Sample 202-1236A-23X-CC (216.07 mcd) (Fig. F23). Sample 202-1236A-24X-CC (223.07 mcd) is barren. Preservation is good to moderate down to 137.9 mbsf (Cores 202-1236A-1H through 15H) but deteriorates below this depth in Hole 1236A.

The Pleistocene–middle Miocene assemblage is relatively diverse and characterizes an oligotrophic pelagic environment. Characteristic taxa are *Cibicidoides mundulus, Globocassidulina subglobosa, Gyroidinoides soldanii, Gyroidinoides orbicularis, Laticarinina pauperata, Melonis affinis, Oridorsalis umbonatus, Planulina wuellerstorfi, Pullenia bulloides, Pyrgo murrhina, Rectuvigerina striata, Siphonina tenuicarinata, Stilostomella abyssorum, Stilostomella subspinosa,* and *Vulvulina spinosa.*

A decrease in water depth from middle bathyal in the Pleistocene–middle Miocene to upper bathyal or shelf during the early Miocene and late Oligocene is registered by a change in assemblage composition. Below 175.4 mcd (Cores 202-1236A-18H through 23X), buliminids and nodosariids become more abundant and are present together with shallow-water forms such as *Rosalina* and *Palliolatella*. Coarser layers within this interval often show grading (see Fig. F19 and **"Lithostratigraphy,"** p. 5) and contain large abraded tests of *Lenticulina* with rusty staining and poorly preserved large symbiont-bearing foraminifers (mainly alveolinids and soritinids). Their presence, together with robust bryozoan fragments, indicates redeposition from a nearby carbonate platform, probably in a cool subtropical climate.

Diatoms

All core catchers and split sections examined for diatoms at Site 1236 were barren, with the exception of Samples 202-1236A-9H-1, 64 cm, and 9H-1, 66 cm (82.3 mcd), where diatoms are frequent, and 22X-CC (206.7 mcd), where their presence is rare. The fact that both these levels are present above ash layers and, in the case of Core 202-1236A-9H, that diatoms disappear 5 cm above the referred ash layer, might be indicative of selective preservation because of increased silica in the sediment pore waters. However, three other ash-layer intervals were examined (intervals 202-1236A-23X-5, 29–31 cm [214.0 mcd]; 8H-6, 110–150 cm [82.0–82.4 mcd]; and 11H-7, 46–57 cm [114.9–115.0 mcd]), and none of them contained diatoms. This points to increased diatom production at the time of deposition of the sediments at 82.3 and 206.7 mcd.

Samples 202-1236A-9H-1, 64 and 66 cm (82.3 mcd), contain a typical middle Miocene low-latitude diatom assemblage including *Actinocyclus moronensis, Actinocyclus ellipticus, Rossiela paleacea* s.l., *Coscinodiscus lewisianus, Denticulopsis simonsenii* s.s., and *Denticulopsis nicobarica.* The presence of *A. ellipticus, A. moronensis,* and *C. lewisianus* and the absence of *Cestodiscus peplum* in this sample assign it to the *C. lewisianus* Zone, with an age between 13.51 and 12.47 Ma.

For Sample 202-1236A-22X-CC (206.7 mcd), no age assignment can be made based on the rare specimens observed.

Benthic and neritic diatoms are also found in Samples 202-1236A-9H-1, 64 and 66 cm (82.3 mcd), and 22X-CC (206.7 mcd). The presence of benthic and neritic forms suggests shallow-water, possibly shelf, conditions close to the drilled site.

PALEOMAGNETISM

Natural Remanent Magnetization

The natural remanent magnetization (NRM) of whole-round sections from Cores 202-1236A-1H through 20H and 202-1236B-1H through 9H was measured to help facilitate hole-to-hole correlation. The NRM of archive-half sections of each core was remeasured after alternating-field (AF) demagnetization at selected levels. Core 202-1236A-1H was demagnetized at peak alternating fields of 10, 15, and 20 mT. Section 202-1236A-1H-3 was additionally demagnetized at 25 mT. Core 202-1236A-2H was demagnetized at 15 and 20 mT. Section 202-1236A-2H-6 was additionally demagnetized at 25 mT. Core 202-1236A-3H was demagnetized at 15, 20, and 25 mT. Cores 202-1236A-4H through 24X, all cores from Hole 1236B, and Cores 202-1236C-1H through 11H were demagnetized at 20 and 25 mT. Cores 202-1236C-12H through 18H were demagnetized at 25 mT.

NRM intensities of the whole-round sections varied around 10^{-2} A/m for the upper ~120 mcd. At greater depths values were generally lower but more variable, alternating between 10^{-2} and 10^{-4} A/m. Discrete peaks were more commonly found from Core 202-1036A-9H to the base of the APC-cored interval (the whole rounds of the XCB cores were not measured), with values often >1 A/m. The peaks are generally restricted to core tops and reflect the accumulation of debris in the hole from drilling of the overlying section. After AF demagnetization at peak fields of 20 or 25 mT (Fig. F24), a substantial decrease in intensity is observed with values slightly more than an order of magnitude lower than their predemagnetized level. The downhole pattern of intensity variations is similar to that observed prior to demagnetization and to a large degree mimics the magnetic susceptibility profile. In general, the NRM intensity pattern reflects the major lithologic changes at Site 1236 (see "Lithostratigraphy," p. 5). Intensity values within lithologic Unit I are at or below 10^{-3} A/m for the upper 20 mcd and between 10^{-3} and 10^{-4} A/m at greater depths. Within Unit II beginning at ~120 mcd, the intensity values are generally lower (as low as 5×10^{-6} A/m) but are significantly more variable, with some intensities higher than those found in Unit I. Starting with Unit III, intensities begin to increase and continue increasing through Unit IV to a value $>10^{-2}$ A/m (Fig. F24).

F24. NRM after AF demagnetization, p. 52.

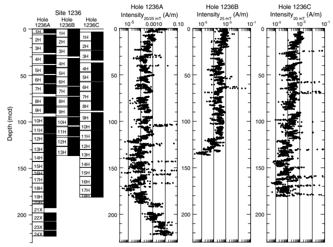

As observed at the previous sites, inclinations prior to demagnetization are steeply positive, characteristic of a drill string–induced magnetic overprint. After demagnetization at either 20 or 25 mT, negative and positive inclinations are observed, suggesting that much of this overprint is removed (Fig. F25). Inclinations steeper than expected are common in intervals of either negative or positive polarities (expected inclination is –37.5° at the latitude of Site 1236 during normal polarity) and may reflect slight coring deformation within these generally unlithified carbonate-rich sediments. A generally positive inclination bias is apparent (the overprint direction), particularly in Hole 1236B (Fig.

F25. NRM inclination after demagnetization, p. 53.

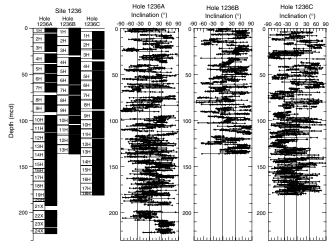

F25). Because of the overprint problem observed at previous sites (see **Lund et al.,** this volume), the nonmagnetic core barrel was used for even-numbered cores in Holes 1236A and 1236C and for odd-numbered cores in Hole 1236B. Although the effect of the nonmagnetic core barrel on NRM intensity was smaller than observed in the siliciclastic-rich sediments of Site 1235, it did result in more clearly recognizable polarities and reversals.

The directional data from the lower part of lithologic Unit I, beginning at ~100 mcd, and through all of Unit II displays no obvious polarity pattern (Fig. F25). These sediments contain coarse netritic carbonates (see **"Lithostratigraphy,"** p. 5) deposited by downslope processes. The reliability of any directional information in these transported sediments must, therefore, be questioned. However, the sediments cored with the XCB that comprise lithologic Units III and IV may preserve a reliable polarity sequence. Sediments from ~210 mcd to the base of the cored interval show clear reversed polarity.

Positive and negative inclinations are present within the upper 100 mcd of Site 1236, suggesting that correlation to the geomagnetic polarity timescale (GPTS) (Cande and Kent, 1995) may be possible (Fig. F26). Though normal and reversed polarities are common, few clear polarity transitions are recognized. Some transitions apparently recognized in one hole are not obvious in another hole at the same composite depth. Additionally, many intervals of indeterminate polarity are present, which complicates stratigraphic interpretation. A few unambiguous polarity transitions are observed, including the Gauss (2An)/Matuyama (2r) transition, the boundaries of the Olduvai (2n), the Jaramillo (1r.1n), and the Matuyama (2r)/Brunhes (1n) transition (Table T10).

F26. Inclination data and polarity interpretation correlated to the GPTS, p. 54.

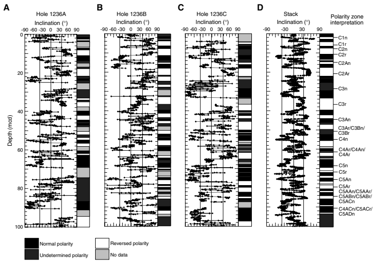

T10. Polarity chron boundaries, p. 69.

In view of the difficulty in recognizing clear polarity transitions, we have attempted to provide magnetostratigraphic information for Site 1236 by using the distinct fingerprint provided by the GPTS. Rather than picking discrete polarity reversal boundaries, we identified the magnetic chron(s) to which a sequence of sediment belongs. Because of the low fidelity of records from each individual hole, we stacked the inclination data from Holes 1236A, 1236B, and 1236C based on the composite depth scale (see **"Composite Section,"** p. 4). We then took a 10-point running mean of the stacked inclination data and interpreted the polarity sequence from the top down (Fig. F26). This stacked inclination record was correlated by anchoring the top of our record to the top of the GPTS and working downward. The stacked and smoothed record provides a relatively unambiguous match to the GPTS, with many individual polarity zones recognizable. The clarity of this record suggests that much of the noise within in each individual core is random and that stacking and smoothing significantly increased the signal-to-noise ratio. Based on the overall correlation to the fingerprint of the GPTS (Fig. F26), 18 polarity zone identifications were made within the upper 100 mcd of Site 1236. Ages for the polarity are given as midpoint averages of the polarity interval ages of Cande and Kent (1995). Depth errors are assumed to be plus or minus one-half the depth interval of the interpreted polarity zone (Table T11; Fig. F26). Other polarity events may be present in the smoothed stack record, suggesting that shore-based research may be able to resolve a more detailed magnetostratigraphy.

T11. Paleomagnetic age control points, p. 70.

GEOCHEMISTRY

Sediment Gases

Concentrations of headspace gases were routinely monitored in Hole 1236A sediments according to shipboard safety and pollution prevention considerations. Headspace methane concentrations were below 2 ppmv throughout the entire hole, equivalent to blank (i.e., laboratory air) concentrations. This indicates that no methanogenesis is now occurring at this site, consistent with the low organic matter contents in sediments (see **"Sedimentary Inorganic Carbon Concentrations,"** p. 18).

Interstitial Water Geochemistry

We collected 22 interstitial water samples from Hole 1236A. Chemical gradients at this site (Table **T12;** Fig. **F27**) reflect a minor influence of organic matter diagenesis by microbially mediated oxidation reactions, a limited degree of biogenic opal dissolution along with other controls on dissolved silicate, and a minor signature of calcite diagenesis. In general, chemical variations with depth at Site 1236 are minor compared to those at the Chile margin sites (1233–1235). Interstitial water geochemistry varies little with lithologic unit, except in the deepest sedimentary unit overlying presumed basement (Fig. **F27**).

T12. Interstitial water geochemical data, Hole 1236A, p. 71.

F27. Interstitial water geochemical data, p. 55.

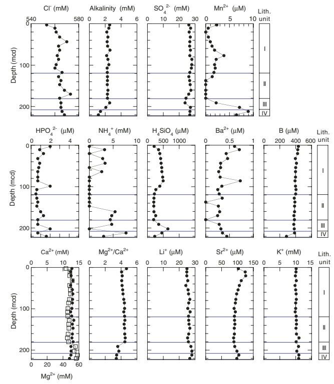

Chlorinity increases from 553 mM at 2.9 mcd to 570 mM at 43.6 mcd then decreases to values ~560–565 mM from 54.2 to 147.1 mcd (Fig. **F27**). Chlorinity is 573 mM at 170.4 mcd in a sample taken from an ash layer. Salinity, measured refractively as total dissolved solids, ranges from 34 to 36 (Table **T12**). Sodium concentrations measured by inductively coupled plasma–atomic emission spectrophotometry averaged 3% lower than those estimated by charge balance (Table **T12**). Sodium concentrations parallel chlorinity, with a total range from 473 to 492 mM.

Organic matter diagenesis, driven by microbial oxidation reactions, has a relatively minor influence on interstitial water composition. Sulfate undergoes a limited degree of reduction, by no more than 6 mM from typical seawater values of ~29 mM, to the lowest values in lithologic Unit III, with a value of 23.6 mM at 191.1 mcd coincident with a small local maximum in alkalinity. Alkalinity averages ~2.2 mM and varies little with depth except for a decrease to 1.1 mM observed in the deepest three samples from 202.3 to 220.2 mcd.

Dissolved manganese concentrations initially decrease from 2.3 µM at 2.9 mcd to below the detection limit (<0.1 µM) at 20.3 mcd then increase to 3.8 µM at 77.3 mcd before decreasing again to low values (generally below the detection limit) throughout lithologic Unit II (see **"Lithostratigraphy,"** p. 5). Manganese increases in Unit III to 8.9 µM at 212.0 mcd then decreases to 6.5 µM in the deepest sample at 220.2 mcd. The magnitude of the middepth peak is equivalent to those at Chile margin Sites 1233 and 1234, with the peak near the contact with presumed basement larger than any values at Sites 1233–1235. Dissolved iron is below the detection limit (<0.3 µM) in all samples, reflecting the low content of terrigenous material in this site relative to Chile margin Sites 1233–1235.

Phosphate concentrations decrease from 2 µM at 2.9 mcd to generally low values no more than a factor of 3–4 times the detection limit (0.4 µM) throughout. Ammonium concentrations are generally below the detection limit (2.2 µM), and the concentrations reported reflect a substantial blank correction relative to the measured signal. Phosphate and ammonium concentrations at Site 1236 are an order of magnitude lower than those at Chile margin Sites 1233–1235, as is alkalinity.

Dissolved silicate concentrations increase from 210 µM at 2.9 mcd to 492 µM at 86.1 mcd, near the only biostratigraphy sample observed to have abundant diatoms (see **"Biostratigraphy,"** p. 11). Silicate concentrations drop sharply to values averaging 210 µM from 127.9 to 179.9 mcd in lithologic Unit II. They then increase to 645 µM at 202.3 mcd, the highest value seen at this site. This sample was taken in an ash layer from the same core where one sample contained diatoms (rare), which were otherwise nearly absent throughout the drilled sequence (see **"Diatoms,"** p. 14, in "Biostratigraphy"). The interstitial waters are below saturation with respect to biogenic opal, and the profile indicates multiple influences with depth.

Barium concentrations are much lower than those in the reducing Chile margin Sites 1233–1235. The blank-corrected concentrations reported here are of similar magnitude to the analytical blank and not significantly greater than the detection limit, and show no significant variation with depth. The lack of a barium increase here, where sulfate values remain high throughout, is consistent with barite dissolution driven by solubility controlling site-to-site and depth variations in dissolved barium.

Boron concentrations decrease slightly with increasing depth, from 433 µM at 2.9 mcd to 385 µM at 196.9 mcd, with a steeper decrease to 284 µM in the deepest sample at 220.2 mcd. Boron concentrations at Site 1236 are lower than those at the Chile margin Sites 1233–1235, and the profile lacks the middepth maximum seen at those sites.

Calcium concentrations increase with depth, from 11.0 mM at 2.9 mcd to 12.9 mM at 32.2 mcd, then decline to 11.4 mM at 170.4 mcd before increasing to ≥14 mM from 191.1 to 220.2 mcd. Magnesium concentrations have minor variations with depth. Magnesium/calcium ratios decrease with depth from 4.7 at 2.9 mcd and to <4.2 from 10.9 to 43.6 mcd, increase slightly with depth to 4.5 from 170.4 to 180.0 mcd, and then decrease in the deepest four samples to 3.4–3.7 (Fig. F27). The limited range of variability in calcium and magnesium and therefore magnesium/calcium ratios at Site 1236 contrasts strongly with the nonconservative profiles of Chile margin Sites 1233–1235, which were dominated by the influence of authigenic mineralization reactions. Lithium concentrations increase slightly with depth, from 25 to 28 µM. Strontium concentrations are >100 µM from 2.9 to 54.2 mcd, generally decrease to 89 µM near the base of lithologic Unit II, and then increase to 100 µM from 202.3 to 220.2 mcd. Potassium concentrations range from 9.8 to 11.0 mM (Fig. F27).

T13. IC, $CaCO_3$, and TC concentrations, Hole 1236A, p. 72.

Sedimentary Inorganic Carbon Concentrations

Inorganic carbon (IC) and total carbon (TC) concentrations were determined on sediment samples from Hole 1236A (Table T13). Calcium carbonate concentrations typically range between 91 and 99 wt% in the uppermost 181 m of lithologic Units I and II (Fig. F28; see **"Description of Lithologic Units,"** p. 5, in "Lithostratigraphy"). Individual low calcium carbonate values (<93 wt%) in this depth range are associated with high volcanic glass abundance and low siliciclastic components (see **"Description of Lithologic Units,"** p. 5, in "Lithostratigraphy"). Calcium carbonate concentrations decrease in Unit III from ~97 wt% at

F28. Calcium carbonate vs. depth, p. 56.

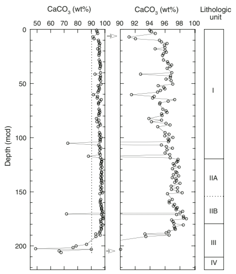

the top of the unit to a minimum of 49 wt% at 202.7 mcd (Fig. **F28**). No calcium carbonate determinations were made in Unit IV (207.7–222.3 mcd; see **"Description of Lithologic Units,"** p. 5, in "Lithostratigraphy").

Subtle changes in calcium carbonate concentrations typically occur at Site 1236 in the high–carbonate content Units I and II. These variations exceed the nominal analytical precision of ±0.2 wt% (see Table **T7,** p. 73, and **"Geochemistry,"** p. 32, both in the "Explanatory Notes" chapter) and may be explained by variations in calcium carbonate sedimentation, preservation, and dilution.

In the carbonate-rich sediments at Site 1236, total organic carbon (TOC) contents could not be determined with confidence by shipboard techniques. As is generally the case in sediments very rich in calcium carbonate, TOC concentrations are probably <0.2 wt% (Romankevich, 1984).

AGE MODEL AND MASS ACCUMULATION RATES

A 223.2-mcd-thick (207.7 mbsf) sequence of Neogene and upper Oligocene (~28 Ma) mostly calcareous sediments was recovered at Site 1236. Biostratigraphic and magnetostratigraphic age datums (see Tables **T7, T11**) were used to construct an age-depth model for this site (Table **T14;** Fig. **F29**). Linear sedimentation rates (LSRs), total MARs, and carbonate MARs were calculated at 1-m.y. intervals (see **"Age Models and Mass Accumulation Rates,"** p. 41, in the "Explanatory Notes" chapter).

T14. Age-depth model, LSRs, and MARs, p. 74.

F29. Biostratigraphic and magnetostratigraphic datums and age-depth model, p. 57.

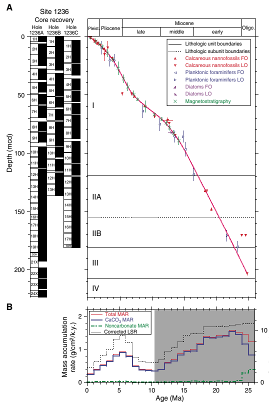

Age-Depth Model

Both biostratigraphic and magnetostratigraphic age datums are well constrained and in general agreement for the upper 90 mcd (Fig. **F29**). Almost no reworked specimens were observed (see **"Biostratigraphy,"** p. 11). Large error bars on the magnetostratigraphic datums result from the method used for identifying polarity chrons (see **"Paleomagnetism,"** p. 15). Below 90 mcd, age datums become less frequent, preservation becomes worse in some intervals (especially at depth >150 mcd), some standard middle and early Miocene biostratigraphic zonal markers are absent, and the agreement between magnetostratigraphic and biostratigraphic datums becomes less certain. The downhole transition to more scattered datums occurs at ~11–12 Ma, approximately when biostratigraphic datums are no longer astronomically tuned. The age-depth relationship relies primarily upon available magnetostratigraphic data, which is not available below ~90 mcd. In the deepest section (90–222 mcd), a nearly straight line was used to approximate the age-depth relationship because of a paucity of reliable biostratigraphic datums.

Three specific calcareous nannofossil outliers were not included in the generation of this age-depth model (see **"Biostratigraphy,"** p. 11). These included the last occurrence of *T. rugosus* (~49.4 mcd; 5.35 Ma), which was considered only because the LO of *D. quinqueramus* (5.56 Ma) was not observed near the Miocene/Pliocene boundary. Another outlier resulted from the LO of *C. floridanus* at 71.8 mcd (~13 Ma), whose age may be more than 1 m.y. younger at Site 1236 than has been observed elsewhere. The two calcareous nannofossil outliers at ~170 mcd (LOs of *R. bisecta* and *Z. bijugatus*) may represent anomalous appearances or reworking and are not supported by other microfossil datums.

Linear Sedimentation and Mass Accumulation Rates

Site 1236 LSRs and both total and carbonate MARs follow the same general trend for the last 25 m.y. (Fig. F29). LSRs range between ~3 and 11 m/m.y., and MARs range between 0.2 and 1.6 g/cm²/k.y. Values are high at the base of the record but decrease gradually until ~11 Ma. A peak in LSRs (~9 m/m.y.) and MARs (~0.9 g/cm²/ky) occurs between 6-5 Ma. The rates then decrease gradually toward minimum values at the top of the record.

Some variation in dry density occurs, represented by the changing relationship between LSRs and total MARs. The accuracy of dry density measurements between ~24 and 17.5 Ma (119.5–206.5 mcd) may have been compromised in intervals of unconsolidated grainstones because the moisture contents may not have represented saturated in situ conditions. Carbonate MARs closely mimic total MARs for essentially the entire record, indicating that only minimal input of noncarbonate components has occurred throughout the site's history.

The relatively high accumulation rate of lithologic Unit II is related to downslope gravity flows from nearby carbonate platforms (see **"Lithostratigraphy,"** p. 5). Gravity flows are apparent at least through ~17.5 Ma (the top of Unit II). Two isolated intervals of unlithified wackestone also are present as shallow as 65 and 99 mcd, indicating that at least some influx of neritic grains through gravity flows occurred as recently as ~11 Ma. Therefore, at ages >17.5 Ma, and possibly >11 Ma, inferences cannot be made about surface water productivity from MARs and LSRs, as the production signal cannot be distinguished from gravity-driven accumulation.

The interval of low carbonate MAR (~0.4 g/cm²/k.y.) from 8 to 12 Ma coincides with the so-called "carbonate crash," which is an interval of poor preservation recognized in equatorial east Pacific sediments below 3000 m water depth (Lyle et al., 1995). Given the shallow paleowater depth of Site 1236 at <1300 m well above the lysocline and no evidence for a change in carbonate preservation (see **"Biostratigraphy,"** p. 11), the low carbonate MARs may reflect the oligotrophic environment at the eastern boundary of the subtropical gyre rather than a link to the "carbonate crash." Carbonate MARs rise from 9 to 6 Ma and peak between 6 and 5 Ma (0.9 g/cm²/k.y). This peak in MAR matches a similar event, referred to as the "biogenic bloom," in the equatorial Pacific that is inferred to reflect anomalously high productivity (Farrell et al., 1995; Pisias et al., 1995). A long-term trend of increasing productivity from ~9 to ~5 Ma could result from gradual eastward tectonic drift of the site toward the South American margin, but drift cannot explain the discrete peak in MAR. Similar trends occur in LSRs and MARs at other Leg 202 sites (see **"Age Model and Mass Accumulation Rates,"** p. 25, in the "Site 1237" chapter) and in the LSRs of some Leg 138 sites (especially Sites 848 and 846; see fig. 18, in the Leg 138 summary chapter (Shipboard Scientific Party, 1992). This MAR peak may indicate widespread trends in biogenic sedimentation. Site 1236 MARs and LSRs decrease from 5 to 0 Ma, indicating a gradual decrease in productivity at this site from a late Miocene and Pliocene maximum.

REFERENCES

Behrenfeld, M.J., Randerson, J.T., McClain, C.R., Feldman, G.C., Los, S.O., Tucker, C.J., Falkowski, P.G., Field, C.B., Frouin, R., Esaias, W.E., Kolber, D.D., and Pollack, N.H., 2001. Biospheric primary production during and ENSO transition. *Science,* 291:2594–2597.

Berggren, W.A., Kent, D.V., Swisher, C.C., III, and Aubry, M.-P., 1995. A revised Cenozoic geochronology and chronostratigraphy. *In* Berggren, W.A., Kent, D.V., Aubry, M.-P., and Hardenbol, J. (Eds.), *Geochronology, Time Scales and Global Stratigraphic Correlation.* Spec. Publ.—SEPM, 54:129–212.

Cande, S.C., and Haxby, W.F., 1991. Eocene propagating rifts in the southwest Pacific and their conjugate features on the Nazca plate. *J. Geophys. Res.,* 96:19609–19622.

Cande, S.C., and Kent, D.V., 1995. Revised calibration of the geomagnetic polarity timescale for the Late Cretaceous and Cenozoic. *J. Geophys. Res.,* 100:6093–6095.

Duncan, R.A., and Hargraves, R.B., 1984. Plate tectonic evolution of the Caribbean region in the mantle reference frame. *In* Bonini, W.E., Hargraves, R.B., and Shagam, R. (Eds.), *The Caribbean-South American Plate Boundary and Regional Tectonics.* Mem.—Geol. Soc. Am., 162:81–94.

Exon, N.F., Kennett, J.P., Malone, M.J., et al., 2001. *Proc. ODP, Init. Repts.,* 189 [CD-ROM]. Available from: Ocean Drilling Program, Texas A&M University, College Station TX 77845-9547, USA.

Fairbridge, R.W., 1967. Phases of diagenesis and authigenesis. *In* Larsen, G., and Chilingar, G.V. (Eds.), *Diagenesis in Sediments:* Amsterdam (Elsevier).

Farrell, J.W., Raffi, I., Janecek, T.C., Murray, D.W., Levitan, M., Dadey, K.A., Emeis, K.-C., Lyle, M., Flores, J.-A., and Hovan, S., 1995. Late Neogene sedimentation patterns in the eastern equatorial Pacific. *In* Pisias, N.G., Mayer, L.A., Janecek, T.R., Palmer-Julson, A., and van Andel, T.H. (Eds.), *Proc. ODP, Sci. Results,* 138: College Station, TX (Ocean Drilling Program), 717–756.

Lyle, M., Dadey, K.A., and Farrell, J.W., 1995. The late Miocene (11–8 Ma) eastern Pacific carbonate crash: evidence for reorganization of deep-water circulation by the closure of the Panama Gateway. *In* Pisias, N.G., Mayer, L.A., Janecek, T.R., Palmer-Julson, A., and van Andel, T.H. (Eds.), *Proc. ODP, Sci. Results,* 138, College Station, TX (Ocean Drilling Program), 821–838.

Mix, A.C., Pisias, N.G., Bloomer, S.F., and Mayer, L.A., 1998. *Southeast Pacific Paleoceanographic Transects, Site Survey Data Package 3: 3.5 kHz Data, Genesis Leg III,* R/V Roger Revelle, *Feb.–Apr. 1997:* Corvallis (Oregon State Univ.).

Mix, A.C., Pisias, N.G., Goldfinger, C., West, B., Mayer, L.A., and Bloomer, S.F., 1997. *Southeast Pacific Paleoceanographic Transects, Site Survey Data Package 2: Genesis Leg III,* R/V Roger Revelle, *Feb.–Apr. 1997:* Corvallis (Oregon State Univ.)

Ocean Climate Laboratory, 1999. *World Ocean Atlas 1998 (WOA98)* [CD-ROM]. Available from: National Climatic Data Center, Asheville NC 28801-5001, USA.

Pisias, N.G., Mayer, L.A., and Mix, A.C., 1995. Paleoceanography of the eastern equatorial Pacific during the Neogene: synthesis of Leg 138 drilling results. *In* Pisias, N.G., Mayer, L.A., Janecek, T.R., Palmer-Julson, A., and van Andel, T.H. (Eds.), *Proc. ODP, Sci. Results,* 138: College Station, TX (Ocean Drilling Program), 5–21.

Porrenga, D.H., 1967. Glauconite and chamosite as depth indicators in the marine environment. *In* Hallam, A. (Ed.), *Depth Indicators in Marine Sedimentary Rocks.* Mar. Geol., Spec. Iss., 5:495–502.

Romankevich, E.A., 1984. *Geochemistry of Organic Matter in the Ocean:* New York (Springer-Verlag).

Shipboard Scientific Party, 1992. The planning and execution of a high-resolution paleoceanographic drilling leg: a summary. *In* Mayer, L., Pisias, N., Janecek, T., et al., *Proc. ODP, Init. Repts.,* 138 (Pt. 2): College Station, TX (Ocean Drilling Program), 1095–1096.

Strub, P.T., Mesias, J.M., Montecino, V., Rutllant, J., and Salinas, S., 1998. Coastal ocean circulation off western South America. *In* Robinson, A.R., and Brink, K.H. (Eds.), *The Sea* (Vol. 11): *Coastal Oceans:* New York (Wiley), 273–313.

Young, J.R., 1998. Neogene. *In* Bown, P.R. (Ed.), *Calcareous Nannofossil Biostratigraphy* (Vol. 8): Dordrecht (Kluwer Academic), 225–265.

Figure F1. **A.** Locations of Sites 1236 and 1237 and bathymetry. **B.** Site locations and oceanographic features off Peru and northern Chile (CC = Coastal Current off Peru, know as the Coastal Current, PCCC = Peru-Chile Countercurrent, PCC = Peru-Chile Current), after Strub et al. (1998). Modern mean annual sea-surface temperatures (SSTs) (contours are in degrees Celsius, after Ocean Climate Laboratory, 1999).

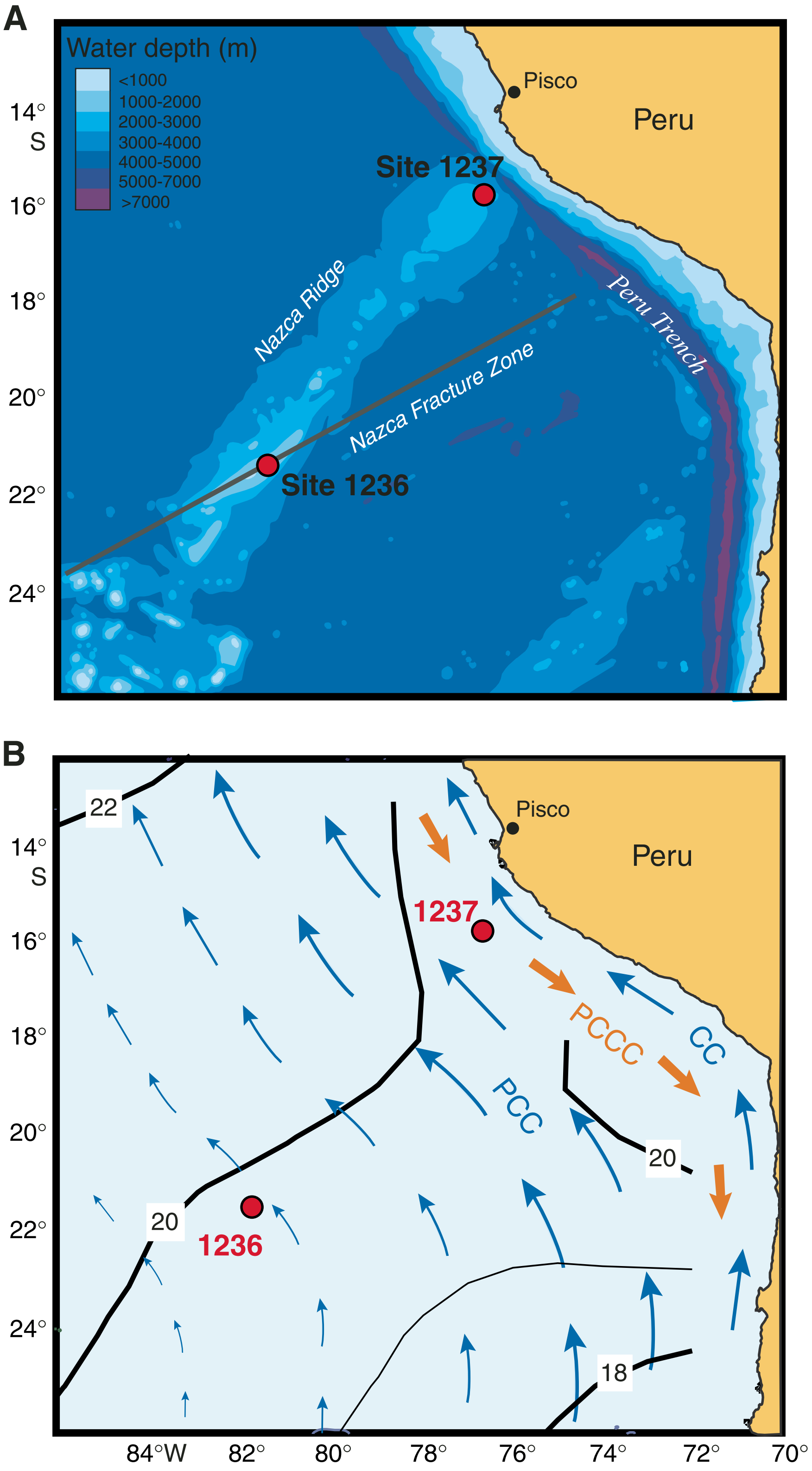

Figure F2. High-resolution swath bathymetry at Site 1236 (Mix et al., 1997) Countour interval = 50 m.

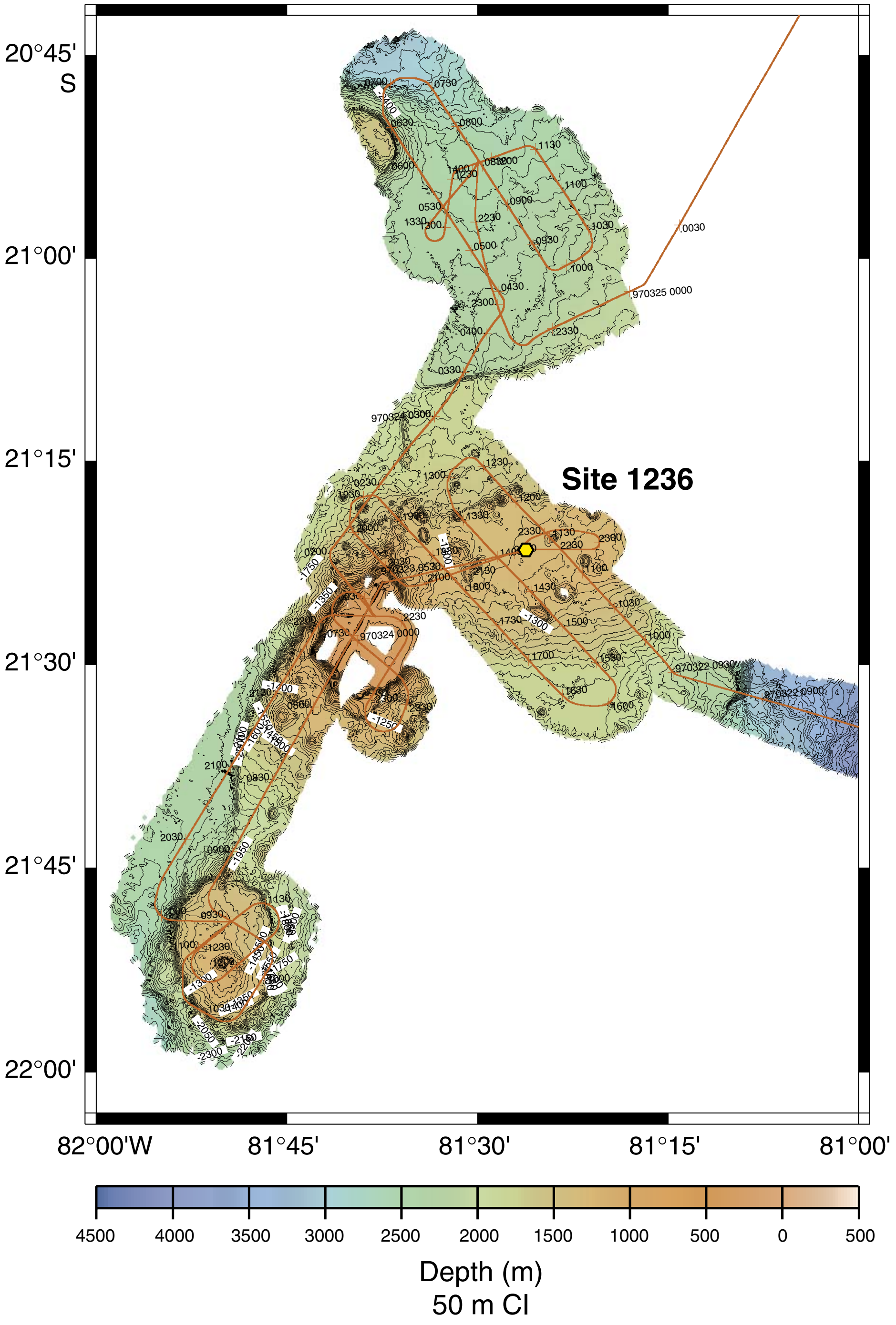

Figure F3. Seismic profile at Site 1236 (line 970322, *Revelle,* NAZ-1B-5, Shotpoint 366, 2201z, 80-in³ water gun at 30–400 Hz, notch filter at 60 Hz; Mix et al., 1997).

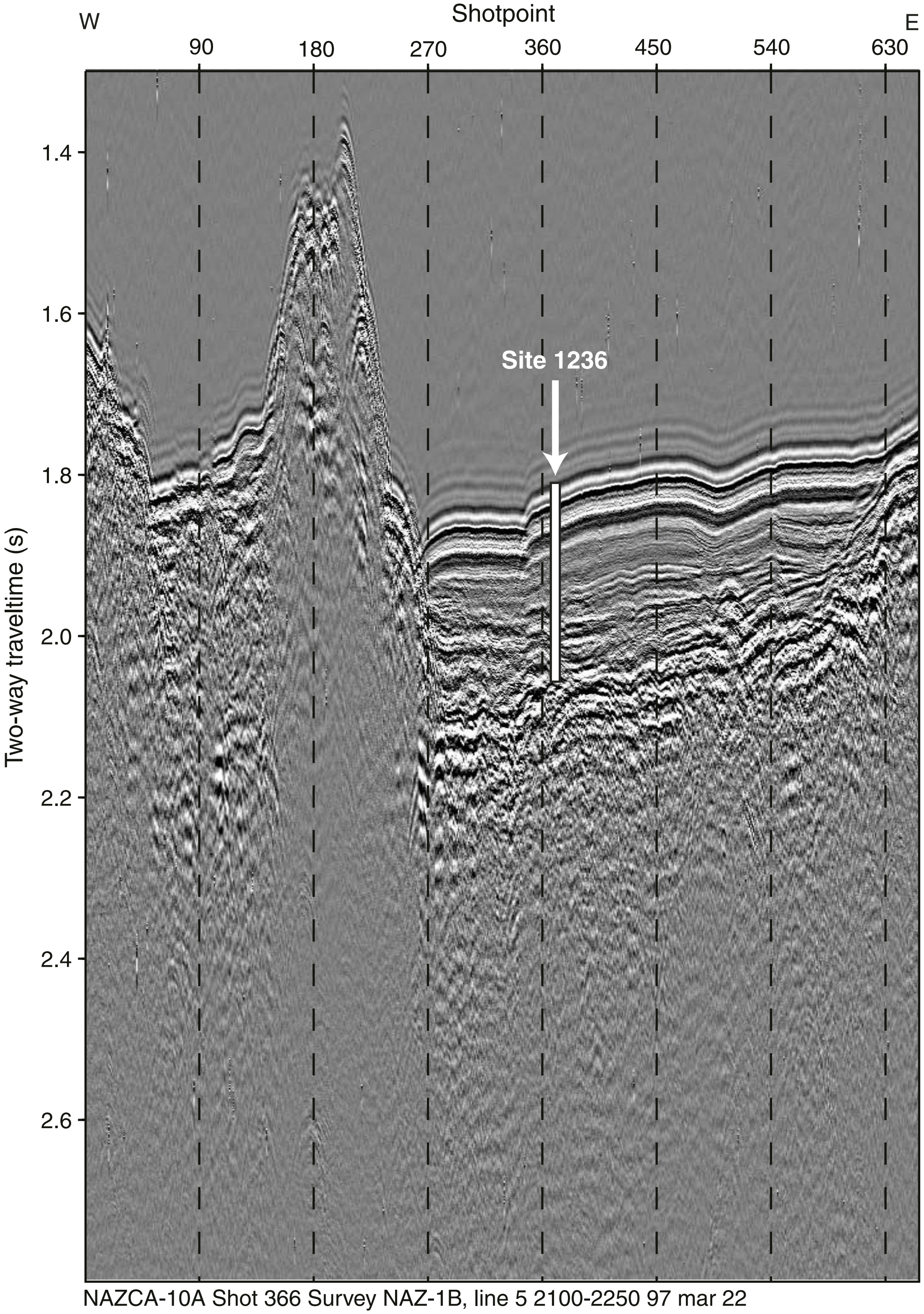

Figure F4. Tectonic backtrack of Site 1236, relative to a fixed South America. Poles of rotation are from Duncan and Hargraves (1984) and Pisias et al. (1995). The dotted path represents positions in million-year increments. Numbers denote ages (in millions of years) of changes in rate or direction of drift. Contours of modern mean annual sea-surface temperature are superimposed (Ocean Climate Laboratory, 1999). PCC = Peru-Chile Current, SEC = South Equatorial Current.

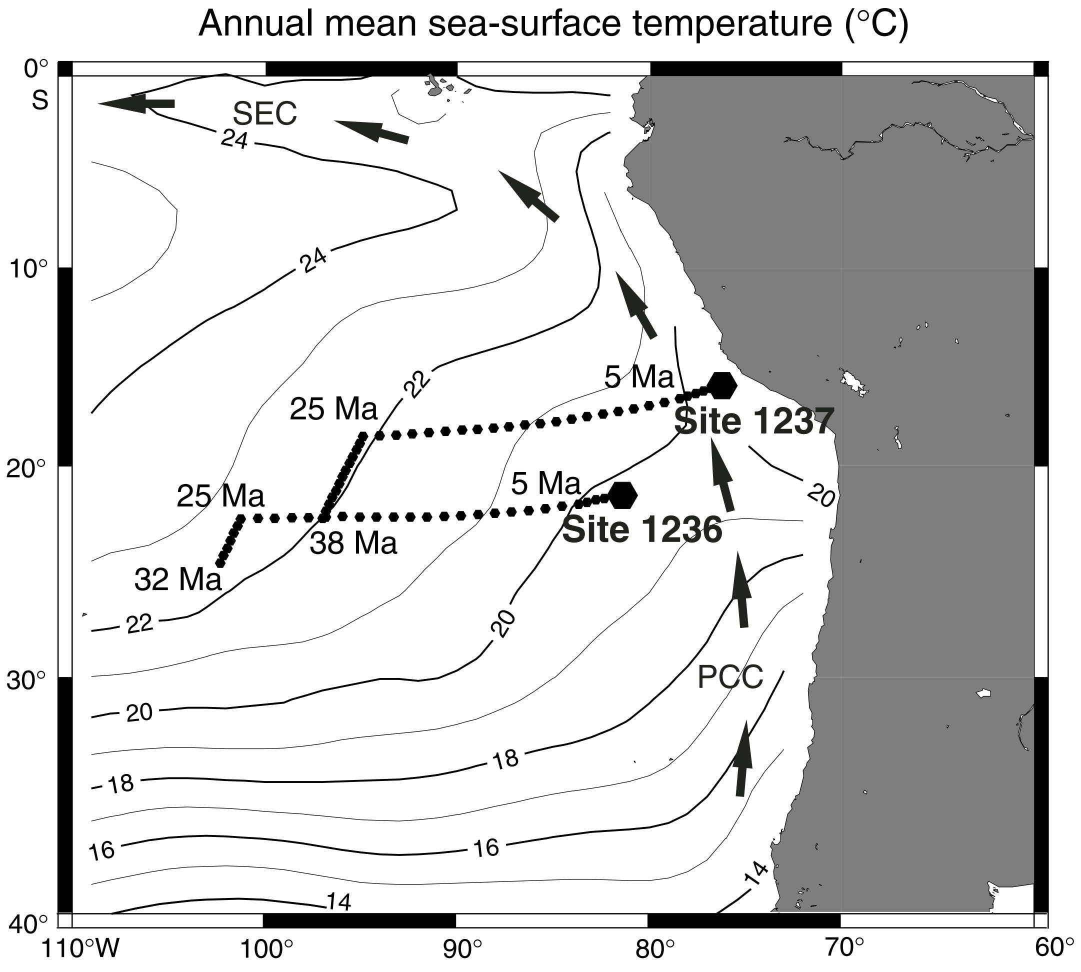

Figure F5. Modern annual-average properties of the upper ocean at paleolocations of Site 1236, based on plate tectonic backtracking and an assumption of no temporal changes in regional oceanic properties. Atlas data on physical and chemical properties are from WOA98 (Ocean Climate Laboratory, 1999). Primary productivity (PP) is from satellite measurements of sea-surface color (Behrenfeld et al., 2001). Pycnocline depth is calculated to the nearest 5 m, based on the shallowest maximum in the vertical density gradient. Symbols are average values extracted from the nearest 1° latitude-longitude box in each atlas. Lines = smoothed trends of each property along the backtrack path. SST = sea-surface temperature, SSS = sea-surface salinity.

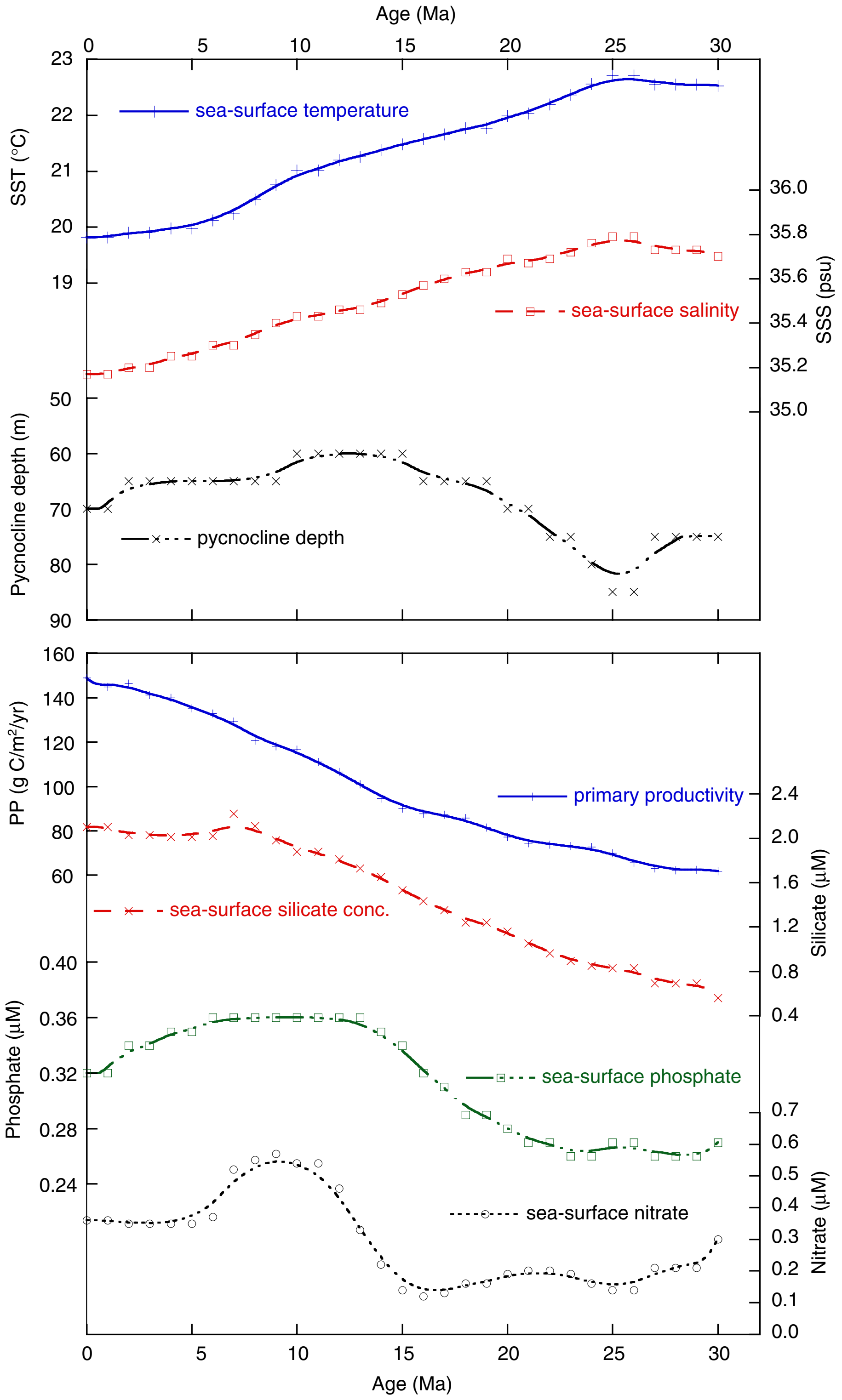

Figure F6. Meridional cross section of water masses, characterized by dissolved oxygen concentrations in the southeast Pacific (Ocean Climate Laboratory, 1999). Southward-spreading middepth waters (PCW = Pacific Central Water) are characterized by relatively low oxygen and salinity and high nutrients. Northward-flowing bottom water, below ~3 km depth, starts as relatively oxygen-rich Antarctic Circumpolar Deep Water (CPDW). Northward-spreading Antarctic Intermediate Water (AAIW), above 1 km depth, is high in oxygen but is low in both salinity and nutrients.

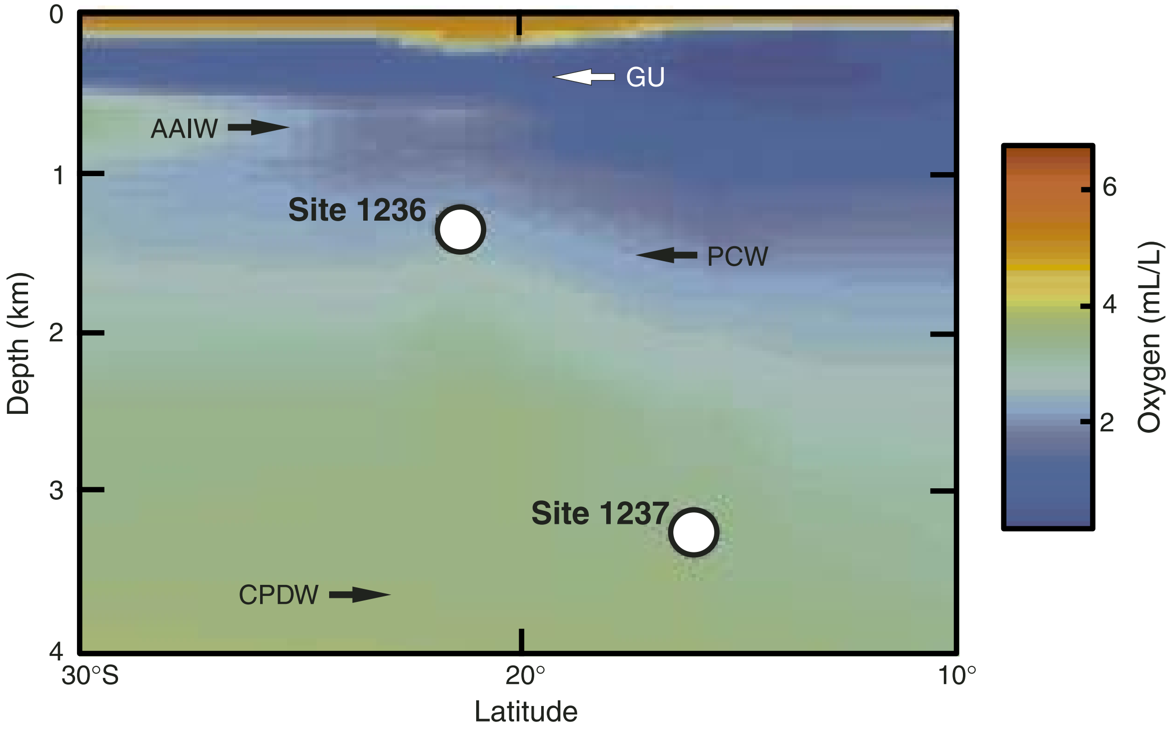

Figure F7. Magnetic susceptibility data collected with the MST system (MST-MS) vs. mcd for the Site 1236 splice and Holes 1236A though 1236C. Gray boxes indicate the portions of cores that are in the splice. **A.** 0–40 mcd. **B.** 30–70 mcd. (Continued on next three pages.)

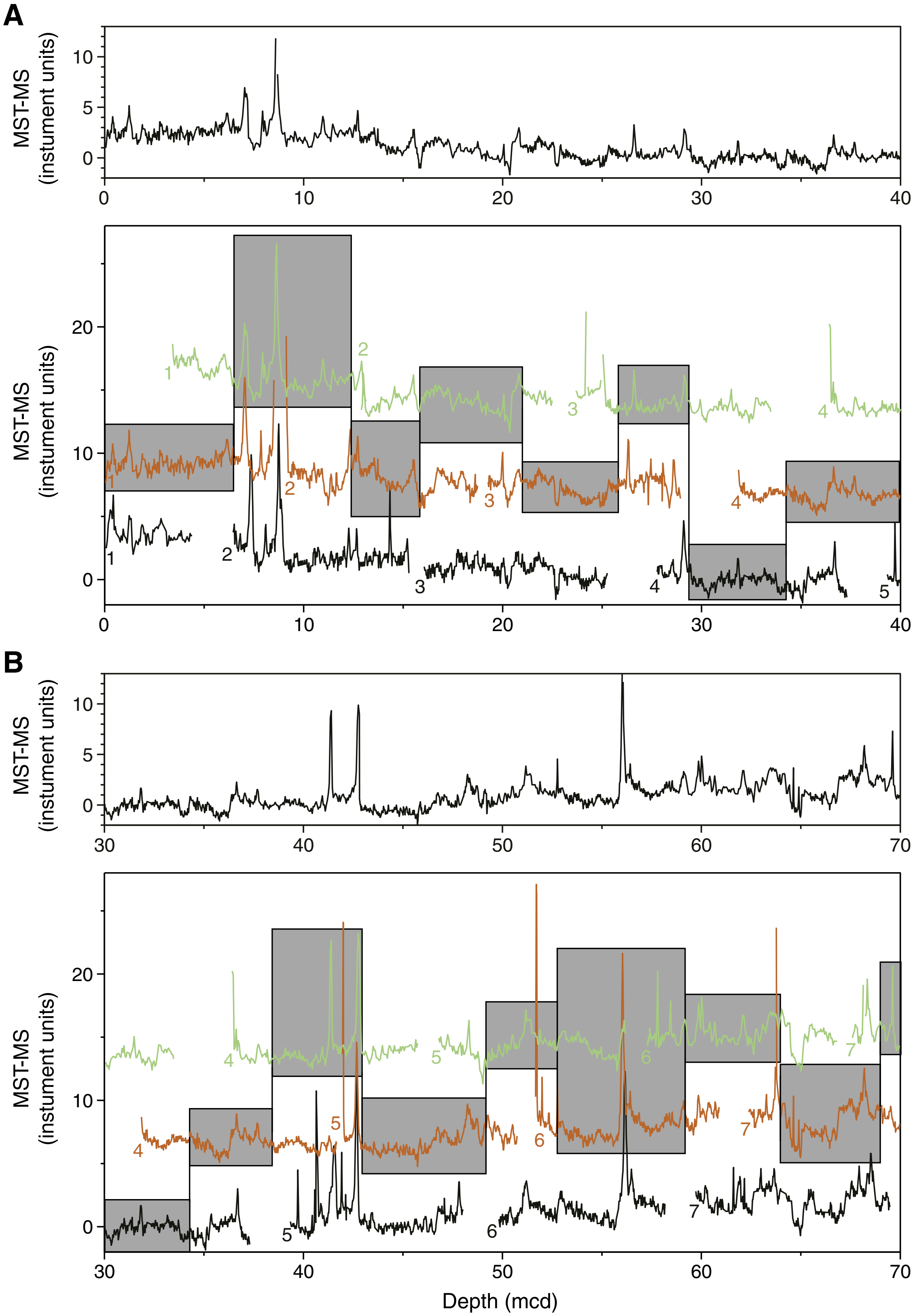

Figure F7 (continued). C. 60–100 mcd. **D.** 90–130 mcd.

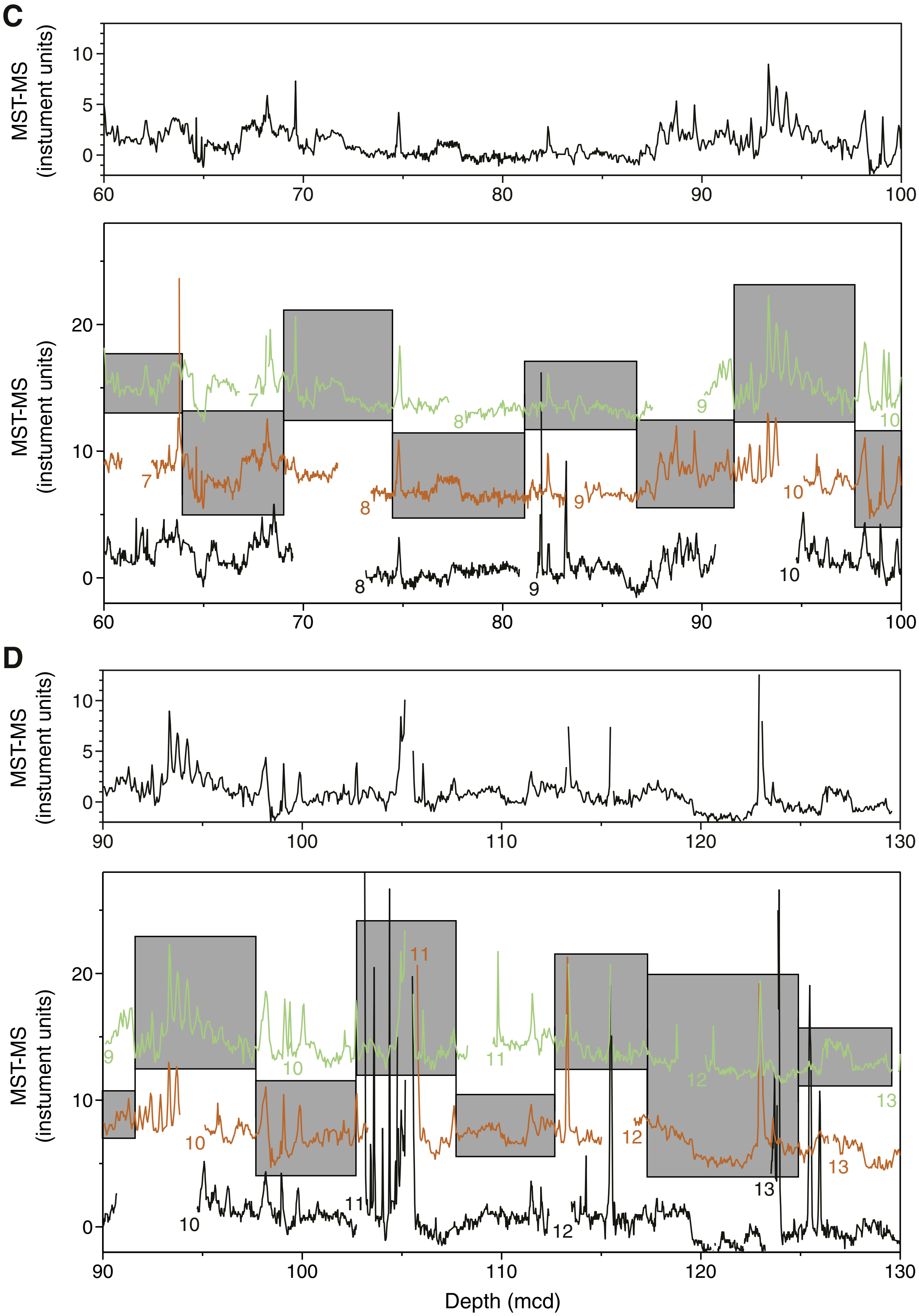

Figure F7 (continued). **E.** 120–160 mcd. **F.** 150–190 mcd.

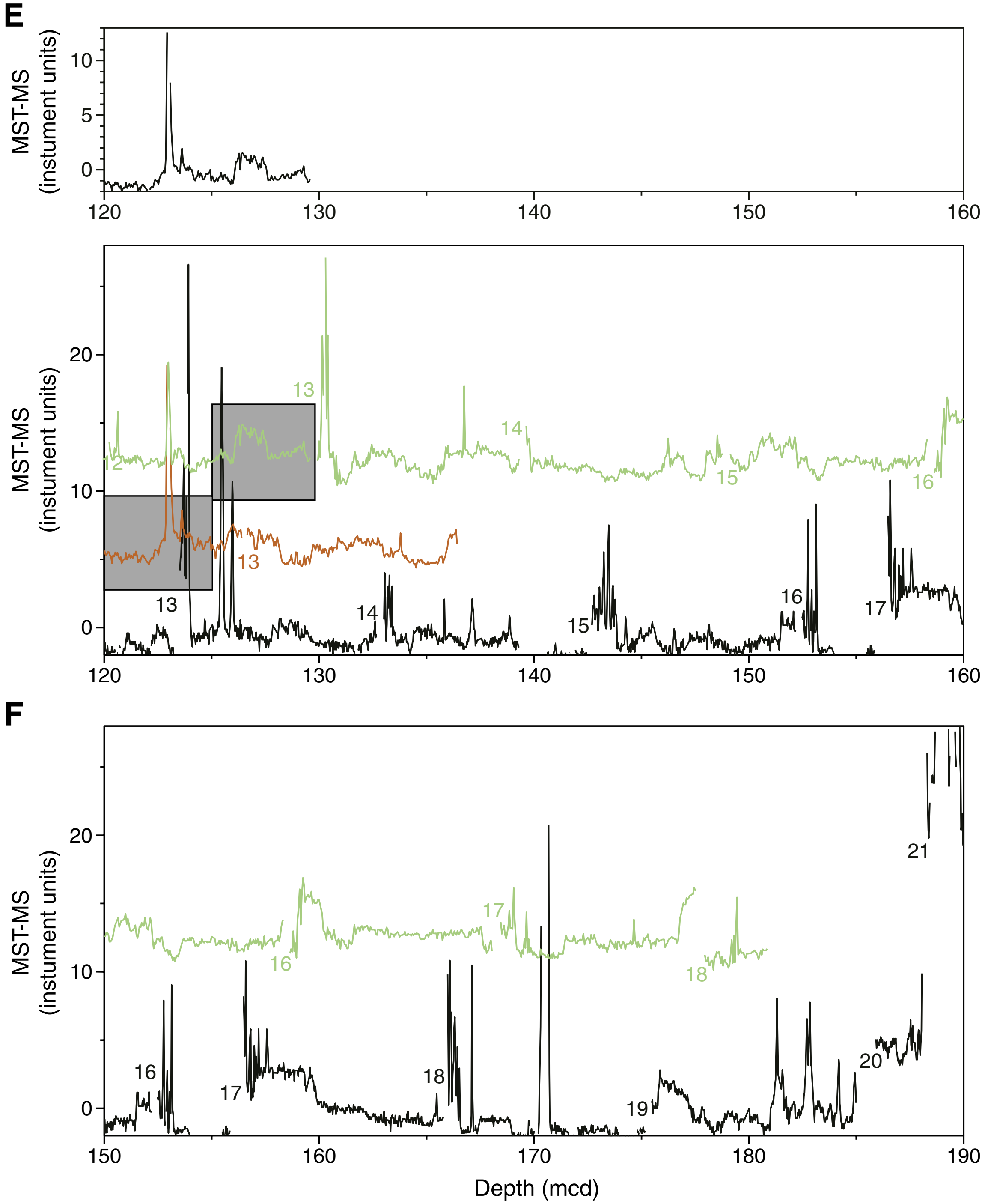

Figure F7 (continued). **G.** 180–220 mcd. **H.** 210–250 mcd.

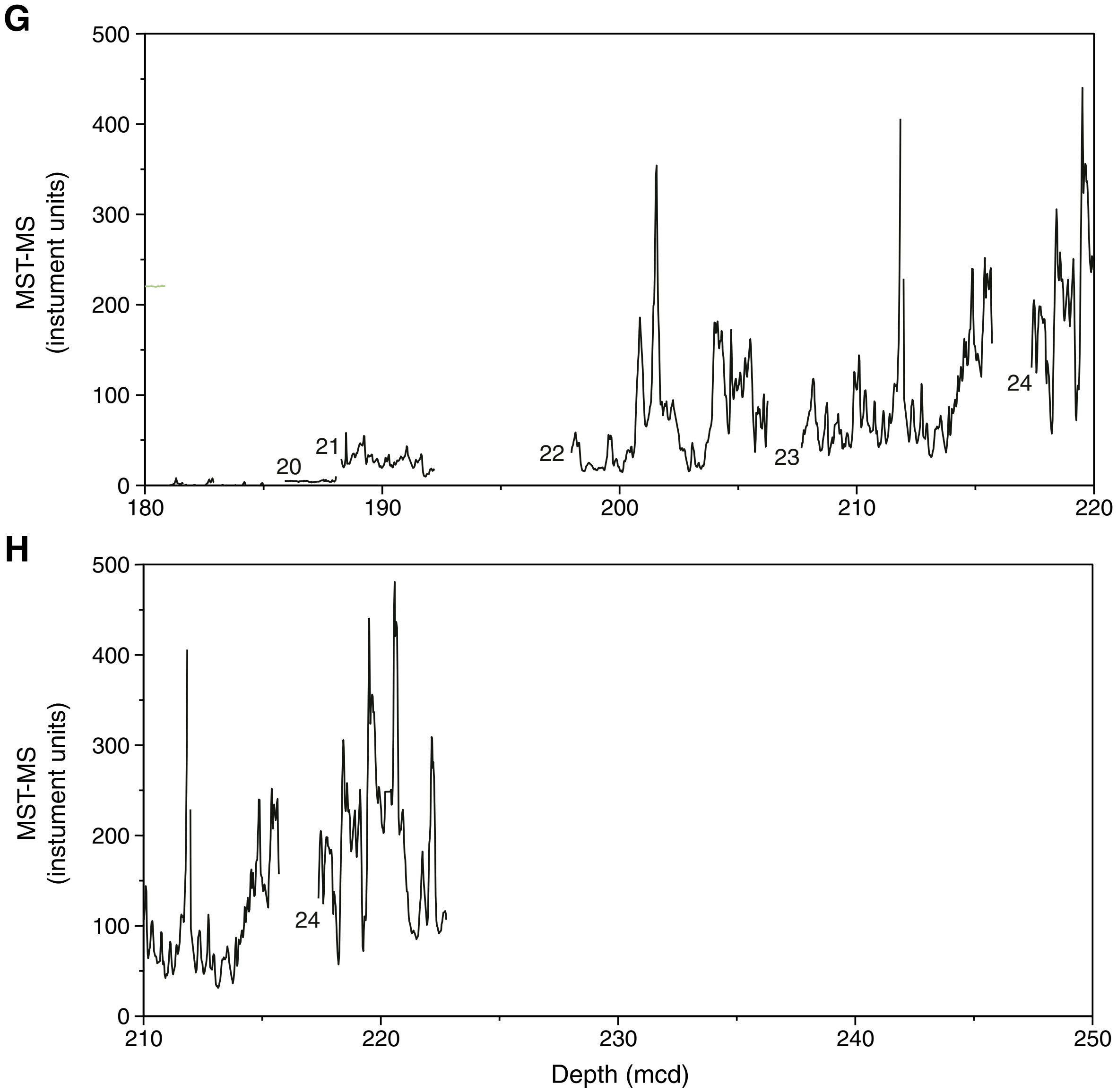

Figure F8. Reflectance (a*) collected with the AMST system vs. mcd for the Site 1236 splice and Holes 1236A though 1236C. Gray boxes indicate the portions of cores that are in the splice. **A.** 0–40 mcd. **B.** 30–70 mcd. (Continued on next three pages.)

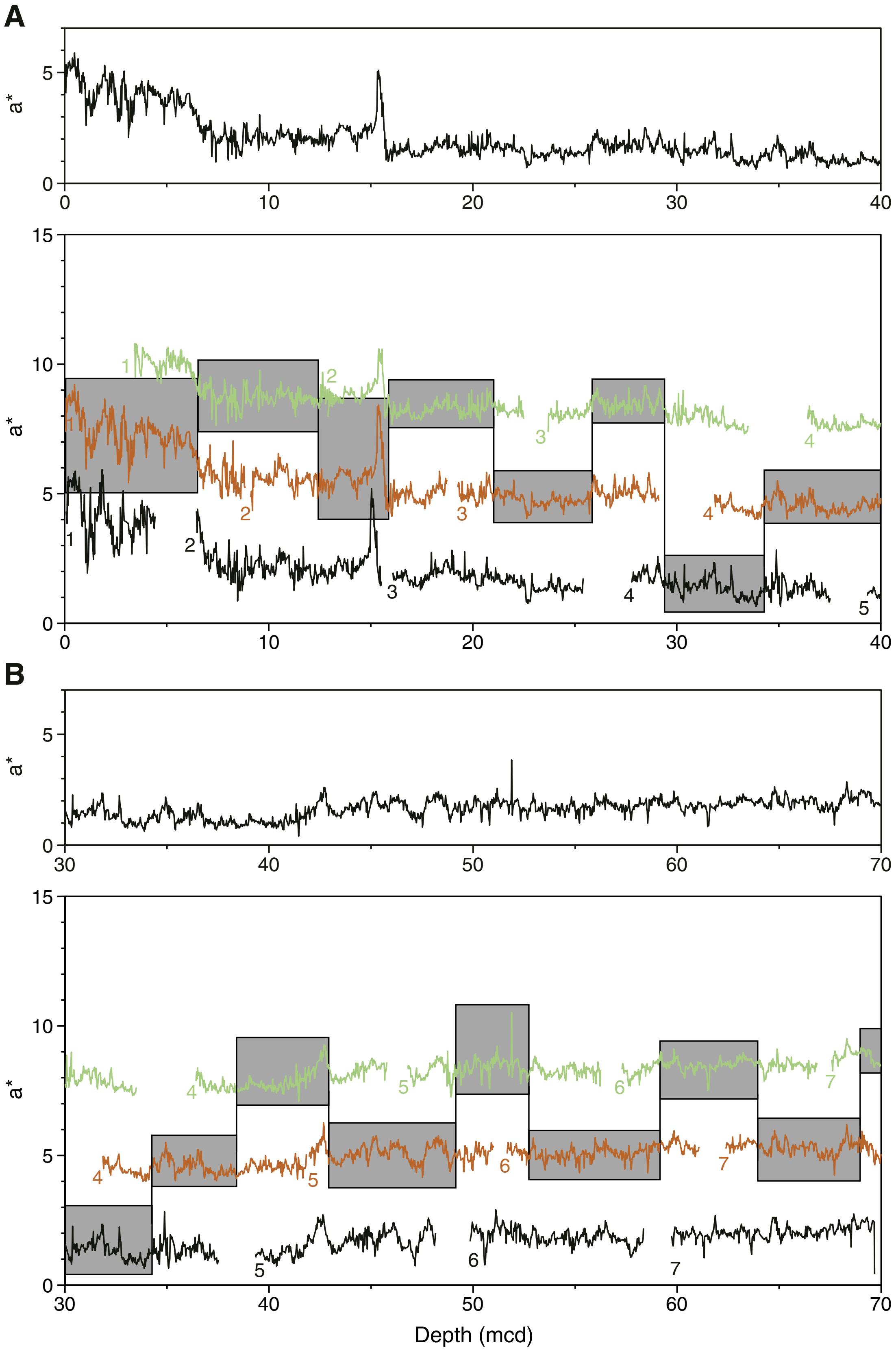

Figure F8 (continued). **C.** 60–100 mcd. **D.** 90–130 mcd.

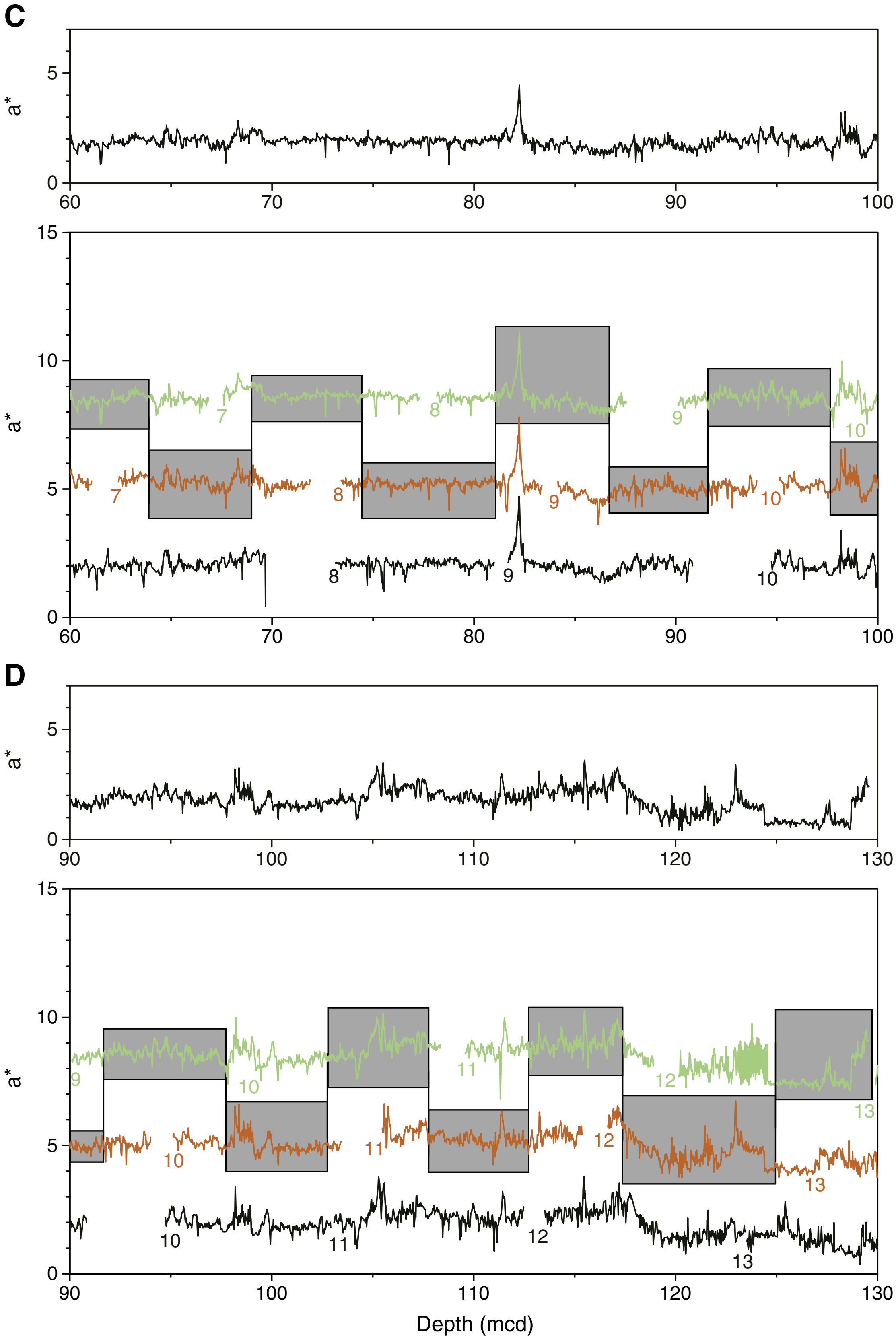

Figure F8 (continued). E. 120–160 mcd. F. 150–190 mcd.

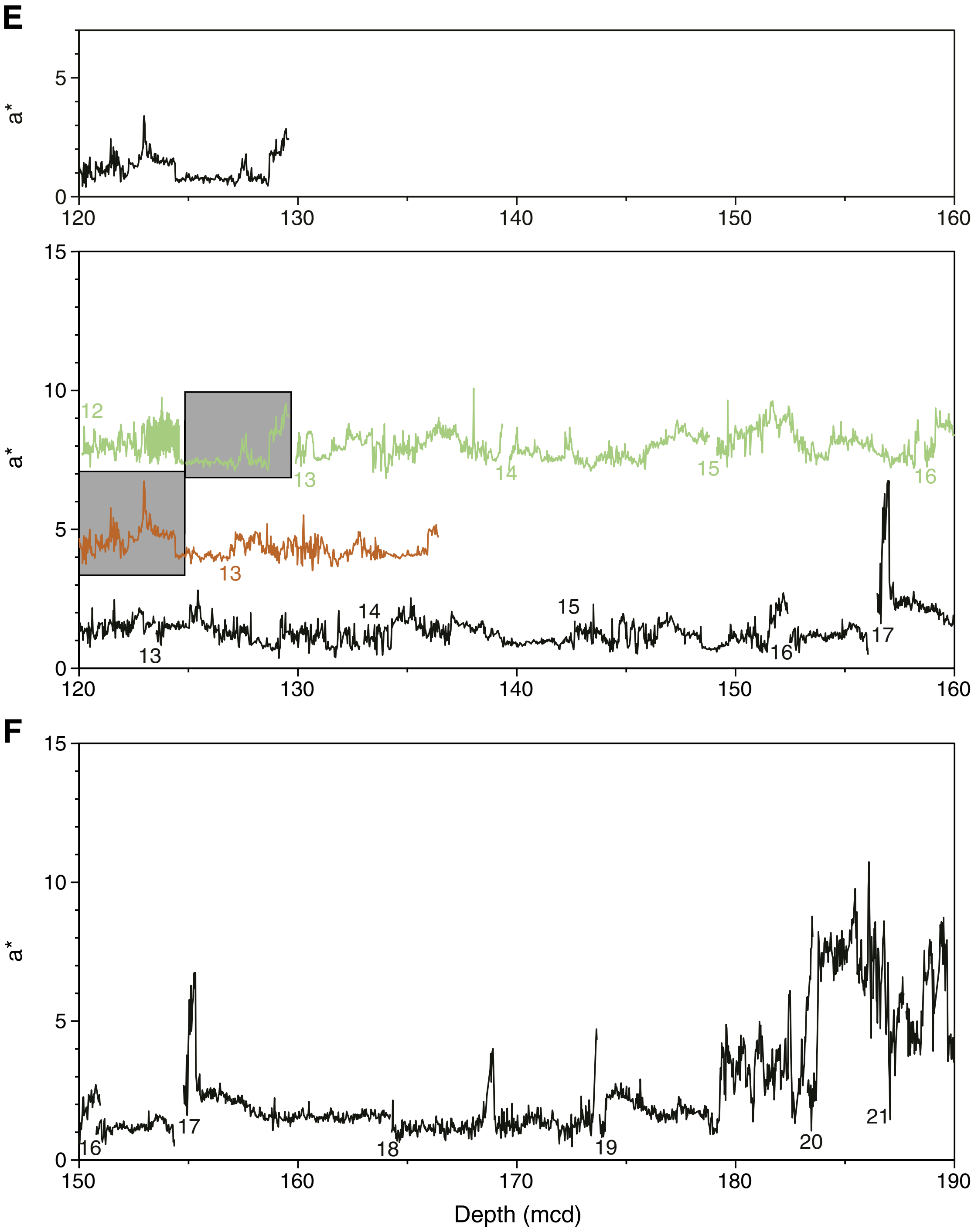

Figure F8 (continued). **G.** 180–220 mcd. **H.** 210–250 mcd.

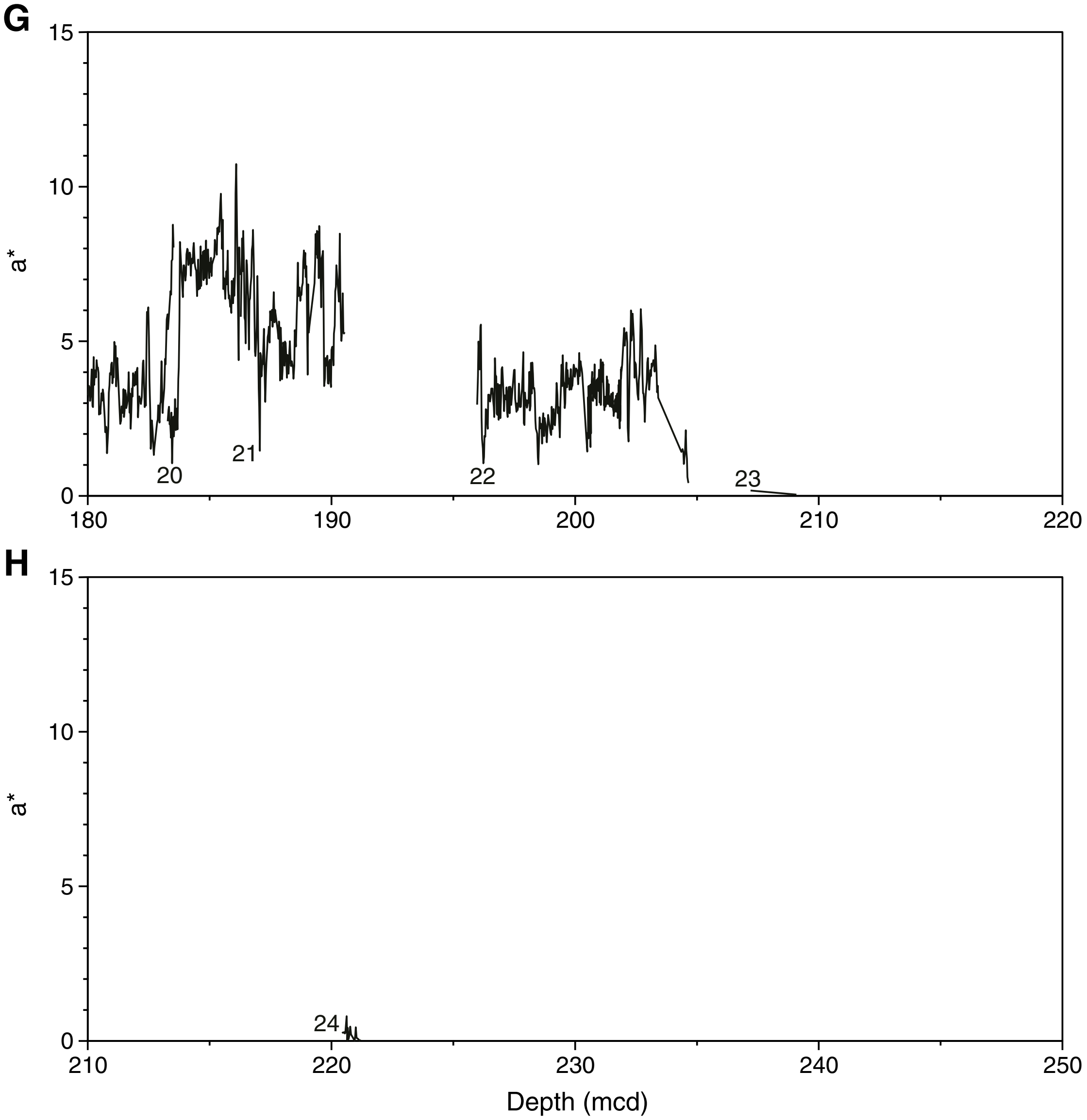

Figure F9. Spliced records of reflectance (a*), gamma ray attenuation (GRA) bulk density, and magnetic susceptibility (MST-MS) from Site 1236.

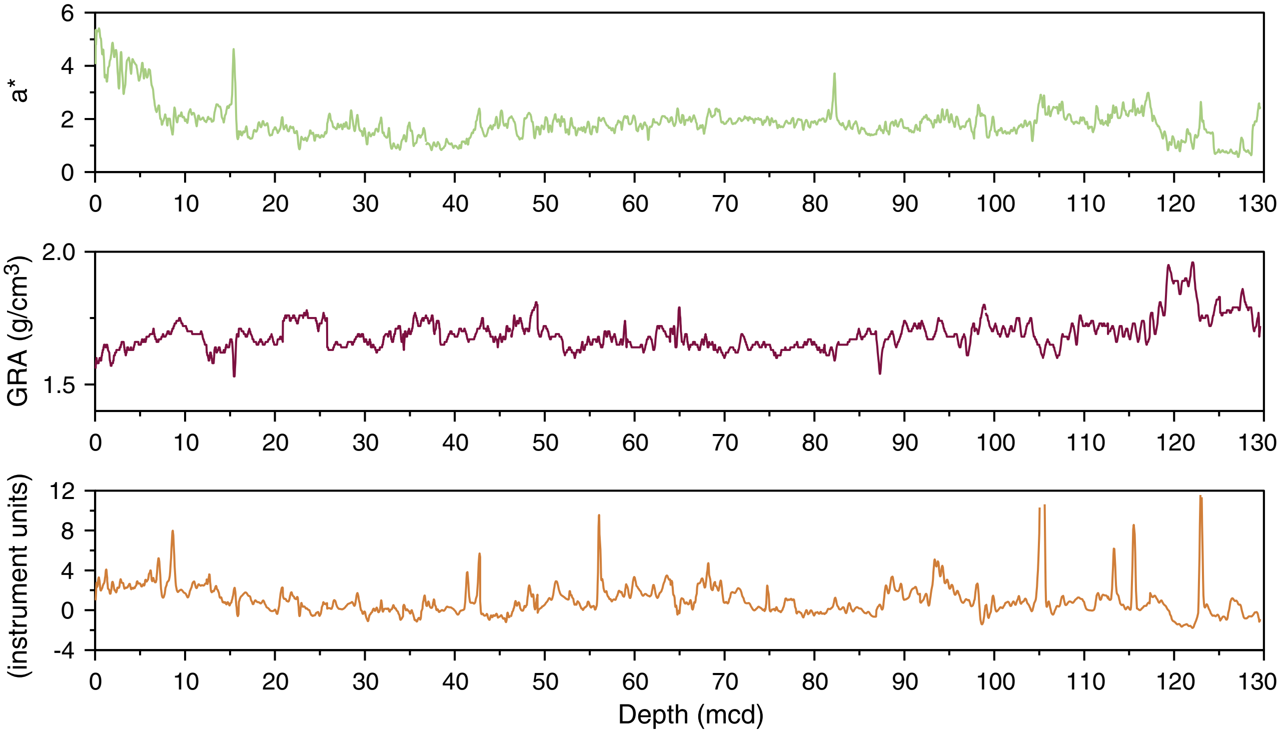

Figure F10. A comparison of the drillers depth (mbsf) and meters composite depth (mcd) scales in Holes 1236A through 1236C. The purple box shows the extent of the spliced record. On average, mcd is 14% greater than mbsf. The 1:1 (mbsf:mcd) line is also shown for comparison. GF = growth factor.

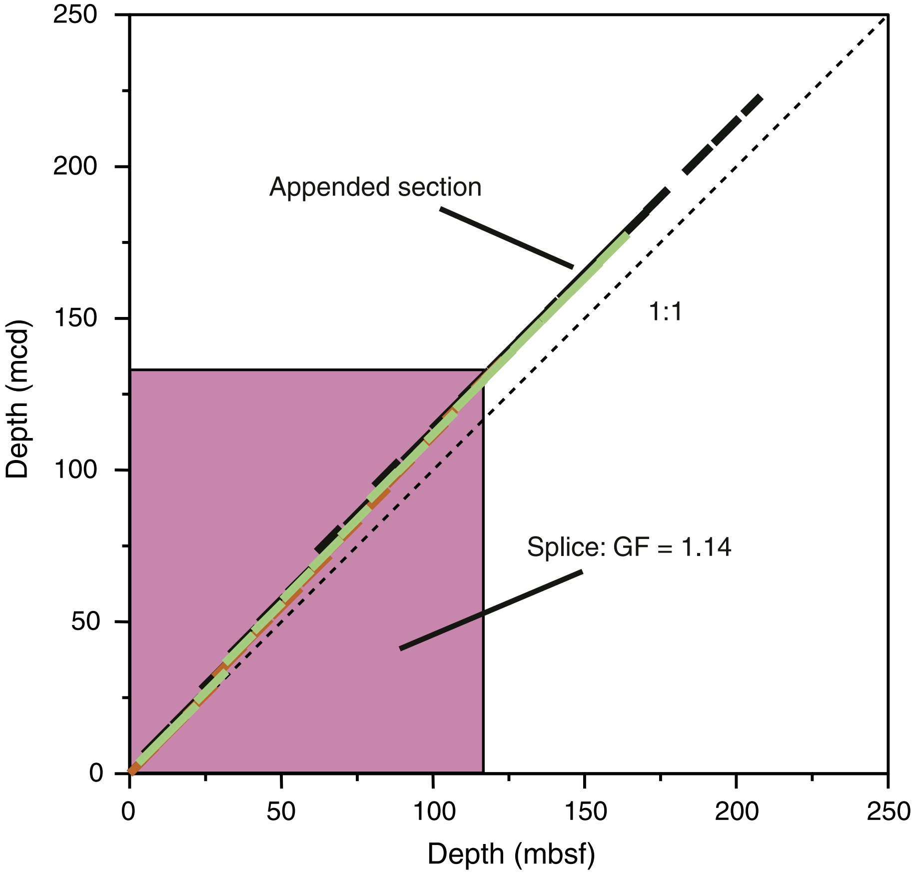

Figure F11. Core recovery, lithostratigraphy, magnetic susceptibility, gamma ray attenuation (GRA) bulk density, lightness, chroma a*, chroma b*, and calcium carbonate concentrations of recovered sediments from Site 1236.

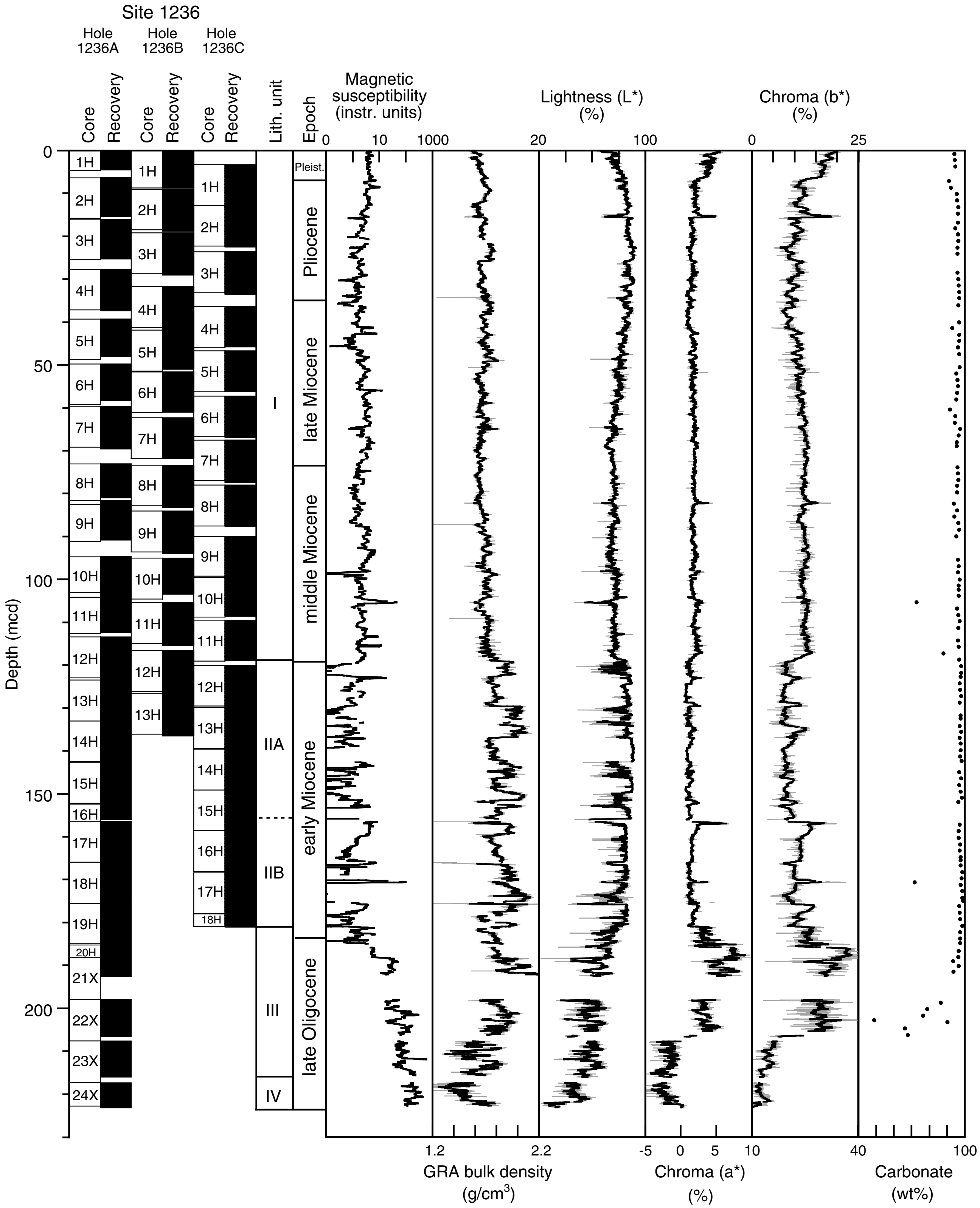

Figure F12. Bulk and grain densities and porosity measured on discrete samples from Site 1236. MAD = moisture and density.

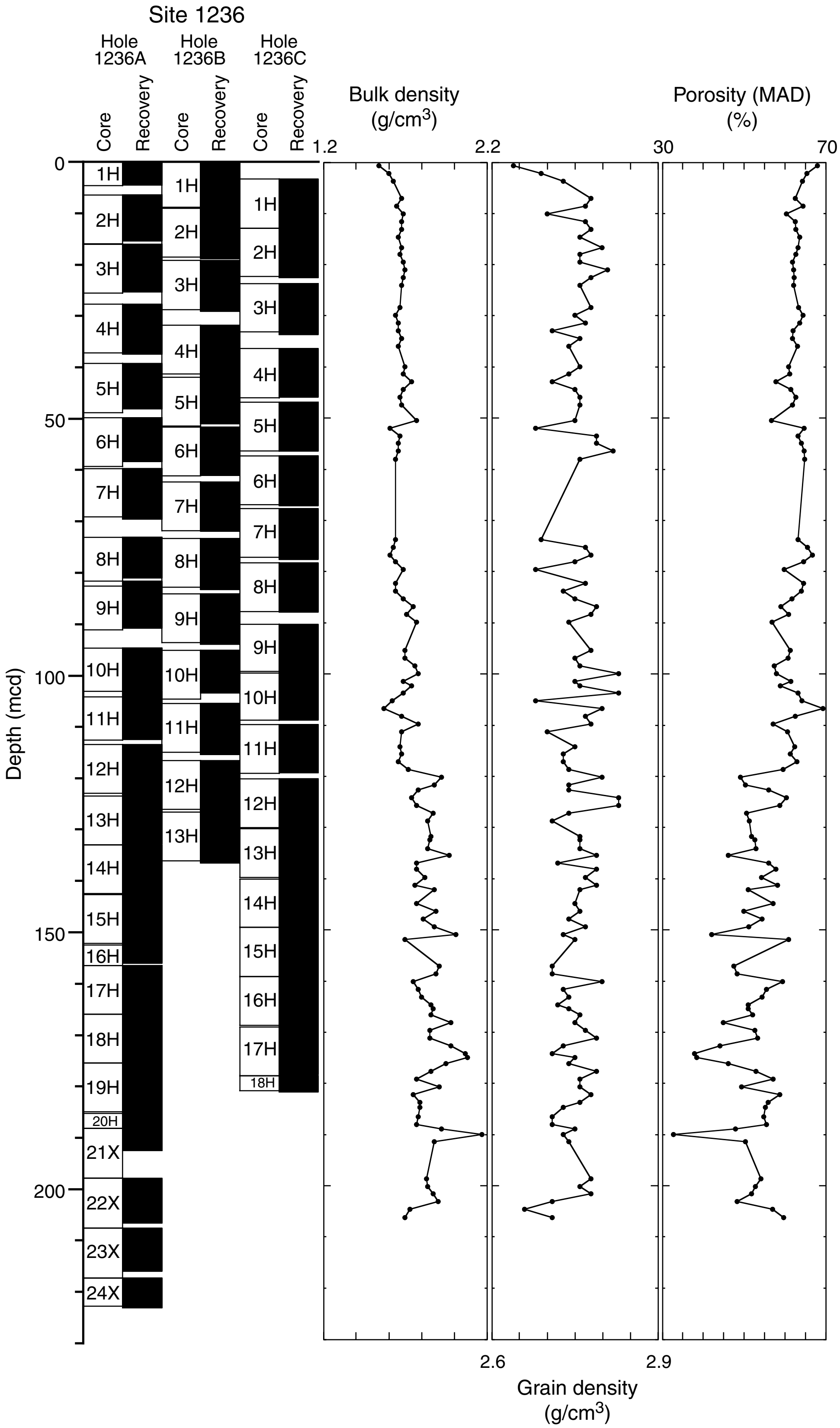

Figure F13. Major components observed in smear slides (dominant lithologies only) compared to carbonate concentration and the magnetic susceptibility (MS) record. Note that 1.5 instrument units have been added to the 5-point average of the original data set (see Fig. F11, p. 39) in order to exclude negative values for logarithmic scaling. microf. = microfossil.

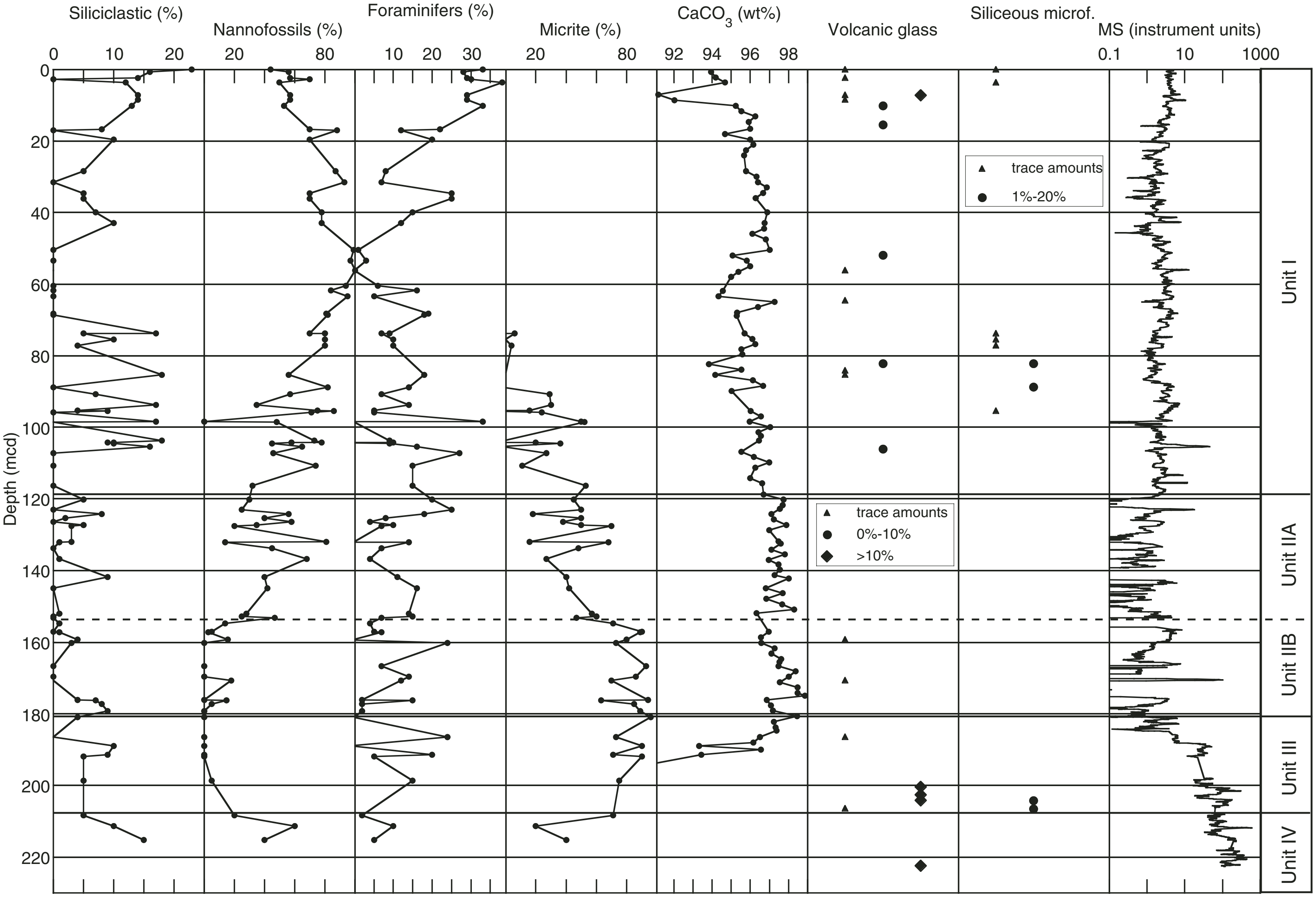

Figure F14. Close-up photograph of the uppermost nonpelagic grain–rich layer present in Unit I (interval 202-1236A-7H-4, 74–100 cm).

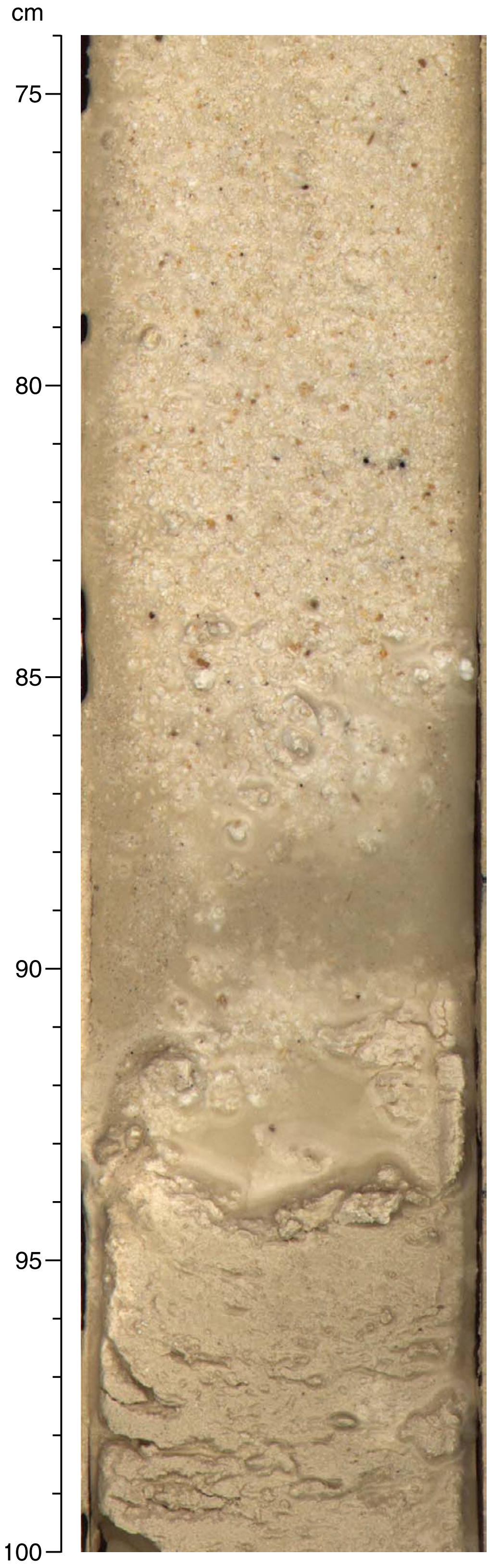

Figure F15. Close-up photograph of a volcanic ash layer in Unit I (interval 202-1236B-11H-1, 0–42 cm). Note the sharp lower boundary and diffuse top.

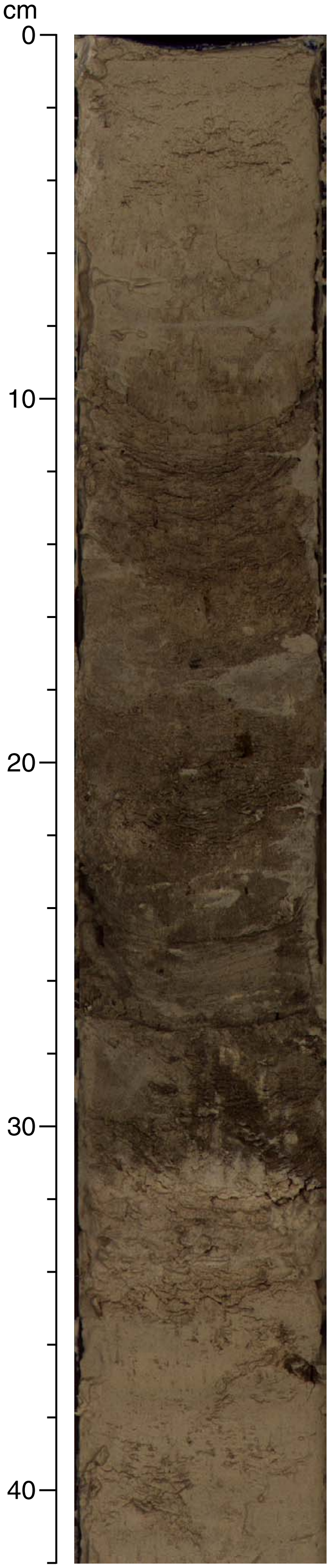

Figure F16. Magnetic susceptibility, gamma ray attenuation (GRA) bulk density, and lightness of the four lithologic units, Site 1236. Brown dots indicate position of volcanic ash layers. Black bars = thickness and position of nonpelagic grain–rich layers in Units I and II. Thick colored lines = 5-point averages. Note that 1.5 instrument units have been added to the original magnetic susceptibility data set (see Fig. F11, p. 39) in order to exclude negative values for logarithmic scaling. upw. fining = upward fining. * = inferred basement.

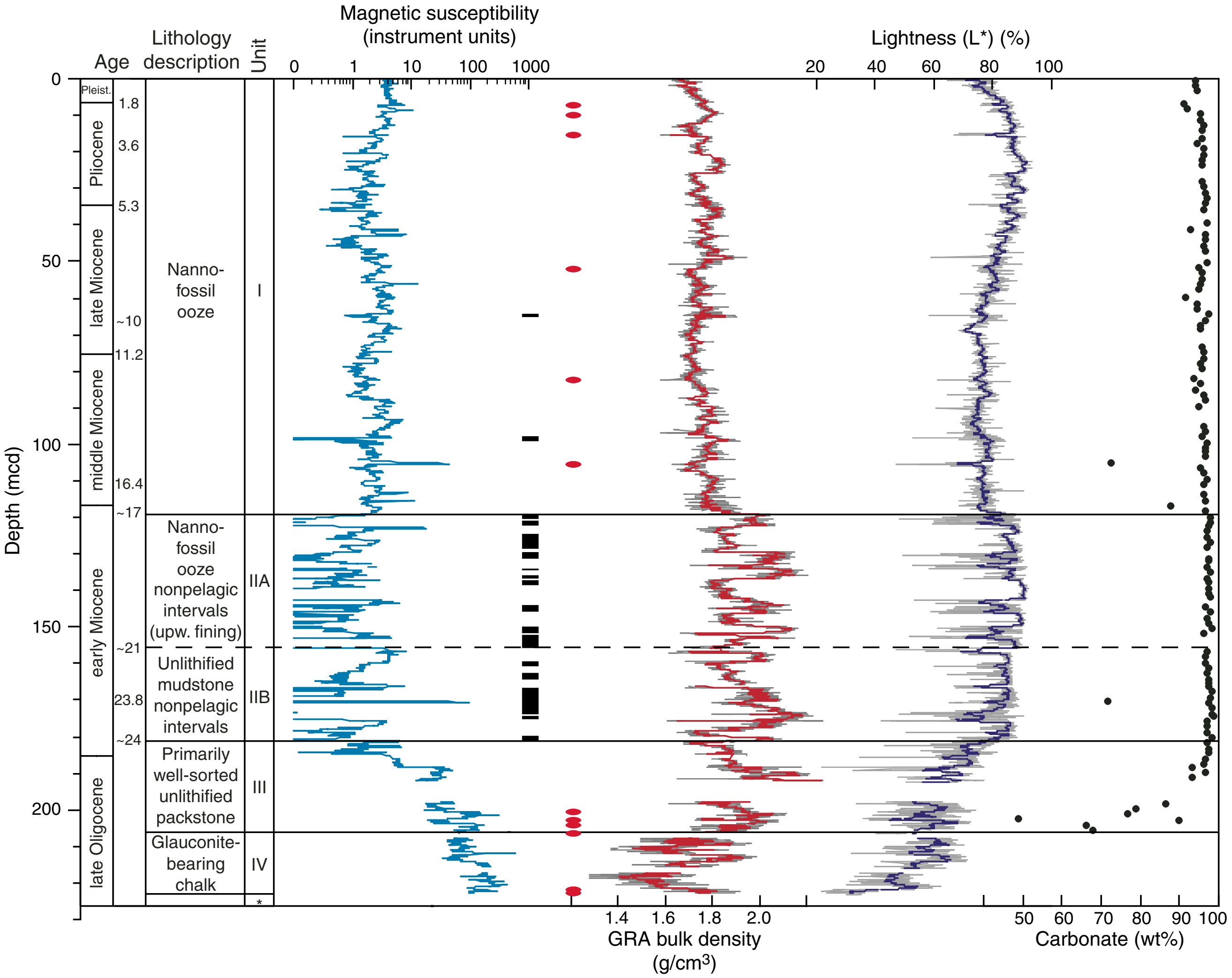

Figure F17. Color measurements plotted in the a*-b* color plane. **A.** Entire sequence at Site 1236. **B–E.** Units I–IV.

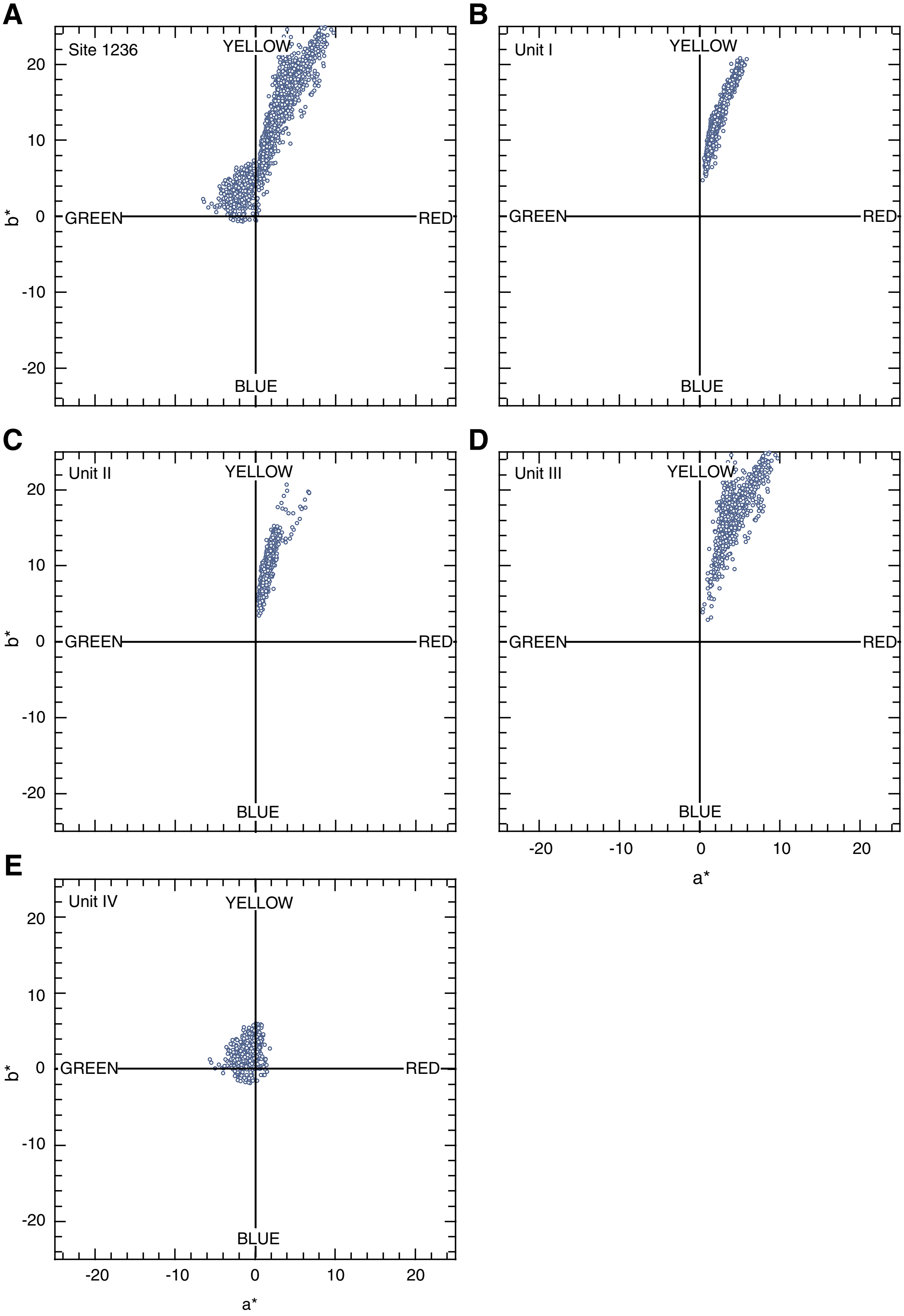

Figure F18. Close-up photograph of a fining-upward sequence of unlithified rudstone to wackestone in Unit II (interval 202-1236C-18H-4, 65–148 cm).

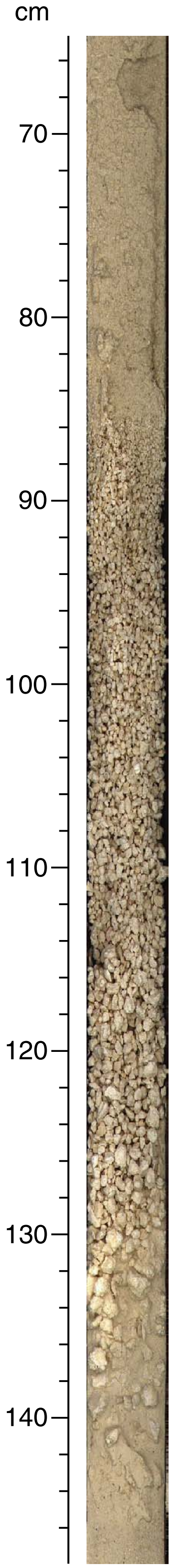

Figure F19. Photomicrograph of skeletal grain-rich rudstone. **A.** Sample 202-1236A-18H-1, 90–92 cm. **B, C.** Sample 202-1236A-18H-5, 61–62 cm. **D.** Sample 202-1236A-18H-1, 0–2 cm. (i) = peloids, (ii) = larger benthic foraminifers, (iii) = red algae, and (iv) = bryozoan fragments.

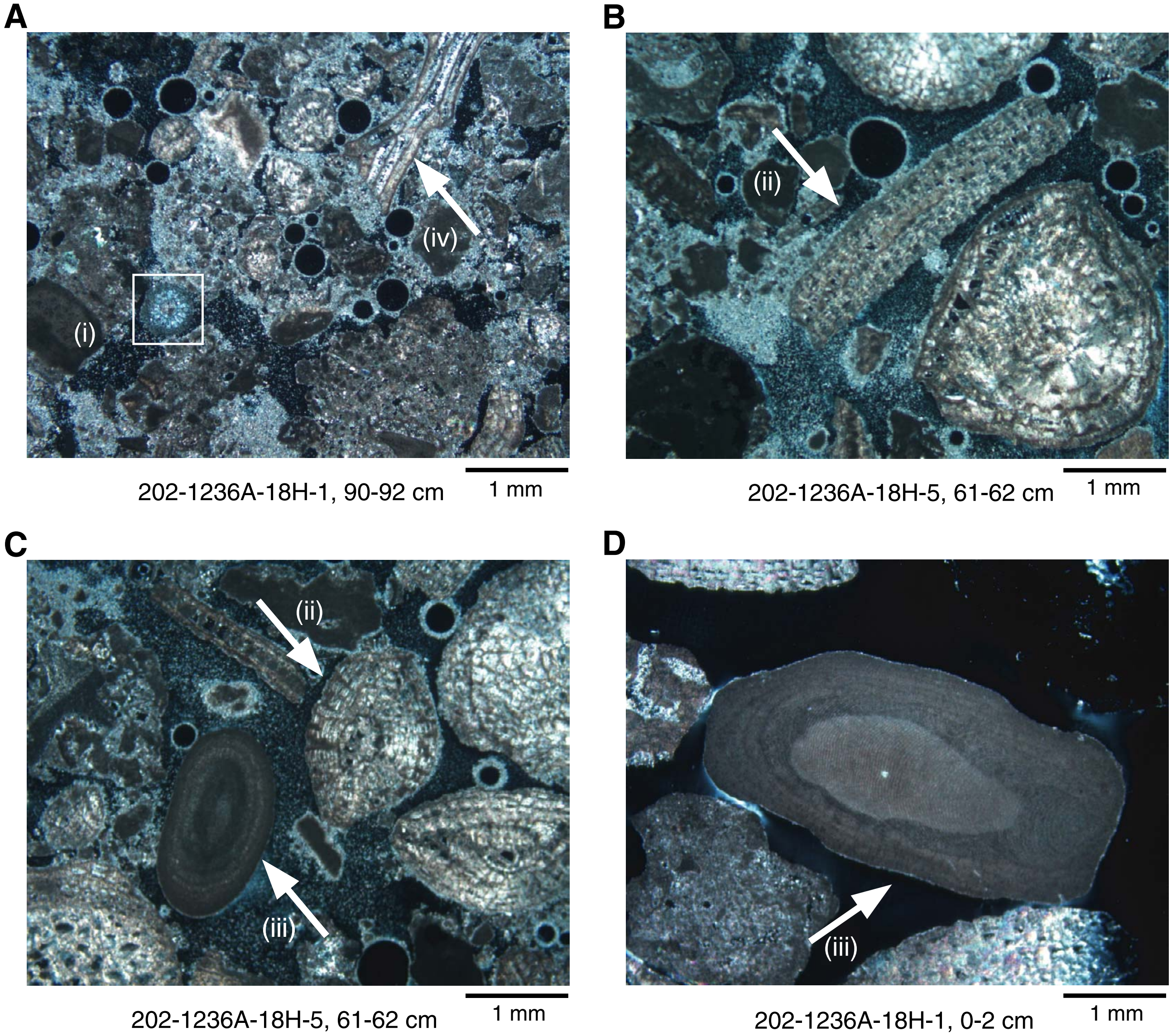

Figure F20. Close-up photograph of well-sorted and occasionally fining-upward unlithified packstone with authigenic glauconite, typical for Unit III sediments (interval 202-1236A-22X-6, 0–33 cm).

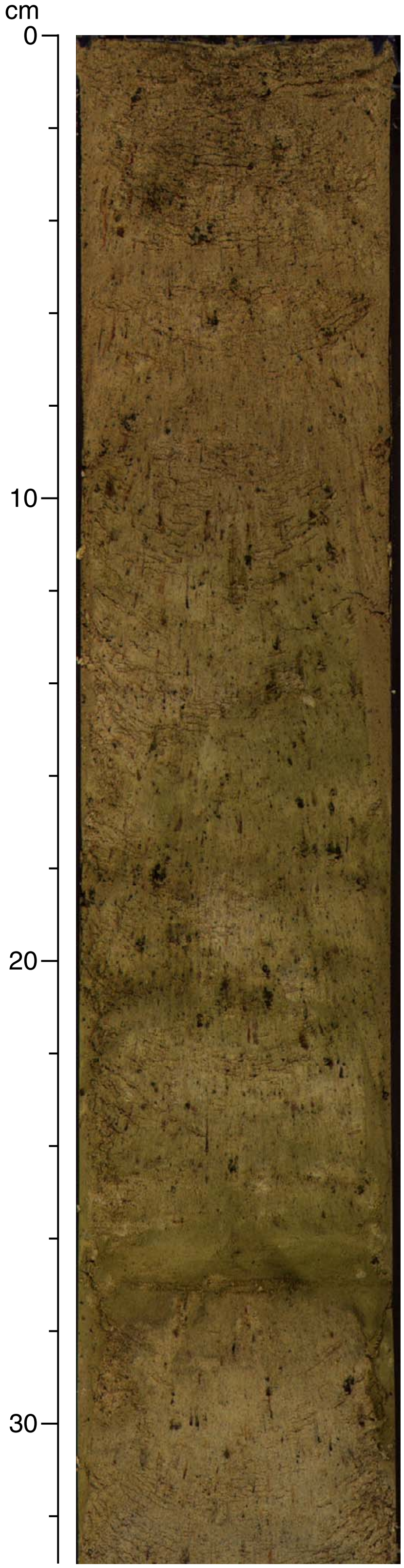

Figure F21. Close-up photograph of glauconite-bearing chalk with centimeter- to decimeter-scale color banding defining lithologic Unit IV (interval 202-1236C-23X-02, 10–47 cm).

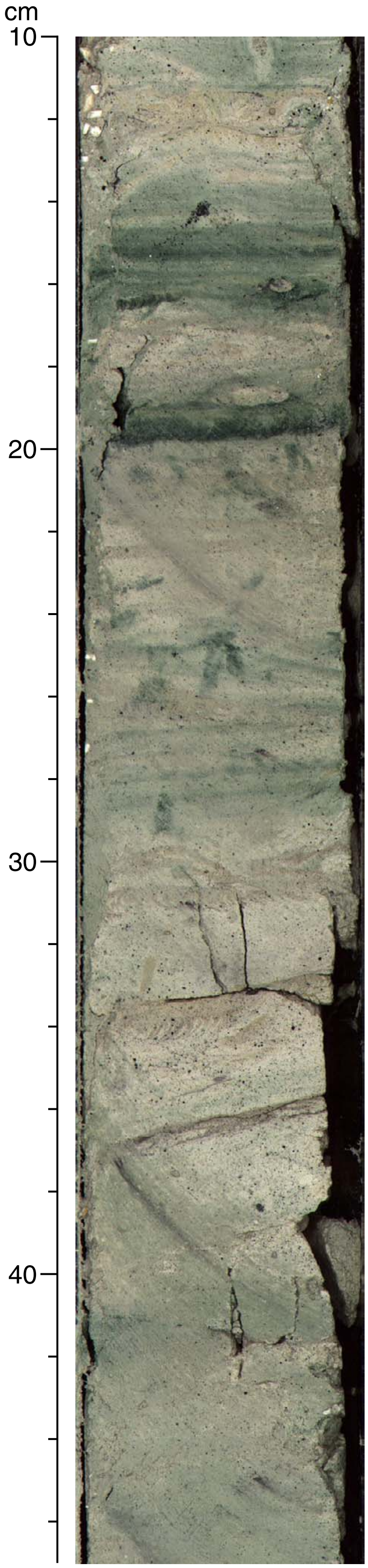

Figure F22. Summary of the depositional history of Site 1236. Red = position of volcanic ash layers. Black bars = thickness and position of nonpelagic grain–rich layers in Units I and II. * = inferred basement.

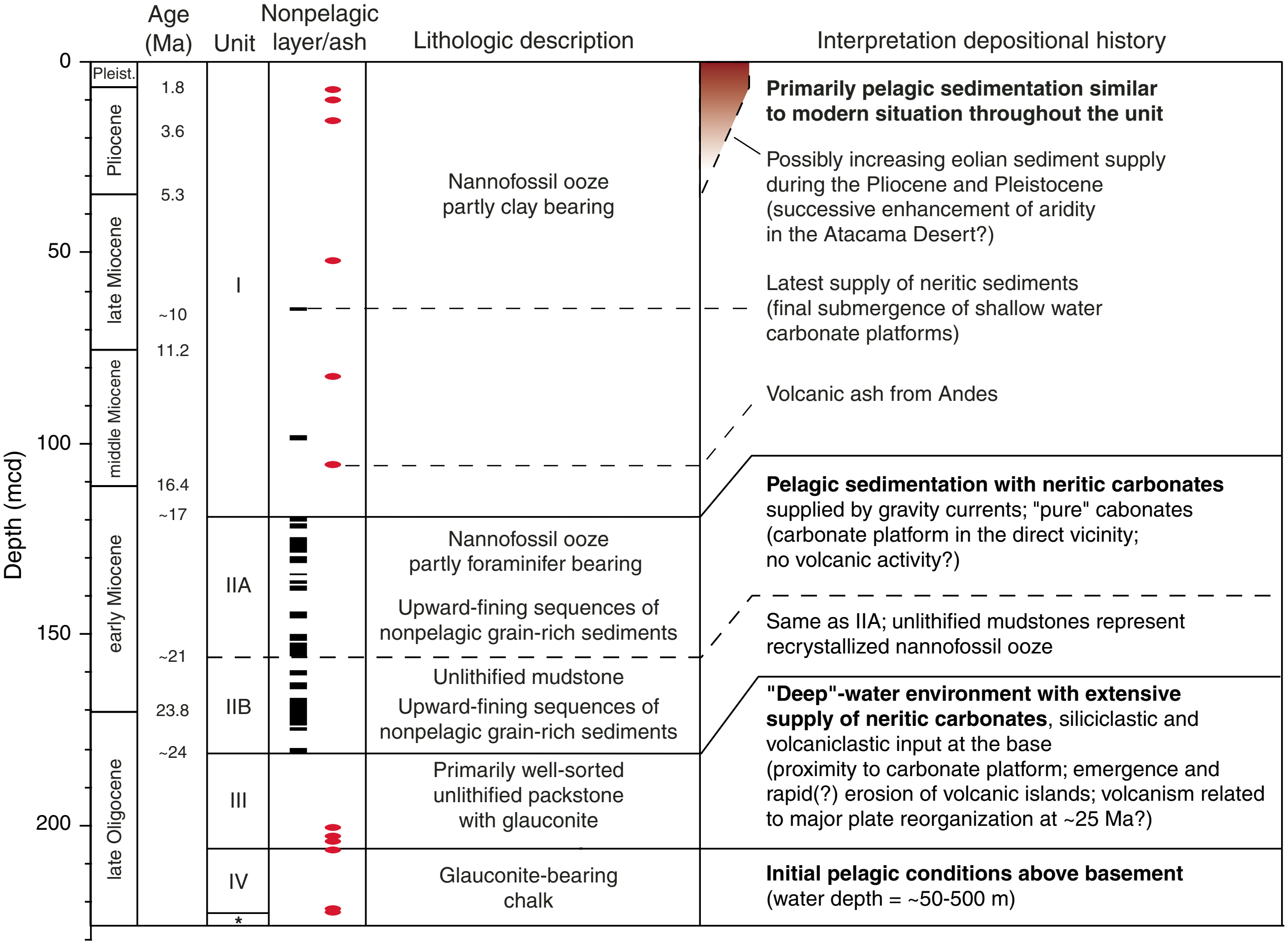

Figure F23. Core recovery, calcareous nannofossil and foraminifer abundance, and benthic foraminifer percentage of total foraminifers at Hole 1236A (smoothed lines). B = barren, R = rare, C = common, A = abundant, VA = very abundant.

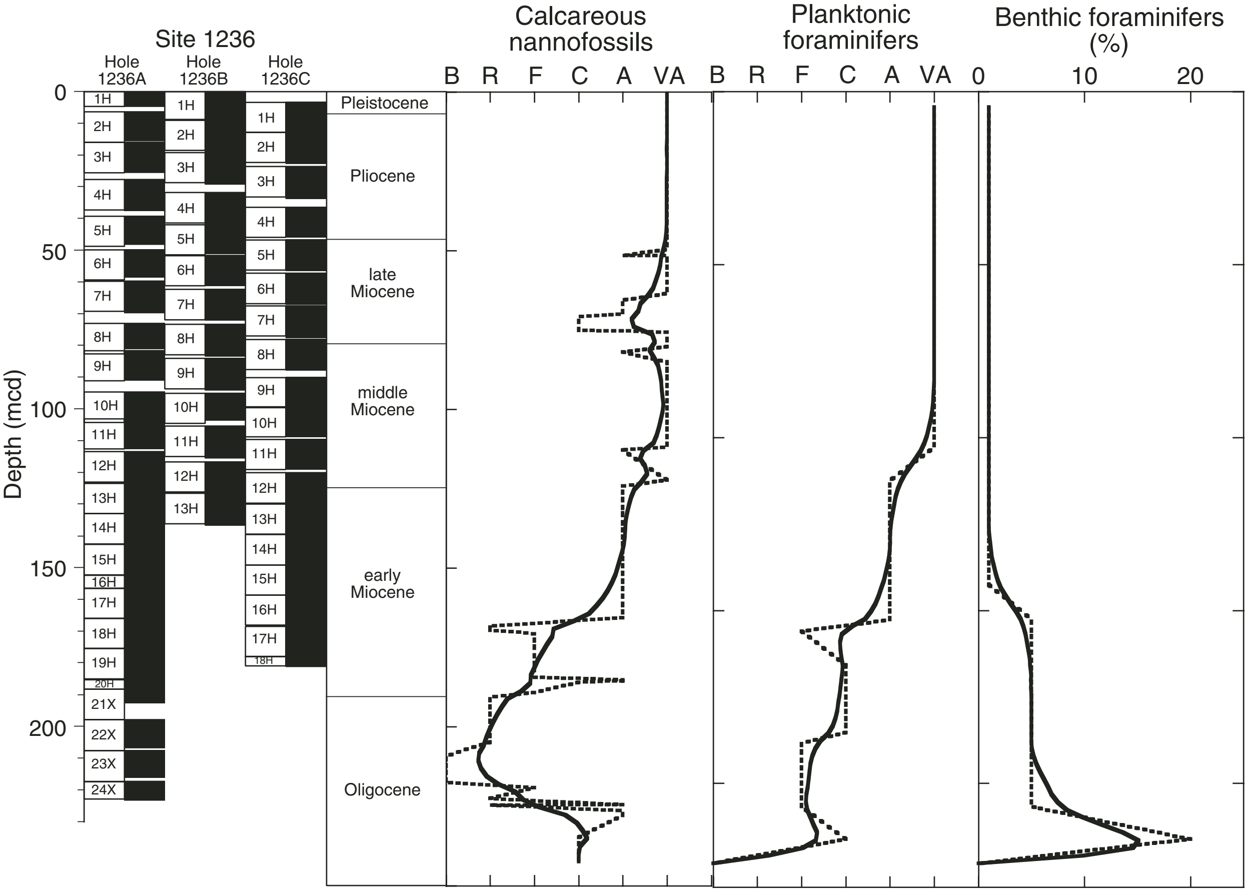

Figure F24. Site 1236 NRM intensity measured after AF demagnetization at peak fields of 20 or 25 mT vs. depth. Core recovery is shown for reference.

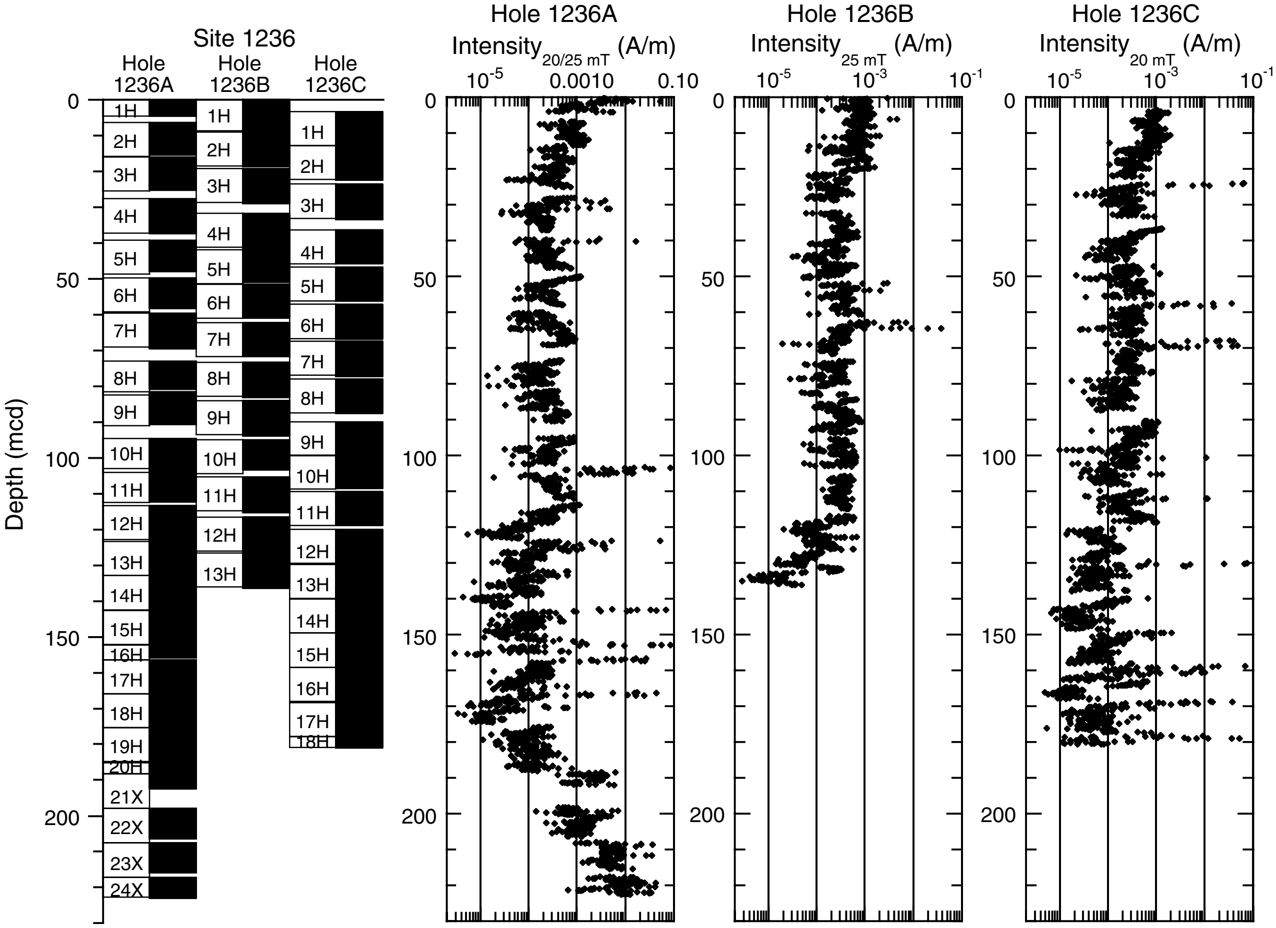

Figure F25. Site 1236 inclination after demagnetization at peak alternating fields of 20 or 25 mT vs. depth. Core recovery is shown for reference.

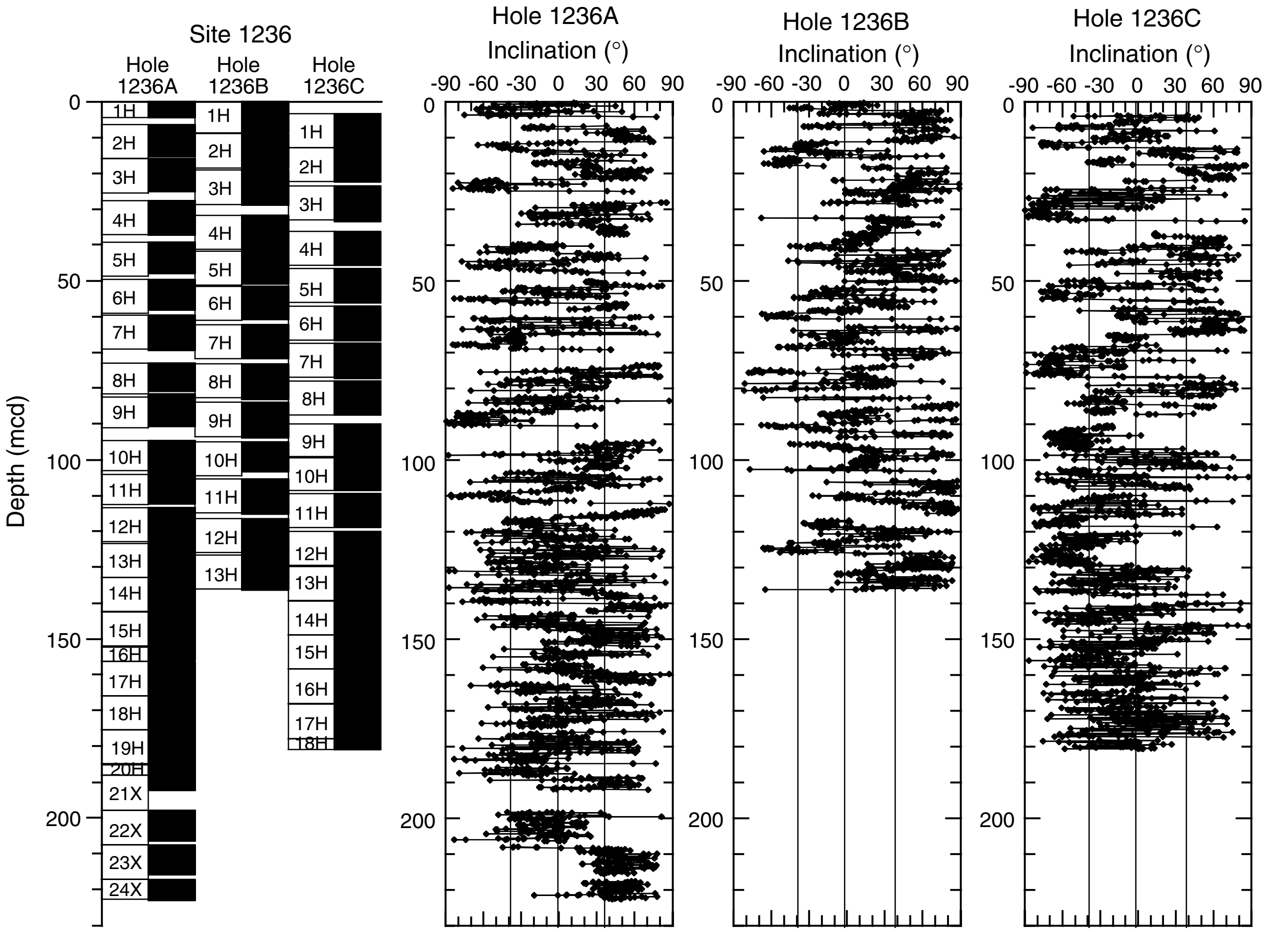

Figure F26. The inclination record after demagnetization at peak alternating fields of 20 or 25 mT for the upper 100 mcd of (**A**) Hole 1236A, (**B**) Hole 1236B, and (**C**) Hole 1236C and the (**D**) stacked and smoothed inclination data from Site 1236 and their polarity interpretation with correlation to the GPTS.

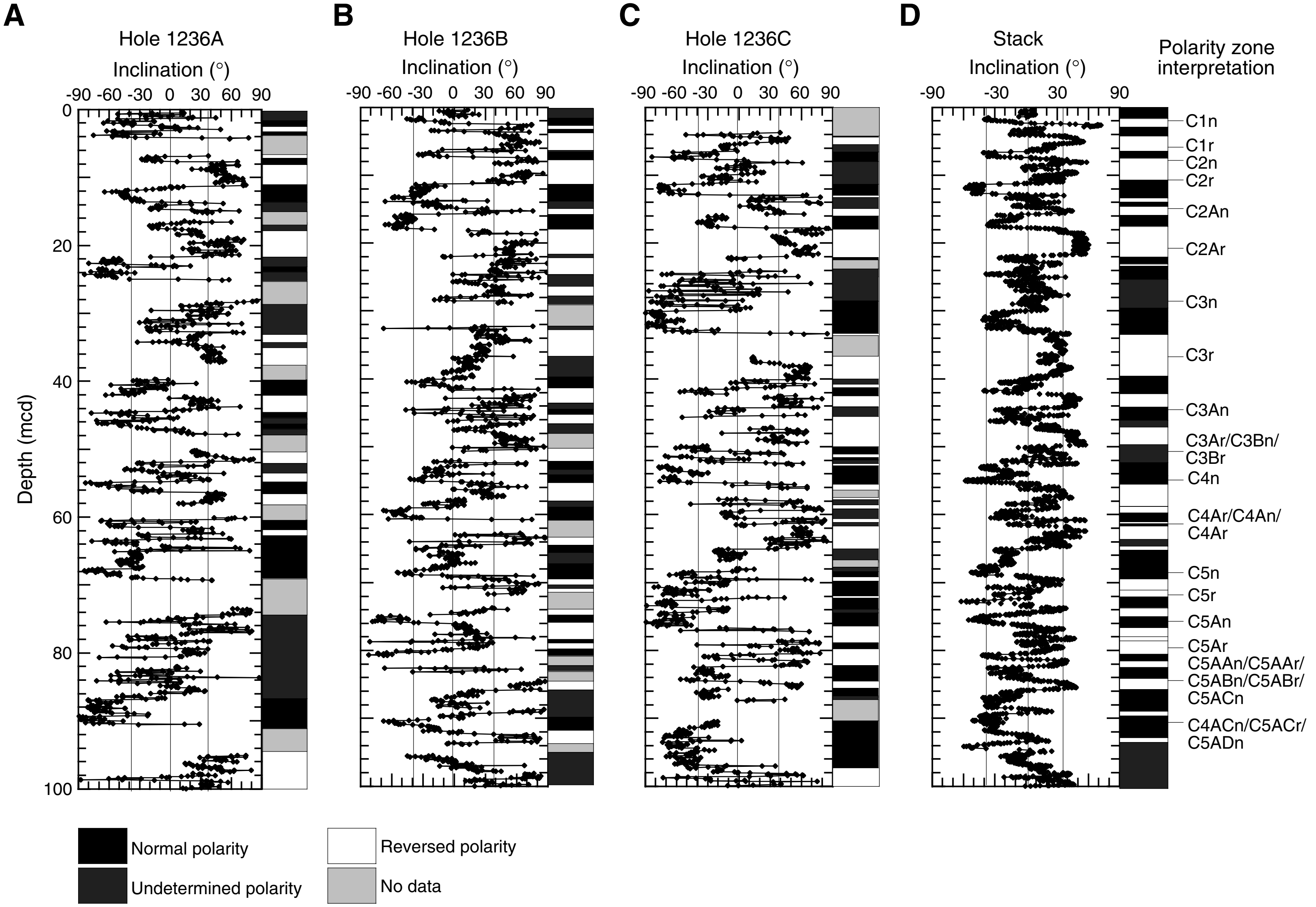

Figure F27. Interstitial water geochemical data for Site 1236. Open squares = calcium concentrations. Horizontal lines = lithologic unit boundaries (see **"Description of Lithologic Units,"** p. 5, in "Lithostratigraphy"). Values below the detection limit (0.1 µM for manganese, 2.2 µM for ammonium, and 0.22 µM for barium) are plotted at zero. Iron concentrations (not plotted) are in almost all samples below the detection limit (0.3 µM). The phosphate detection limit was 0.4 µM. Note that blank corrections for ammonium and barium were significant compared to total measured concentrations, so these profiles should be interpreted with caution. The sediment whole round used to extract the interstitial water sample at 202.3 mcd was taken ~5 cm below the top of a 38-cm-thick ash layer.

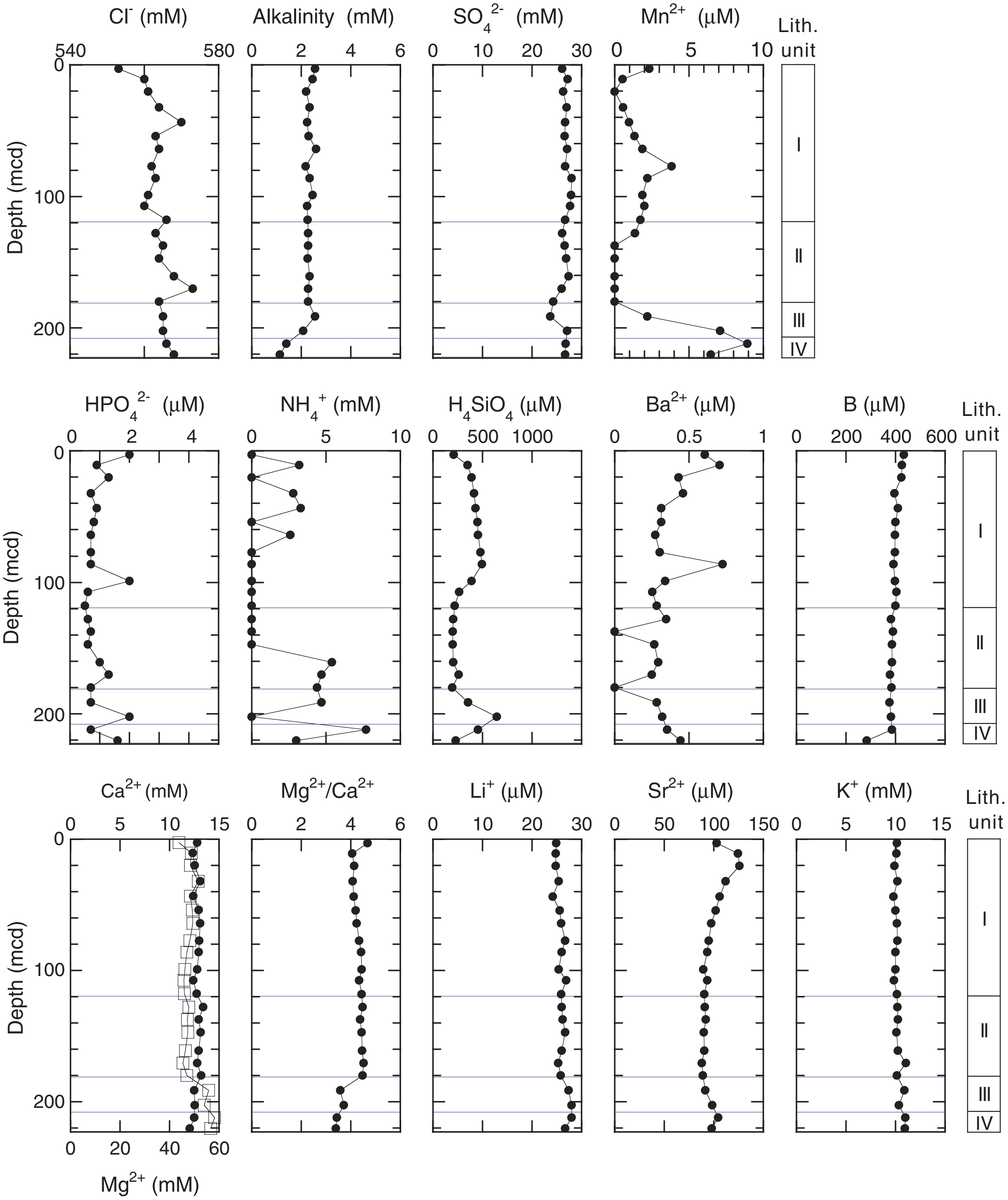

Figure F28. Calcium carbonate ($CaCO_3$) concentrations vs. depth from sediments of Site 1236. The lithologic units are adopted from **"Lithostratigraphy,"** p. 5.

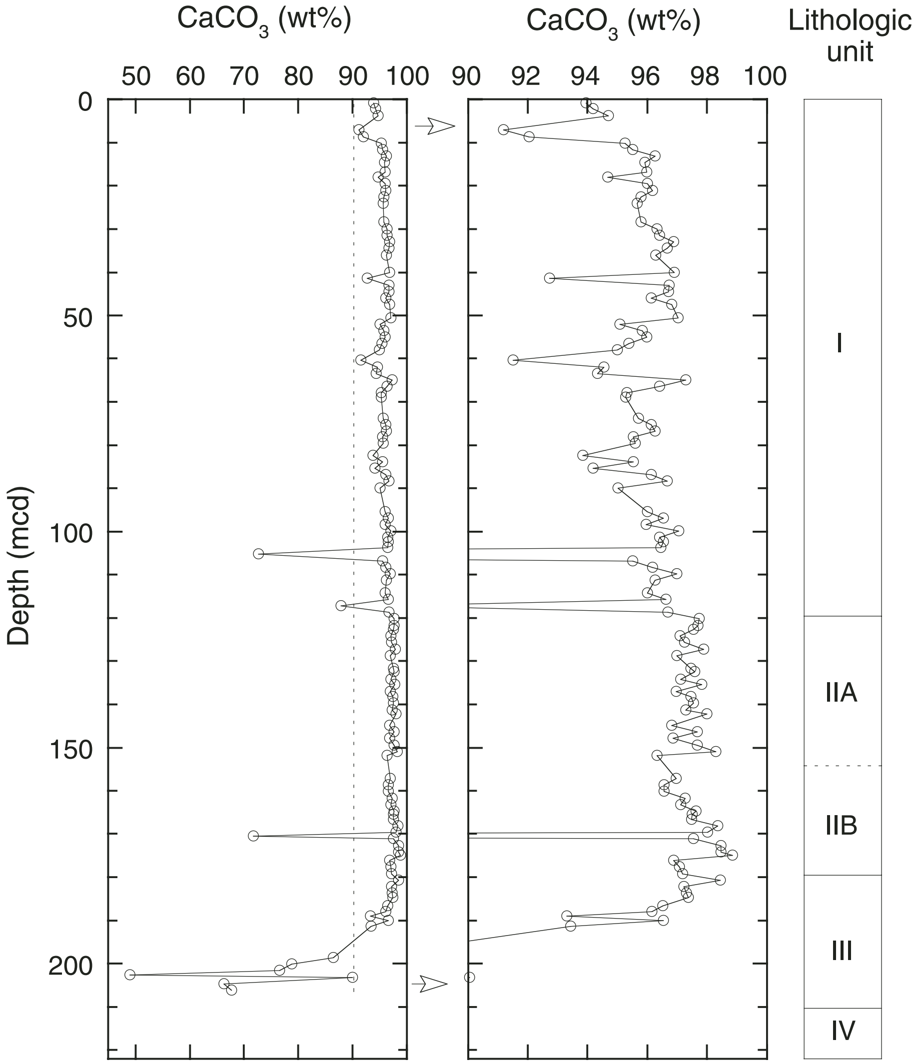

Figure F29. **A.** Shipboard biostratigraphic and magnetostratigraphic datums and age-depth model. **B.** Corrected linear sedimentation rates (LSRs), total mass accumulation rates (MARs), and carbonate MARs are calculated from the smooth age model, average dry density, and calcium carbonate concentrations at 1-m.y. intervals. Shaded areas represent time period influenced by downslope. FO = first occurrence, LO = last occurrence.

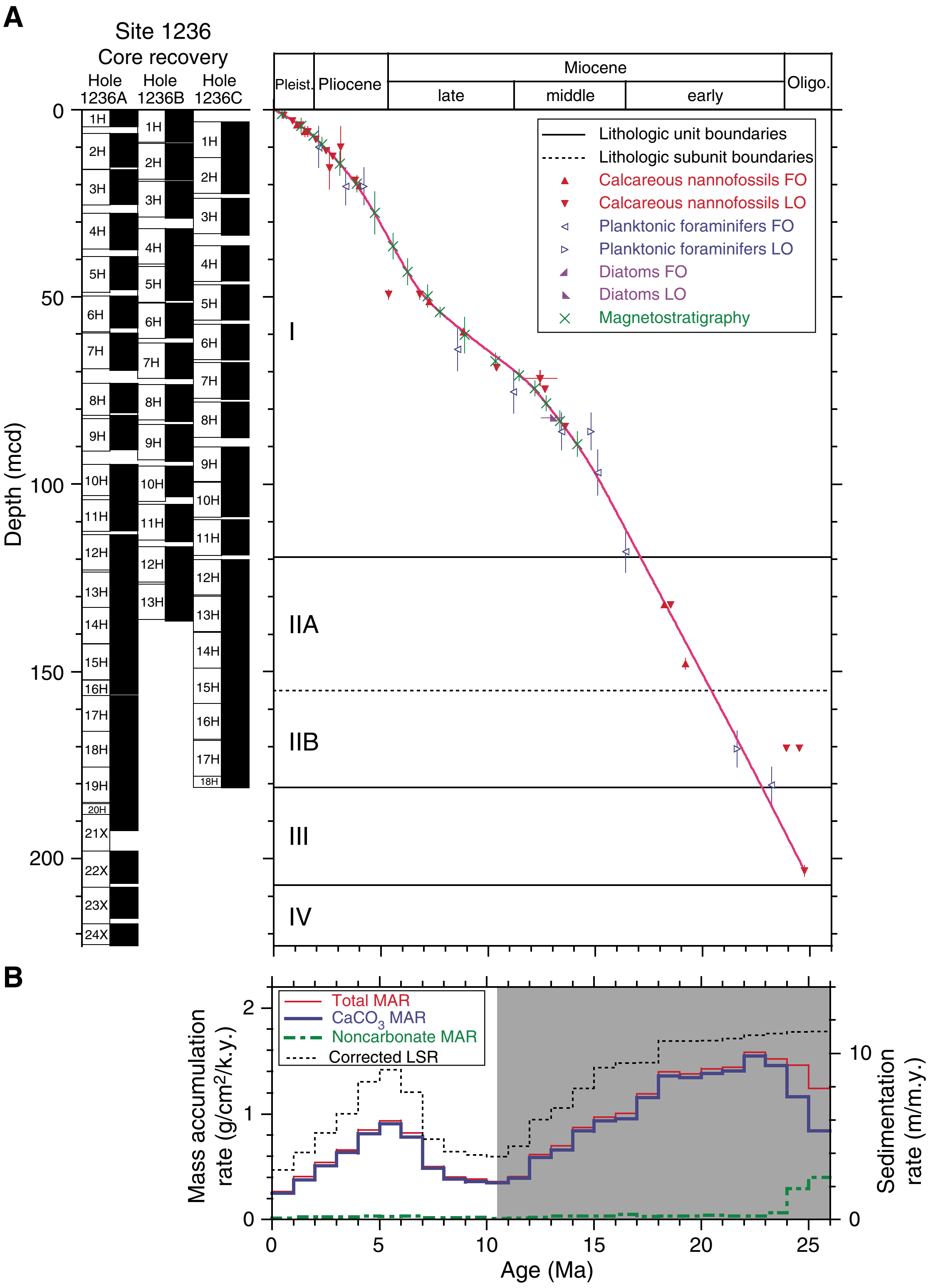

Table T1. Operations summary, Site 1236.

Core	Date (Apr 2002)	Local time (hr)	Depth (mbsf)		Length (m)		Recovery (%)	APCT	Orientation	NMCB
			Top	Bottom	Cored	Recovered				
202-1236A-										
1H	22	1825	0.0	4.6	4.6	4.61	100.2			
2H	22	1910	4.6	14.1	9.5	9.09	95.7			X
3H	22	1935	14.1	23.6	9.5	9.41	99.1			
4H	22	2040	23.6	33.1	9.5	9.76	102.7	X	Tensor	X
5H	22	2115	33.1	42.6	9.5	8.90	93.7		Tensor	
6H	22	2155	42.6	52.1	9.5	8.63	90.8	X	Tensor	X
7H	22	2235	52.1	61.6	9.5	9.97	105.0		Tensor	
8H	22	2330	61.6	71.1	9.5	7.97	83.9	X	Tensor	X
9H	22	2355	71.1	80.6	9.5	9.24	97.3		Tensor	
10H	23	0050	80.6	90.1	9.5	8.24	86.7	X	Tensor	X
11H	23	0200	90.1	99.6	9.5	9.47	99.7		Tensor	
12H	23	0240	99.6	109.1	9.5	10.01	105.4		Tensor	X
13H	23	0315	109.1	118.6	9.5	9.38	98.7		Tensor	
14H	23	0355	118.6	128.1	9.5	9.68	101.9		Tensor	X
15H	23	0435	128.1	137.6	9.5	9.78	103.0		Tensor	
16H	23	0510	137.6	141.6	4.0	3.64	91.0		Tensor	X
17H	23	0615	141.6	151.1	9.5	9.49	99.9		Tensor	
18H	23	0700	151.1	160.6	9.5	9.48	99.8		Tensor	X
19H	23	0735	160.6	170.1	9.5	9.79	103.1		Tensor	
20H	23	0820	170.1	173.1	3.0	3.27	109.0		Tensor	X
21X	23	0930	173.1	182.8	9.7	4.39	45.3			
22X	23	1010	182.8	192.5	9.7	8.72	89.9			
23X	23	1045	192.5	202.2	9.7	8.44	87.0			
24X	23	1155	202.2	207.7	5.5	5.87	106.7			
				Cored totals:	207.7	197.23	95.0			
202-1236B-										
1H	23	1510	0.0	8.8	8.8	8.85	100.6			X
2H	23	1540	8.8	18.3	9.5	9.81	103.3			
3H	23	1620	18.3	27.8	9.5	9.93	104.5		Tensor	X
4H	23	1650	27.8	37.3	9.5	10.03	105.6		Tensor	
5H	23	1720	37.3	46.8	9.5	9.10	95.8		Tensor	X
6H	23	1750	46.8	56.3	9.5	9.47	99.7		Tensor	
7H	23	1825	56.3	65.8	9.5	9.61	101.2		Tensor	X
8H	23	1855	65.8	75.3	9.5	9.97	105.0		Tensor	
9H	23	1935	75.3	84.8	9.5	9.93	104.5		Tensor	X
10H	23	2005	84.8	94.3	9.5	8.42	88.6		Tensor	
11H	23	2100	94.3	103.8	9.5	10.00	105.3	X	Tensor	X
12H	23	2135	103.8	113.3	9.5	10.01	105.4		Tensor	
13H	23	2245	113.3	122.8	9.5	9.97	105.0	X	Tensor	X
				Cored totals:	122.8	125.10	101.9			
202-1236C-										
1H	24	1315	2.8	12.3	9.5	10.00	105.3			
2H	24	1345	12.3	21.8	9.5	9.79	103.1			X
3H	24	1415	21.8	31.3	9.5	10.03	105.6		Tensor	
4H	24	1445	31.3	40.8	9.5	9.53	100.3		Tensor	X
5H	24	1515	40.8	50.3	9.5	9.65	101.6		Tensor	
6H	24	1540	50.3	59.8	9.5	9.71	102.2		Tensor	X
7H	24	1615	59.8	69.3	9.5	9.94	104.6		Tensor	
8H	24	1645	69.3	78.8	9.5	9.64	101.5		Tensor	X
9H	24	1710	78.8	88.3	9.5	9.58	100.8		Tensor	
10H	24	1735	88.3	97.8	9.5	9.49	99.9		Tensor	X
11H	24	1825	97.8	107.3	9.5	9.47	99.7		Tensor	
12H	24	1853	107.3	116.8	9.5	9.77	102.8		Tensor	X
13H	24	1925	116.8	126.3	9.5	9.74	102.5		Tensor	
14H	24	1955	126.3	135.8	9.5	9.46	99.6		Tensor	X
15H	24	2035	135.8	145.3	9.5	9.53	100.3		Tensor	
16H	24	2145	145.3	154.8	9.5	9.81	103.3		Tensor	X
17H	24	2216	154.8	164.3	9.5	9.39	98.8		Tensor	
18H	24	2255	164.3	167.3	3.0	3.21	107.0		Tensor	X
				Cored totals:	164.5	167.74	102.0			
				Site totals:	495.0	490.07	99.0			

Notes: APCT = advanced piston corer temperature tool (stainless steel housing is cutting shoe). NMCB = nonmagnetic core barrel, including cutting shoe (made from monel). X = APCT or NMCB was used. Tensor = brand name for core-barrel orientation tool.

Table T2. Composite depth scale, Site 1236.

	Depth of core top		Depth offset		Translation to cmcd	
Core	Drillers (mbsf)	Composite (mcd)	Cumulative (m)	Differential (m)	Growth factor*	Depth (cmcd)†
202-1236A-						
1H	0.0	0.03	0.03		1.14	0.03
2H	4.6	6.41	1.81	1.78	1.14	5.62
3H	14.1	16.01	1.91	0.10	1.14	14.04
4H	23.6	27.72	4.12	2.21	1.14	24.32
5H	33.1	39.29	6.19	2.07	1.14	34.46
6H	42.6	49.78	7.18	0.99	1.14	43.67
7H	52.1	59.67	7.57	0.39	1.14	52.34
8H	61.6	73.08	11.48	3.91	1.14	64.11
9H	71.1	81.63	10.53	–0.95	1.14	71.61
10H	80.6	94.68	14.08	3.55	1.14	83.05
11H	90.1	103.03	12.93	–1.15	1.14	90.38
12H	99.6	113.46	13.86	0.93	1.14	99.53
13H	109.1	123.47	14.37	0.51	1.14	108.31
14H	118.6	132.97	14.37	0.00	ND	ND
15H	128.1	142.65	14.55	0.18	ND	ND
16H	137.6	152.43	14.83	0.28	ND	ND
17H	141.6	156.43	14.83	0.00	ND	ND
18H	151.1	165.93	14.83	0.00	ND	ND
19H	160.6	175.43	14.83	0.00	ND	ND
20H	170.1	185.22	15.12	0.29	ND	ND
21X	173.1	188.22	15.12	0.00	ND	ND
22X	182.8	197.92	15.12	0.00	ND	ND
23X	192.5	207.62	15.12	0.00	ND	ND
24X	202.2	217.32	15.12	0.00	ND	ND
202-1236B-						
1H	0.0	0.00	0.00		1.14	0.00
2H	8.8	9.07	0.27	0.27	1.14	7.96
3H	18.3	19.22	0.92	0.65	1.14	16.86
4H	27.8	31.81	4.01	3.09	1.14	27.90
5H	37.3	41.92	4.62	0.61	1.14	36.77
6H	46.8	51.62	4.82	0.20	1.14	45.28
7H	56.3	62.34	6.04	1.22	1.14	54.68
8H	65.8	73.35	7.55	1.51	1.14	64.34
9H	75.3	84.08	8.78	1.23	1.14	73.75
10H	84.8	95.06	10.26	1.48	1.14	83.39
11H	94.3	105.42	11.12	0.86	1.14	92.47
12H	103.8	116.59	12.79	1.67	1.14	102.27
13H	113.3	126.60	13.30	0.51	1.14	111.05
202-1236C-						
1H	2.8	3.36	0.56		1.14	2.95
2H	12.3	12.85	0.55	–0.01	1.14	11.27
3H	21.8	23.64	1.84	1.29	1.14	20.74
4H	31.3	36.37	5.07	3.23	1.14	31.90
5H	40.8	46.75	5.95	0.88	1.14	41.01
6H	50.3	57.25	6.95	1.00	1.14	50.22
7H	59.8	67.54	7.74	0.79	1.14	59.25
8H	69.3	78.09	8.79	1.05	1.14	68.50
9H	78.8	90.05	11.25	2.46	1.14	78.99
10H	88.3	99.23	10.93	–0.32	1.14	87.04
11H	97.8	109.52	11.72	0.79	1.14	96.07
12H	107.3	120.08	12.78	1.06	1.14	105.33
13H	116.8	129.85	13.05	0.27	1.14	113.90
14H	126.3	139.59	13.29	0.24	ND	ND
15H	135.8	149.09	13.29	0.00	ND	ND
16H	145.3	158.59	13.29	0.00	ND	ND
17H	154.8	168.40	13.60	0.31	ND	ND
18H	164.3	177.90	13.60	0.00	ND	ND

Notes: * = calculated based on mbsf-mcd relationship for splice shown in Figure F10, p. 38. † = within the splice, the following equations apply: cmcd = mcd/growth factor, mcd = mbsf + cumulative depth offset, mcd = cmcd × growth factor; mbsf = cmcd × growth factor – cumulative offset. ND = not defined. This table is also available in ASCII.

Table T3. Splice tie points, Site 1236.

Hole, core, section, interval (cm)	Depth				Hole, core, section, interval (cm)	Depth		
	(mbsf)	(mcd)	(cmcd)			(mbsf)	(mcd)	(cmcd)
202-					202-			
1236B-1H-5, 77.5	6.82	6.82	5.98	Tie to	1236C-1H-3, 44.5	6.26	6.82	5.98
1236C-1H-7, 5.0	11.85	12.41	10.89	Tie to	1236B-2H-3, 31.0	12.14	12.41	10.89
1236B-2H-5, 85.0	15.68	15.95	13.99	Tie to	1236C-2H-3, 10.0	15.40	15.95	13.99
1236C-2H-6, 52.5	20.33	20.88	18.32	Tie to	1236B-3H-2, 15.0	19.96	20.88	18.32
1236B-3H-5, 52.5	24.87	25.79	22.62	Tie to	1236C-3H-2, 65.0	23.95	25.79	22.62
1236C-3H-4, 125.0	27.55	29.39	25.78	Tie to	1236A-4H-2, 15.0	25.27	29.39	25.78
1236A-4H-5, 45.0	30.11	34.23	30.03	Tie to	1236B-4H-2, 89.5	30.22	34.23	30.03
1236B-4H-5, 50.0	34.33	38.34	33.63	Tie to	1236C-4H-2, 46.0	33.27	38.34	33.63
1236C-4H-5, 45.0	37.75	42.82	37.56	Tie to	1236B-5H-1, 90.0	38.20	42.82	37.56
1236B-5H-5, 125.0	44.58	49.20	43.16	Tie to	1236C-5H-2, 95.0	43.25	49.20	43.16
1236C-5H-4, 147.5	46.78	52.73	46.25	Tie to	1236B-6H-1, 109.5	47.91	52.73	46.25
1236B-6H-5, 147.5	54.32	59.14	51.88	Tie to	1236C-6H-2, 38.5	52.19	59.14	51.88
1236C-6H-5, 72.5	57.03	63.98	56.12	Tie to	1236B-7H-2, 12.5	57.94	63.98	56.12
1236B-7H-5, 57.5	62.90	68.94	60.47	Tie to	1236C-7H-1, 140.0	61.20	68.94	60.47
1236C-7H-5, 90.0	66.70	74.44	65.30	Tie to	1236B-8H-1, 108.5	66.89	74.44	65.30
1236B-8H-6, 20.0	73.56	81.11	71.15	Tie to	1236C-8H-3, 0.5	72.32	81.11	71.15
1236C-8H-6, 127.5	78.08	86.87	76.20	Tie to	1236B-9H-2, 127.5	78.09	86.87	76.20
1236B-9H-6, 10.0	82.96	91.74	80.47	Tie to	1236C-9H-2, 18.5	80.49	91.74	80.47
1236C-9H-6, 25.0	86.52	97.77	85.76	Tie to	1236B-10H-2, 119.0	87.51	97.77	85.76
1236B-10H-6, 15.0	92.48	102.74	90.12	Tie to	1236C-10H-3, 50.0	91.81	102.74	90.12
1236C-10H-6, 85.0	96.69	107.62	94.40	Tie to	1236B-11H-2, 70.0	96.50	107.62	94.40
1236B-11H-5, 120.0	101.52	112.64	98.81	Tie to	1236C-11H-3, 8.5	100.92	112.64	98.81
1236C-11H-6, 22.5	105.58	117.30	102.89	Tie to	1236B-12H-1, 69.5	104.51	117.30	102.89
1236B-12H-6, 95.0	112.29	125.08	109.72	Tie to	1236C-12H-4, 50.0	112.30	125.08	109.72
1236C-12H-7, 50.0	116.80	129.58	113.67					

Note: This table is also available in **ASCII**.

Table T4. OSUS-MS measurements, Hole 1236B.

Core, section, interval (cm)	Depth		Magnetic susceptibility (instrument units)	Run number	Depth from top of core (cm)
	(mbsf)	(mcd)			
202-1236B-					
7H-1, 5	56.35	62.39	1.5	919	5
7H-1, 10	56.40	62.44	1.5	919	10
7H-1, 15	56.45	62.49	1.5	919	15
7H-1, 20	56.50	62.54	1.5	919	20
7H-1, 25	56.55	62.59	1.6	919	25
7H-1, 30	56.60	62.64	1.4	919	30
7H-1, 35	56.65	62.69	1.1	919	35
7H-1, 40	56.70	62.74	1.0	919	40
7H-1, 45	56.75	62.79	1.3	919	45
7H-1, 50	56.80	62.84	1.6	919	50
7H-1, 55	56.85	62.89	1.8	919	55
7H-1, 60	56.90	62.94	2.0	919	60
7H-1, 65	56.95	62.99	1.8	919	65
7H-1, 70	57.00	63.04	1.7	919	70
7H-1, 75	57.05	63.09	1.8	919	75
7H-1, 80	57.10	63.14	1.7	919	80
7H-1, 85	57.15	63.19	1.8	919	85
7H-1, 90	57.20	63.24	2.0	919	90
7H-1, 95	57.25	63.29	2.5	919	95
7H-1, 100	57.30	63.34	1.9	919	100
7H-1, 105	57.35	63.39	1.8	919	105
7H-1, 110	57.40	63.44	1.9	919	110
7H-1, 115	57.45	63.49	1.8	919	115
7H-1, 120	57.50	63.54	1.9	919	120
7H-1, 125	57.55	63.59	2.3	919	125
7H-1, 130	57.60	63.64	2.5	919	130
7H-1, 135	57.65	63.69	3.0	919	135
7H-1, 140	57.70	63.74	14.9	919	140
7H-1, 145	57.75	63.79	3.7	919	145
7H-2, 5	57.86	63.90	2.0	920	155
7H-2, 10	57.91	63.95	1.8	920	160
7H-2, 15	57.96	64.00	1.6	920	165
7H-2, 20	58.01	64.05	1.9	920	170
7H-2, 25	58.06	64.10	2.1	920	175
7H-2, 30	58.11	64.15	2.1	920	180
7H-2, 35	58.16	64.20	1.9	920	185
7H-2, 40	58.21	64.25	1.4	920	190
7H-2, 45	58.26	64.30	1.3	920	195
7H-2, 50	58.31	64.35	1.4	920	200
7H-2, 55	58.36	64.40	1.5	920	205
7H-2, 60	58.41	64.45	1.1	920	210
7H-2, 65	58.46	64.50	0.8	920	215
7H-2, 70	58.51	64.55	0.5	920	220
7H-2, 75	58.56	64.60	0.5	920	225
7H-2, 80	58.61	64.65	1.0	920	230
7H-2, 85	58.66	64.70	0.2	920	235
7H-2, 90	58.71	64.75	0.1	920	240
7H-2, 95	58.76	64.80	0.2	920	245
7H-2, 100	58.81	64.85	0.3	920	250
7H-2, 105	58.86	64.90	0.9	920	255
7H-2, 110	58.91	64.95	0.0	920	260
7H-2, 115	58.96	65.00	0.1	920	265
7H-2, 120	59.01	65.05	1.0	920	270
7H-2, 125	59.06	65.10	1.1	920	275
7H-2, 130	59.11	65.15	1.0	920	280
7H-2, 135	59.16	65.20	1.1	920	285
7H-2, 140	59.21	65.25	1.2	920	290
7H-2, 145	59.26	65.30	1.2	920	295
7H-3, 5	59.36	65.40	1.6	921	305
7H-3, 10	59.41	65.45	1.6	921	310
7H-3, 15	59.46	65.50	1.4	921	315
7H-3, 20	59.51	65.55	1.3	921	320
7H-3, 25	59.56	65.60	1.4	921	325

Note: Only a portion of this table appears here. The complete table is available in ASCII.

Table T5. OSUS-MS measurements, Hole 1236C.

Core, section, interval (cm)	Depth (mbsf)	Depth (mcd)	Magnetic susceptibility (instrument units)	Run number	Depth from top of core (cm)
202-1236C-					
1H-1, 5	2.85	3.41	3.0	926	5
1H-1, 10	2.90	3.46	2.4	926	10
1H-1, 15	2.95	3.51	2.3	926	15
1H-1, 20	3.00	3.56	2.4	926	20
1H-1, 25	3.05	3.61	2.5	926	25
1H-1, 30	3.10	3.66	2.2	926	30
1H-1, 35	3.15	3.71	2.3	926	35
1H-1, 40	3.20	3.76	2.5	926	40
1H-1, 45	3.25	3.81	2.6	926	45
1H-1, 50	3.30	3.86	6.9	926	50
1H-1, 55	3.35	3.91	2.3	926	55
1H-1, 60	3.40	3.96	2.0	926	60
1H-1, 65	3.45	4.01	2.0	926	65
1H-1, 70	3.50	4.06	1.9	926	70
1H-1, 75	3.55	4.11	1.9	926	75
1H-1, 80	3.60	4.16	2.1	926	80
1H-1, 85	3.65	4.21	2.0	926	85
1H-1, 90	3.70	4.26	2.0	926	90
1H-1, 95	3.75	4.31	1.8	926	95
1H-1, 100	3.80	4.36	1.9	926	100
1H-1, 105	3.85	4.41	2.7	926	105
1H-1, 110	3.90	4.46	4.1	926	110
1H-1, 115	3.95	4.51	3.0	926	115
1H-1, 120	4.00	4.56	1.8	926	120
1H-1, 125	4.05	4.61	1.5	926	125
1H-1, 130	4.10	4.66	1.5	926	130
1H-1, 135	4.15	4.71	1.2	926	135
1H-1, 140	4.20	4.76	1.1	926	140
1H-1, 145	4.25	4.81	1.1	926	145
1H-2, 5	4.36	4.92	1.9	927	156
1H-2, 10	4.41	4.97	1.9	927	161
1H-2, 15	4.46	5.02	1.9	927	166
1H-2, 20	4.51	5.07	2.1	927	171
1H-2, 25	4.56	5.12	1.9	927	176
1H-2, 30	4.61	5.17	2.0	927	181
1H-2, 35	4.66	5.22	1.9	927	186
1H-2, 40	4.71	5.27	1.9	927	191
1H-2, 45	4.76	5.32	2.1	927	196
1H-2, 50	4.81	5.37	2.2	927	201
1H-2, 55	4.86	5.42	2.1	927	206
1H-2, 60	4.91	5.47	2.0	927	211
1H-2, 65	4.96	5.52	1.9	927	216
1H-2, 70	5.01	5.57	2.0	927	221
1H-2, 75	5.06	5.62	2.0	927	226
1H-2, 80	5.11	5.67	1.7	927	231
1H-2, 85	5.16	5.72	1.8	927	236
1H-2, 90	5.21	5.77	2.1	927	241
1H-2, 95	5.26	5.82	2.2	927	246
1H-2, 100	5.31	5.87	2.3	927	251
1H-2, 105	5.36	5.92	2.4	927	256
1H-2, 110	5.41	5.97	2.5	927	261
1H-2, 115	5.46	6.02	2.4	927	266
1H-2, 120	5.51	6.07	2.1	927	271
1H-2, 125	5.56	6.12	2.0	927	276
1H-2, 130	5.61	6.17	1.7	927	281
1H-2, 135	5.66	6.22	1.7	927	286
1H-2, 140	5.71	6.27	1.8	927	291
1H-2, 145	5.76	6.32	1.9	927	296
1H-3, 5	5.87	6.43	2.4	928	306
1H-3, 10	5.92	6.48	2.4	928	311
1H-3, 15	5.97	6.53	2.4	928	316
1H-3, 20	6.02	6.58	2.3	928	321
1H-3, 25	6.07	6.63	2.3	928	326

Note: Only a portion of this table appears here. The complete table is available in ASCII.

Table T6. Lithologic units, Site 1236.

Unit/ Subunit	Top			Base			Description	Interpretation
	Core, section, interval (cm)	Depth		Core, section, interval (cm)	Depth			
		(mbsf)	(mcd)		(mbsf)	(mcd)		
	202-			202-				
I	1236A-1H-1, 0	0.0	0.0	1236A-12H-5, 0	105.6	119.5	Nannofossil ooze, rich in foraminifers, partly clay bearing	Pelagic sedimentation
	1236B-1H-1, 0	0.0	0.0	1236B-12H-2, 69	106.0	118.8		
	1236C-1H-1, 0	2.8	3.4	1236C-11H-7, 56	106.9	118.7		
II	1236A-12H-5, 0	105.6	119.5	1236A-19H-4, 100	166.1	180.9	Nannofossil ooze, unlithified mudstone, nonpelagic grain-rich intervals	Pelagic sedimentation with allochthonous supply of neritic carbonates
	1236B-12H2, 69	106.0	118.8	1236B-13H-CC, 18	122.8	136.7		
	1236C-11H-7, 56	106.9	118.7	1236C-18H-CC, 21	167.3	180.9		
IIA	1236A-12H-5, 0	105.6	119.5	1236A-16H-1, 79	138.4	153.2	Nannofossil ooze, partly foraminifer bearing, nonpelagic grain-rich intervals	Pelagic sedimentation with allochthonous supply of neritic carbonates
	1236B-12H-2, 69	106.0	118.8	1236B-13H-CC, 18	122.8	136.7		
	1236C-11H-7, 56	106.9	118.7	1236C-15H-5, 0	141.8	155.1		
IIB	1236A-16H-1, 79	138.4	153.2	1236A-19H-4, 100	166.1	180.9	Unlithified mudstone, partly foraminifer bearing, nonpelagic grain-rich intervals	Pelagic sedimentation with allochthonous neritic carbonates
	1236C-15H-5, 0	141.8	155.1	1236C-18H-CC, 21	167.3	180.9		
III	1236A-19H-4, 100	166.1	180.9	1236A-22X-CC, 40	191.6	206.5	Primarily well sorted, unlithified packstone with glauconite	Water depth ~50–500 m, allochthonous neritic carbonates
IV	1236A-23X-1, 0	192.5	207.6	1236A-23X-4, 45	207.2	222.3	Glauconite-bearing chalk	Pelagic sedimentation, water depth ~50–500 m

Table T7. Age-depth control points, Hole 1236A.

		Age (Ma)		Top sample (FO presence/LO absence)		Bottom sample (LO presence/FO absence)		Age (Ma)		Depth		
Datum	Source	Minimum	Maximum	Core, section, interval (cm)	Depth (mbsf)	Core, section, interval (cm)	Depth (mbsf)	Average	Uncertainty (±)	Average (mbsf)	Average (mcd)	Uncertainty (±m)
				202-1236A-		202-236A-						
LO *Pseudoemiliania lacunosa*	CN	0.46	0.46	1H-1, 75	0.75	1H-2, 75	2.25	0.46	0.00	1.50	1.53	0.75
LO *Reticulofenestra asanoi*	CN	0.88	0.88	1H-2, 75	2.25	1H-3, 75	3.76	0.88	0.00	3.01	3.04	0.76
FO *Reticulofenestra asanoi*	CN	1.08	1.08	1H-3, 75	3.76	1H-CC, 13	4.57	1.08	0.00	4.17	4.20	0.41
LO *Gephyrocapsa* (large)	CN	1.24	1.24	1H-3, 75	3.76	1H-CC, 13	4.57	1.24	0.00	4.17	4.20	0.41
FO *Gephyrocapsa* (large)	CN	1.45	1.45	1H-CC, 13	5.57	2H-1, 76	5.36	1.45	0.00	5.47	5.89	–0.11
LO *Calcidiscus macintyrei*	CN	1.59	1.59	1H-CC, 13	5.57	2H-1, 76	5.36	1.59	0.00	5.47	5.89	–0.11
FO *Globorotalia inflata*	PF	2.09	2.09	1H-CC, 13	5.57	2H-CC, 14	5.36	2.09	0.00	5.47	10.06	–0.11
LO *Discoaster brouweri*	CN	1.96	1.96	2H-1, 76	5.36	2H-2, 76	6.87	1.96	0.00	6.12	7.93	0.76
LO *Discoaster pentaradiatus*	CN	2.44	2.44	2H-3, 76	8.38	2H-4, 76	9.89	2.44	0.00	9.14	10.95	0.76
LO *Discoaster surculus*	CN	2.61	2.61	2H-3, 76	8.38	3H-4, 76	9.89	2.61	0.00	9.14	10.95	0.76
LO *Discoaster tamalis*	CN	2.76	2.76	2H-4, 76	9.89	2H-5, 76	11.41	2.76	0.00	10.65	12.46	0.76
LO *Sphaeroidinellopsis seminula*	CN	3.12	3.12	1H-CC, 13	5.57	2H-CC, 14	13.64	3.12	0.00	9.61	10.10	4.04
FO *Globorotalia tosaensis*	PF	3.35	3.35	2H-CC, 14	13.64	3H-CC, 13	23.46	3.35	0.00	18.55	20.48	4.91
LO *Reticulofenestra pseudoumbilicus*	CN	3.80	3.80	3H-2, 76	16.19	3H-3, 76	17.70	3.80	0.00	16.95	18.86	0.75
FO *Pseudoemiliania lacunosa*	CN	4.00	4.00	3H-3, 76	17.70	3H-4, 76	19.21	4.00	0.00	18.46	20.37	0.75
LO *Globoturborotalia nepenthes*	PF	4.20	4.20	2H-CC, 14	13.64	3H-CC, 13	23.46	4.20	0.00	18.55	20.48	4.91
LO *Triquetrorhabdulus rugosus*	CN	5.35	5.35	5H-CC, 11	41.98	6H-1, 76	43.36	5.35	0.00	42.67	49.36	0.69
LO Absence interval *Reticulofenestra pseudoumbilicus* >7 µm	CN	6.80	6.80	5H-CC, 11	41.98	6H-1, 76	43.36	6.80	0.00	42.67	49.36	0.69
FO *Amaurolithus primus*	CN	7.24	7.24	6H-1, 76	43.36	6H-2, 76	44.87	7.24	0.00	44.12	51.30	0.75
FO *Globorotalia plesiotumida*	PF	8.58	8.58	6H-CC, 13	51.82	7H-CC, 14	62.10	8.58	0.00	56.96	64.03	5.14
FO Absence interval *Reticulofenestra pseudoumbilicus* >7 µm	CN	8.85	8.85	6H-CC, 13	51.20	7H-1, 76	52.86	8.85	0.00	52.03	59.41	0.83
LO *Coccolithus miopelagicus*	CN	10.40	10.40	7H-6, 76	60.42	7H-CC, 14	62.10	10.40	0.00	61.26	68.83	0.84
FO *Globoturborotalia nepenthes*	PF	11.19	11.19	7H-CC, 14	62.10	8H-CC, 14	69.52	11.19	0.00	65.81	75.35	3.71
LO *Coronocyclus nitescens*	CN	12.43	12.43	7H-CC, 14	62.10	8H-1, 76	62.36	12.43	0.00	62.23	71.76	0.13
Coscinodiscus lewisianus Zone	D	12.47	13.51	9H-1, 64	71.74	9H-1, 66	71.76	12.99	0.52	71.75	82.28	0.01
LO *Cyclicargolithus floridanus*	CN	11.6	13.19	7H-CC, 14	62.10	8H-1, 76	62.36	12.40	0.80	62.23	71.76	0.13
LO *Calcidiscus premacintyrei*	CN	12.65	12.65	8H-1, 76	62.36	8H-2, 76	63.86	12.65	0.00	63.11	74.60	0.75
FO *Globorotalia fohsi robusta*	PF	13.42	13.42	8H-CC, 14	69.52	9H-CC, 12	80.29	13.42	0.00	74.91	85.95	5.39
LO *Sphenolithus heteromorphus*	CN	13.57	13.57	9H-2, 76	73.37	9H-3, 76	74.88	13.57	0.00	74.13	84.66	0.75
LO *Praeorbulina sicana*	PF	14.80	14.80	8H-CC, 14	69.52	9H-CC, 12	80.29	14.80	0.00	74.91	85.95	5.39
FO *Orbulina suturalis*	PF	15.10	15.10	9H-CC, 12	80.29	10H-CC, 15	88.79	15.10	0.00	84.54	96.90	4.25
FO *Praeorbulina sicana*	PF	16.40	16.40	11H-CC, 11	99.52	12H-CC, 17	109.56	16.40	0.00	104.54	118.01	5.02
FO *Sphenolithus heteromorphus*	CN	18.20	18.20	13H-6, 76	117.41	13H-CC, 1	118.38	18.20	0.00	117.90	132.27	0.48
LO *Sphenolithus belemnos*	CN	18.50	18.50	13H-6, 76	117.41	13H-CC, 1	118.38	18.50	0.00	117.90	132.27	0.48
FO *Sphenolithus belemnos*	CN	19.20	19.20	15H-3, 76	131.88	15H-5, 76	134.90	19.20	0.00	133.39	147.94	1.51
LO *Globoturborotalia angulisuturalis*	PF	21.60	21.60	17H-CC, 11	151.04	18H-CC, 16	160.56	21.60	0.00	155.80	170.68	4.76
FO *Globoquadrina dehiscens*	PF	23.20	23.20	18H-CC, 16	160.56	19H-CC, 21	170.37	23.20	0.00	165.47	180.34	4.91
LO *Reticulofenestra bisecta*	CN	23.90	23.90	18H-3, 75	154.87	18H-4, 75	156.35	23.90	0.00	155.61	170.44	0.74
LO *Zygrhabdolithus bijugatus*	CN	24.50	24.50	18H-3, 75	154.87	18H-4, 75	156.35	24.50	0.00	155.61	170.44	0.74
LO *Sphenolithus ciperoensis*	CN	24.75	24.75	22X-3, 75	186.56	22X-5, 75	189.58	24.75	0.00	188.07	203.19	1.51

Notes: FO = first occurrence, LO = last occurrence. CN = calcareous nannofossils, PF = planktonic foraminifers, D = diatoms.

Table T8. Distribution of calcareous nannofossils, Holes 1236A and 1236B. (**See table notes.** Continued on next two pages.)

Core, section, interval (cm)	Depth (mbsf)	Depth (mcd)	Preservation	Abundance	*Amaurolithus primus*	*Amaurolithus primus/delicatus*	*Calcidiscus macintyrei*	*Calcidiscus premacintyrei*	*Ceratolithus* spp.	*Coccolithus miopelagicus*	*Coronocyclus nitescens*	*Cyclicargolithus abisectus*	*Cyclicargolithus floridanus*	*Discoaster brouweri*	*Discoaster pentaradiatus*	*Discoaster surculus*	*Discoaster tamalis*	*Discoaster triradiatus*	*Discoaster variabilis* gr.	*Discoaster* spp. (5-ray)	*Emiliania huxleyi*	*Gephyrocapsa* (large)	*Gephyrocapsa* (medium)	*Gephyrocapsa* spp. (small)	*Pseudoemiliania lacunosa*	*Reticulofenestra asanoi*	*Reticulofenestra bisecta*	*Reticulofenestra pseudoumbilicus*	*Sphenolithus abies/neoabies*	*Sphenolithus belemnos*	*Sphenolithus ciperoensis*	*Sphenolithus distentus*	*Sphenolithus heteromorphus*	*Sphenolithus predistentus*	*Triquetrorhabdulus rugosus*	*Zygrhabdolithus bijugatus*
202-1236A-																																				
1H-1, 75	0.75	0.78	G	VA																			C	C												
1H-2, 75	2.25	2.28	G	VA																			C	A	C											
1H-3, 75	3.76	3.79	G	VA																					A	C										
1H-CC, 13	4.57	4.60	G	VA																		F			A											
2H-1, 76	5.36	7.17	G	VA			F		R																C											
2H-2, 76	6.87	8.68	G	VA			F							C				F							F											
2H-3, 76	8.38	10.19	G	VA			F							C				F							F											
2H-4, 76	9.89	11.70	M	VA			F							C	C	C									F											
2H-5, 76	11.41	13.22	M	VA			F							C	C	F			F						C											
2H-CC, 14	13.70	15.51	M	VA			F							C					F						C											
3H-1, 76	14.86	16.77	M	VA			F							C											R											
3H-2, 76	16.36	18.10	M	VA			F							C											R											
3H-3, 76	17.70	19.61	M	VA			F							C											R			C								
3H-4, 76	19.21	21.12	M	VA		F	C							C														C	F							
3H-CC, 13	23.53	25.44	M	VA		F	C							C														A	F							
4H-1, 76	24.36	28.48	M	VA		R	C							C	C													C								
4H-3, 76	27.40	31.52	M	VA		R	C							C	C													C								
4H-CC, 14	33.40	37.52	M	VA		R	C							C	C													C								
5H-1, 76	33.86	40.05	M	VA		R	C							C	C													C								
5H-3, 76	36.81	43.00	M	VA		R	C							C	C													C								
5H-6, 76	41.30	47.49	M	A	R	R	C							A														C								
5H-CC, 11	41.98	48.17	M	VA	R	R	C							C	C													A								
6H-1, 76	43.36	50.54	M	VA	R	R	C							C	F																				F	
6H-2, 76	44.87	52.05	M	VA			C							C	F																				F	
6H-3, 76	46.38	53.56	M	VA			C							C	F																				F	
6H-4, 76	47.85	55.03	M	VA			C							C	R																					
6H-4, 76	47.85	55.03	M	VA			C							C	R																					
6H-5, 76	49.36	56.54	M	VA			C							C	F																				F	
6H-6, 76	50.87	58.05	M	VA			C							C	F																				F	
6H-CC, 13	51.20	58.38	M	VA			C							A	R																					
7H-1, 76	52.86	60.43	M	A			C							C	R													C							F	
7H-2, 76	54.38	61.95	M	A			C							C	R					F								C							F	
7H-3, 76	55.89	63.46	M	A			F							C														C							F	
7H-6, 76	60.42	67.99	M	C			C							C														C							R	
7H-7, 45	61.62	69.19	M	C			C							C														C							R	
7H-CC, 14	62.10	69.67	M	VA			C			F				A					C																F	
8H-1, 79	62.39	73.87	M	VA						F	R		A						C									F								
8H-2, 76	63.87	75.35	M	A						R			A						C																	
8H-4, 76	66.69	78.17	M	VA				R		R	R		A						C																	

Table T8 (continued).

Core, section, interval (cm)	Depth (mbsf)	Depth (mcd)	Preservation	Abundance	*Amaurolithus primus*	*Amaurolithus primus/delicatus*	*Calcidiscus macintyrei*	*Calcidiscus premacintyrei*	*Ceratolithus* spp.	*Coccolithus miopelagicus*	*Coronocyclus nitescens*	*Cyclicargolithus abisectus*	*Cyclicargolithus floridanus*	*Discoaster brouweri*	*Discoaster pentaradiatus*	*Discoaster surculus*	*Discoaster tamalis*	*Discoaster triradiatus*	*Discoaster variabilis* gr.	*Discoaster* spp. (5-ray)	*Emiliania huxleyi*	*Gephyrocapsa* (large)	*Gephyrocapsa* (medium)	*Gephyrocapsa* spp. (small)	*Pseudoemiliania lacunosa*	*Reticulofenestra asanoi*	*Reticulofenestra bisecta*	*Reticulofenestra pseudoumbilicus*	*Sphenolithus abies/neoabies*	*Sphenolithus belemnos*	*Sphenolithus ciperoensis*	*Sphenolithus distentus*	*Sphenolithus heteromorphus*	*Sphenolithus predistentus*	*Triquetrorhabdulus rugosus*	*Zygrhabdolithus bijugatus*
8H-CC, 14	69.55	81.03	M	VA				C			F		A						A									F	F							
9H-1, 76	71.86	82.39	M	VA				C			F		A						A									F	F							
9H-2, 76	73.37	83.90	M	VA				C			F		A						A									F	F							
9H-3, 76	74.88	85.41	M	VA				C			C		A						A									F	F				F			
9H-CC, 12	80.34	90.87	M	VA				C			C		A						A									F	F				F			
10H-CC, 15	88.84	102.92	M	VA				R			F		A						A									R					C			
11H-1, 76	90.86	103.79	M	A				R			F		A						A														C			
11H-CC, 11	99.60	112.53	M	VA				R			F		D						C														C			
12H-1, 76	100.36	114.22	M	A							C		A						C														F			
12H-3, 76	103.38	117.24	M	A				?			C		A						C														R			
12H-5, 76	106.40	120.26	M	A							C		A						C														R			
12H-CC, 17	109.63	123.49	M	A							C		A						C														R			
13H-2, 76	111.37	125.74	M	A							C		A						C														F			
13H-3, 76	112.88	127.25	M	A							F		A						C														R			
13H-4, 76	114.39	128.76	M	A							C		A						C														R			
13H-6, 76	117.41	131.78	M	A							C		A						C														R			
13H-CC, 15	118.52	132.89	M	A							C		A						C											R						
14H-CC, 12	128.30	142.67	M	A							C		A						C											R						
15H-3, 76	131.88	146.43	M	A							C		A						C											R						
15H-5, 76	134.90	149.45	M	A							C		A						C																	
15H-CC, 18	137.89	152.44	M	A							C	F	A						C																	
16H-2, 100	140.10	154.93	P	R								F	F																							
16H-CC, 14	141.21	156.04	P	R								R	F																							
17H-1, 75	142.35	157.18	P	F									F																							
17H-2, 75	143.86	158.69	P	F									F																							
17H-3, 75	145.37	160.20	P	F								F	F																							
17H-4, 75	146.89	161.72	P	F									F																							
17H-5, 75	148.39	163.22	P	F									F																							
17H-6, 75	149.90	164.73	P	F									F																							
17H-CC, 11	151.11	165.94	P	F									F																							
18H-1, 75	151.85	166.68	P	F									R																							
18H-2, 75	153.36	168.19	P	F									R																							
18H-3, 75	154.87	169.70	P	F									R																							
18H-4, 75	156.35	171.18	P	C									C														R									F
18H-4, 2	155.62	170.45	M	A							R	F	A														R					F		F		R
18H-4, 3	155.63	170.46	M	A							R	F	A														R					F		F		R
18H-4, 25	155.85	170.68	M	A							R	F	A														R					F		F		R
18H-6, 75	159.36	174.19	P	F																																
18H-CC, 16	160.59	175.42	P	R									R																							
19H-CC, 21	170.42	185.25	P	R									R																							

Table T8 (continued).

Core, section, interval (cm)	Depth (mbsf)	Depth (mcd)	Preservation	Abundance	*Amaurolithus primus*	*Amaurolithus primus/delicatus*	*Calcidiscus macintyrei*	*Calcidiscus premacintyrei*	*Ceratolithus* spp.	*Coccolithus miopelagicus*	*Coronocyclus nitescens*	*Cyclicargolithus abisectus*	*Cyclicargolithus floridanus*	*Discoaster brouweri*	*Discoaster pentaradiatus*	*Discoaster surculus*	*Discoaster tamalis*	*Discoaster triradiatus*	*Discoaster variabilis* gr.	*Discoaster* spp. (5-ray)	*Emiliania huxleyi*	*Gephyrocapsa* (large)	*Gephyrocapsa* (medium)	*Gephyrocapsa* spp. (small)	*Pseudoemiliania lacunosa*	*Reticulofenestra asanoi*	*Reticulofenestra bisecta*	*Reticulofenestra pseudoumbilicus*	*Sphenolithus abies/neoabies*	*Sphenolithus belemnos*	*Sphenolithus ciperoensis*	*Sphenolithus distentus*	*Sphenolithus heteromorphus*	*Sphenolithus predistentus*	*Triquetrorhabdulus rugosus*	*Zygrhabdolithus bijugatus*
20H-CC, 17	173.35	188.47	P	R									R																							
21X-CC, 34	177.47	192.59		B								R	R																							
22X-1, 75	183.55	198.67		B																																
22X-2, 75	185.06	200.18		B																																
22X-3, 75	186.56	201.68	P	F								F																								R
22X-5, 75	189.58	204.70	P	R																							R					R		R		
22X-7, 40	191.58	206.70	P	R								F															R				R	R		R		R
22X-CC, 35	191.53	206.65	C	M							F	F	C														F				R	R		R		R
23X-1, 65	193.15	208.27	M	A								F	C														R					R				
23X-2, 65	194.67	209.79	M	A								F	C														R				F	F				
23X-CC, 32	200.95	216.07	M	C								F	C														R				R	R		R		R
24X-CC, 18	207.95	223.07	M	C								C	C														F				R	R				
202-1236C-																																				
4H-1, 80	32.10	37.17	M	VA		R	C							C	F													A	F							
4H-2, 80	33.61	38.68	M	VA		R	C		?					C	F													A	F							
4H-4, 80	36.63	41.70	M	VA		R	C							C	F													A	F							
4H-7, 40	40.57	45.64	M	VA		R	C							C	F													A	F							
5H-1, 80	41.60	47.55	M	VA	R	R	C							C	F													C								
5H-2, 80	43.12	49.07	M	VA	R	R	C							C	F																				F	
5H-3, 80	44.63	50.58	M	VA	R		C							C																					R	
5H-4, 80	46.14	52.09	M	VA			C							C																					F	
5H-5, 80	47.65	53.60	M	VA			C							C																					F	
5H-7, 40	50.27	56.22	M	VA			C							C																					F	
6H-5, 115	57.49	64.44	M	A			F			R	F		C						C									C								
6H-6, 29	58.14	65.09	M	C						R	F		C						C									C								

Notes: Preservation: G = good, M = moderate, P = poor. Abundance: VA = very abundant, A = abundant, C = common, F = few, R = rare, B = barren. ? = unknown.

Table T9. Distribution of foraminifers, Hole 1236A.

Core, section	Depth (mbsf)	Depth (mcd)	Preparation	Preservation	Abundance	Benthic/planktonic foraminifers (%)	*Catapsydrax dissimilis*	*Catapsydrax unicavus*	*Dentoglobigerina altispira*	*Globigerinella aequilateris*	*Globigerinoides extremus*	*Globigerinoides trilobus*	*Globigerina bulloides*	*Globoquadrina dehiscens*	*Globorotalia conoidea*	*Globorotalia conomiozea*	*Globorotalia crassaformis*	*Globorotalia hirsuta*	*Globorotalia inflata*	*Globorotalia margaritae*	*Globorotalia plesiotumida*	*Globigerinoides ruber*	*Globorotalia scitula*	*Globorotalia tosaensis*	*Globorotalia truncatulinoides*	*Globorotalia tumida*	*Globoturborotalia angulisuturalis*	*Globoturborotalia nepenthes*	*Neogloboquadrina dutertrei*	*Orbulina suturalis*	*Orbulina universa*	*Praeorbulina sicana*	*Praeorbulina transitoria*	*Sphaeroidinella dehiscens*	*Sphaeroidinellopsis kochi*	*Sphaeroidinellopsis seminula*
202-1236A-																																				
1H-CC	4.57	4.60	S	G	A	<1				R			C					R	R			C	F	F	C	C			F		C			F		
2H-CC	13.70	15.51	S	G	A	<1				R	F		C				F	R				C	R	F		C			C		C					F
3H-CC	23.53	25.44	S	M	A	<1			F		R		F								F	F				C		C			C				F	F
4H-CC	33.40	37.52	S	M	A	<1			F		F		F		F	F				F	F	F	R					C			C				F	F
5H-CC	41.98	48.17	S	M	A	<1			F		R		F								F		R					C			A				F	F
6H-CC	51.20	58.38	S	M	A	<1			F		R		F	R		F					F							F			C				F	F
7H-CC	62.10	69.67	S	M	A	<1			F				F	F														F		F					F	F
8H-CC	69.55	81.03	S	M	A	<1			F				F	F									R							R					F	F
9H-CC	80.34	90.87	S	M	A	<1			F					F																R		R	R			F
10H-CC	88.84	102.92	S	M	A	<1			F					F									R									R	R			F
11H-CC	99.60	112.53	S	M	C	<1			F					F									R									R	R			R
12H-CC	109.63	123.49	S	M	C	<1	F		F					F	R																					
13H-CC	118.52	132.89	S	M	C	<1	F	F	F					F																						
14H-CC	128.30	142.67	S	M	C	<1	F	F	F					R																						
15H-CC	137.89	152.44	S	M	C	5	F	F	F					F																						
16H-CC	141.21	156.04	S	P	R	5	F	F	F			F		R																						
17H-CC	151.11	165.94	S	P	F	5	F	F	F			F		R																						
18H-CC	160.59	175.42	S	P	F	5	F	F	F			F		R													R									
19H-CC	170.42	185.25	S	P	F	5	F	F	F			F															F									
20H-CC	173.35	188.47	S	VP	R	5	R	R	R			R															R									
21H-CC	177.47	192.59	C	VP	R	5		R	R																											
22H-CC	191.53	206.65	C	VP	R	5			R																											
23H-CC	200.95	216.07	C	P	F	20	F	F	F																											
24H-CC	207.95	223.07	C	B	B	B																														

Notes: Preparation: S = sieve, C = Calgon. Preservation: B = barren, G = good, M = moderate, P = poor, VP = very poor. Abundance: A = abundant, C = common, F = few, R = rare.

Table T10. Determinations of polarity chron boundaries, Site 1236.

Polarity interval	Core, section, interval (cm)	Depth		Comments	Core, section, interval (cm)	Depth		Core, section, interval (cm)	Depth		Polarity chron interpretation	Age (Ma)
		(mbsf)	(mcd)			(mbsf)	(mcd)		(mbsf)	(mcd)		
	202-1236A-				202-1236B-			202-1236C-				
Upper	1H-2, 80	2.30	2.33	Poorly defined	1H-2, 40	1.91	1.91				C1n (b) Matuyama/Brunhes	
Middle	1H-2, 100	2.50	2.53		1H-2, 75	2.26	2.26				C1n (b) Matuyama/Brunhes	0.780
Lower	1H-2, 115	2.65	2.68		1H-2, 110	2.61	2.61				C1n (b) Matuyama/Brunhes	
Upper	1H-2, 140	2.90	2.93	At section break	1H-3, 10	3.12	3.12				C1r.1n (t) Jaramillo	
Middle	1H-3, 15	3.16	3.19		1H-3, 25	3.27	3.27				C1r.1n (t) Jaramillo	0.990
Lower	1H-3, 25	3.26	3.29		1H-3, 40	3.42	3.42				C1r.1n (t) Jaramillo	
Upper	1H-3, 105	4.06	4.09		1H-3, 50	3.52	3.52				C1r.1n (b) Jaramillo	
Middle	1H-3, 115	4.16	4.19		1H-3, 60	3.62	3.62				C1r.1n (b) Jaramillo	1.070
Lower	1H-3, 125	4.26	4.29	Near core bottom	1H-3, 85	3.87	3.87				C1r.1n (b) Jaramillo	
Upper					1H-4, 120	5.73	5.73	1H-2, 30	4.61	5.17	C2n (t) Olduvai	
Middle					1H-5, 20	6.24	6.24	1H-2, 105	5.36	5.92	C2n (t) Olduvai	1.770
Lower					1H-5, 70	6.74	6.74	1H-3, 35	6.17	6.73	C2n (t) Olduvai	
Upper	2H-1, 110	5.70	7.51		1H-5, 105	7.09	7.09	1H-3, 120	7.02	7.58	C2n (b) Olduvai	
Middle	2H-1, 125	5.85	7.66		1H-5, 140	7.44	7.44	1H-4, 10	7.43	7.99	C2n (b) Olduvai	1.950
Lower	2H-1, 140	6.00	7.81		1H-6, 25	7.80	7.80	1H-4, 35	7.68	8.24	C2n (b) Olduvai	
Upper	2H-4, 30	9.43	11.24		2H-2, 30	10.61	10.88	1H-5, 30	9.14	9.70	C2An.1n (t) Gauss/Matuyama	
Middle	2H-4, 65	9.78	11.59		2H-2, 60	10.91	11.18	1H-5, 115	9.99	10.55	C2An.1n (t) Gauss/Matuyama	2.581
Lower	2H-4, 105	10.18	11.99		2H-2, 90	11.21	11.48	1H-6, 50	10.85	11.41	C2An.1n (t) Gauss/Matuyama	

Note: (b) = bottom, (t) = top.

Table T11. Paleomagnetic age control points based on polarity chron interpretation, Site 1236.

Polarity chron interpretation	Age (Ma)	Depth (mcd)	Error (± m)
C1n	0.39	1.2	1.2
C1r	1.28	4.4	2.1
C2n	1.86	7.0	0.5
C2r	2.26	9.3	1.9
C2An	3.08	14.4	3.2
C2Ar	3.88	19.8	2.2
C3n	4.71	27.6	5.6
C3r	5.56	36.5	3.4
C3An	6.23	43.3	3.4
C3Ar/C3Bn/C3Br	7.18	49.8	3.0
C4n	7.75	54.1	1.3
C4r/C4An/C4Ar	8.91	60.2	4.8
C5n	10.34	67.2	2.2
C5r	11.44	70.9	1.5
C5An	12.17	74.4	2.0
C5Ar	12.70	78.4	2.0
C5AAn/C5AAr/C5ABn/C5ABr/C5ACn	13.35	83.2	2.8
C5ACn/C5ACr/C5ADn	14.16	89.3	3.3

Table T12. Interstitial water geochemical data, Hole 1236A.

Core, section, interval (cm)	Depth		pH	Alkalinity (mM)	Salinity	Cl^- (mM)	Na^+ (mM)	SO_4^{2-} (mM)	HPO_4^{2-} (μM)	NH_4^+ (μM)	H_4SiO_4 (μM)	Mn^{2+} (μM)	Fe^{2+} (μM)	Ca^{2+} (mM)	Mg^{2+} (mM)	B (μM)	Sr^{2+} (μM)	Ba^{2+} (μM)	Li^+ (μM)	K^+ (mM)
	(mbsf)	(mcd)																		
202-1236A-																				
1H-2, 140–150	2.90	2.93	7.39	2.57	34.0	553	473	26.0	2.0	BDL	210	2.3	BDL	11.0	51.3	433	103	0.6	25	10.2
2H-3, 145–150	9.07	10.88	7.35	2.46	34.0	560	483	27.2	0.9	3.2	350	0.5	BDL	12.2	49.5	425	125	0.7	25	10.1
3H-3, 145–150	18.39	20.30	7.04	2.20	34.0	561	481	26.3	1.3	BDL	389	BDL	0.6	12.1	50.3	423	126	0.4	25	9.9
4H-3, 145–150	28.09	32.21	7.50	2.35	34.0	564	479	27.0	0.7	2.8	414	0.6	BDL	12.9	52.6	397	112	0.5	25	10.2
5H-3, 140–150	37.45	43.64	7.47	2.24	34.0	570	492	26.7	0.9	3.3	429	1.0	BDL	12.1	49.8	410	106	0.3	24	9.8
6H-3, 140–150	47.02	54.20	7.42	2.29	35.0	563	480	26.6	0.8	BDL	449	1.3	BDL	12.3	51.9	399	102	0.3	26	10.0
7H-3, 140–150	56.53	64.10	7.36	2.61	35.0	564	481	27.0	0.7	2.6	455	1.9	BDL	12.4	52.6	397	97	0.3	26	10.1
8H-3, 122–132	65.84	77.32	7.39	2.17	35.0	562	479	26.6	0.7	BDL	480	3.8	BDL	12.1	52.2	399	95	0.3	27	10.2
9H-3, 140–150	75.52	86.05	7.36	2.34	36.0	563	484	28.0	0.7	BDL	492	2.2	BDL	11.8	51.9	392	93	0.7	26	10.0
10H-3, 140–150	85.01	99.09	7.43	2.46	35.0	561	483	27.9	2.0	BDL	387	1.9	BDL	11.6	51.3	397	90	0.3	25	10.0
11H-3, 140–150	94.52	107.45	7.39	2.23	35.0	560	485	27.7	0.6	BDL	266	2.0	BDL	11.5	49.7	404	93	0.3	27	9.8
12H-3, 140–150	104.02	117.88	7.53	2.26	34.0	566	486	26.7	0.5	BDL	218	1.7	BDL	11.5	51.2	400	91	0.3	26	10.1
13H-3, 140–150	113.52	127.89	7.46	2.29	35.0	563	476	26.1	0.6	BDL	206	1.3	BDL	12.0	53.7	382	91	0.3	26	10.2
14H-3, 140–150	123.03	137.40	7.51	2.28	36.0	565	483	26.5	0.7	BDL	200	BDL	BDL	11.8	51.8	391	92	BDL	26	10.2
15H-3, 140–150	132.52	147.07	7.53	2.27	36.0	564	481	26.9	0.6	BDL	198	BDL	0.3	11.9	52.7	386	90	0.3	27	10.1
17H-3, 145–150	146.07	160.90	7.56	2.33	36.0	568	483	27.4	1.0	5.4	204	BDL	BDL	11.6	51.9	386	91	0.3	26	10.3
18H-3, 140–150	155.52	170.35	7.61	2.29	36.0	573	487	26.0	1.3	4.7	262	BDL	BDL	11.4	51.4	377	88	0.2	25	11.0
19H-3, 140–150	165.02	179.85	7.58	2.28	36.0	564	475	24.3	0.7	4.4	196	BDL	BDL	11.8	52.9	384	89	BDL	26	10.2
21X-2, 140–150	176.01	191.13	7.64	2.57	36.0	565	476	23.6	0.7	4.7	352	2.2	0.4	14.0	50.0	377	91	0.3	27	10.9
22X-3, 140–150	187.21	202.33	7.64	2.09	36.0	565	483	27.0	2.0	BDL	645	7.1	BDL	13.5	50.3	381	98	0.3	28	10.4
23X-3, 140–150	196.92	212.04	7.63	1.40	36.0	566	481	26.8	0.7	7.7	455	8.9	BDL	14.6	50.1	385	105	0.3	28	11.0
24X-2, 140–150	205.11	220.23	7.91	1.14	36.0	568	487	26.7	1.6	3.0	231	6.5	BDL	14.2	48.2	284	98	0.4	27	10.9

Notes: BDL = below detection limit (NH_4^+ = 2.2 μM, Mn^{2+} = 0.1 μM, Fe^{2+} = 0.3 μM, Ba^{2+} = 0.2 μM).

Table T13. Inorganic carbon, calcium carbonate, and total carbon concentrations in sediments, Hole 1236A. (See table note. Continued on next page.)

Core, section, interval (cm)	Depth		IC	$CaCO_3$	TC
	(mbsf)	(mcd)	(wt%)	(wt%)	(wt%)
202-1236A-					
1H-1, 74-75	0.74	0.77	11.28	93.9	
1H-2, 74-75	2.24	2.27	11.31	94.2	
1H-3, 74-75	3.75	3.78	11.37	94.7	11.33
2H-1, 74-75	5.34	7.15	10.95	91.2	
2H-2, 74-75	6.85	8.66	11.05	92.0	
2H-3, 74-75	8.36	10.17	11.43	95.2	11.49
2H-4, 74-75	9.87	11.68	11.47	95.5	
2H-5, 74-75	11.39	13.20	11.56	96.3	
2H-6, 74-75	12.89	14.70	11.51	96.0	
3H-1, 74-75	14.84	16.75	11.52	96.0	
3H-2, 74-75	16.17	18.08	11.37	94.7	
3H-3, 74-75	17.68	19.59	11.52	96.0	11.42
3H-4, 74-75	19.19	21.10	11.55	96.2	
3H-5, 74-75	20.70	22.61	11.50	95.8	
3H-6, 74-75	22.20	24.11	11.49	95.7	
4H-1, 74-75	24.34	28.46	11.50	95.8	
4H-2, 74-75	25.86	29.98	11.56	96.3	
4H-3, 74-75	27.38	31.50	11.57	96.4	11.46
4H-4, 74-75	28.88	33.00	11.63	96.9	
4H-5, 74-75	30.40	34.52	11.60	96.7	
4H-6, 74-75	31.91	36.03	11.56	96.3	
5H-1, 74-75	33.84	40.03	11.63	96.9	
5H-2, 74-75	35.27	41.46	11.13	92.7	
5H-3, 74-75	36.79	42.98	11.61	96.7	11.51
5H-4, 74-75	38.26	44.45	11.61	96.7	
5H-5, 74-75	39.77	45.96	11.54	96.1	
5H-6, 74-75	41.28	47.47	11.62	96.8	
6H-1, 74-75	43.34	50.52	11.65	97.0	
6H-2, 74-75	44.85	52.03	11.41	95.1	
6H-3, 74-75	46.36	53.54	11.50	95.8	11.45
6H-4, 74-75	47.83	55.01	11.52	96.0	
6H-5, 74-75	49.34	56.52	11.45	95.4	
6H-6, 74-75	50.85	58.03	11.40	95.0	
7H-1, 74-75	52.84	60.41	10.99	91.5	
7H-2, 74-75	54.36	61.93	11.35	94.5	
7H-3, 74-75	55.87	63.44	11.33	94.3	11.48
7H-4, 74-75	57.37	64.94	11.68	97.3	
7H-5, 74-75	58.88	66.45	11.57	96.4	
7H-6, 74-75	60.40	67.97	11.44	95.3	
7H-7, 20-21	61.37	68.94	11.44	95.3	
8H-1, 74-75	62.34	73.82	11.49	95.7	
8H-2, 74-75	63.85	75.33	11.54	96.1	
8H-3, 74-75	65.36	76.84	11.56	96.3	11.39
8H-4, 74-75	66.67	78.15	11.47	95.5	
8H-5, 74-75	68.18	79.66	11.47	95.6	
9H-1, 74-75	71.84	82.37	11.27	93.8	
9H-2, 74-75	73.35	83.88	11.47	95.5	
9H-3, 74-75	74.86	85.39	11.31	94.2	11.22
9H-4, 74-75	76.37	86.90	11.54	96.1	
9H-5, 74-75	77.88	88.41	11.60	96.7	
9H-6, 74-75	79.38	89.91	11.41	95.0	
10H-1, 74-75	81.34	95.42	11.53	96.0	
10H-2, 74-75	82.85	96.93	11.59	96.5	
10H-3, 74-75	84.35	98.43	11.52	96.0	11.46
10H-4, 74-75	85.86	99.94	11.65	97.0	
10H-5, 74-75	87.36	101.44	11.57	96.4	
10H-6, 20-21	88.33	102.41	11.59	96.5	
11H-1, 74-75	90.84	103.77	11.58	96.4	
11H-2, 74-75	92.35	105.28	8.73	72.7	
11H-3, 74-75	93.86	106.79	11.47	95.5	11.35
11H-4, 74-75	95.37	108.30	11.55	96.2	
11H-5, 74-75	96.88	109.81	11.64	97.0	
11H-6, 74-75	98.39	111.32	11.56	96.3	
12H-1, 74-75	100.34	114.20	11.52	96.0	
12H-2, 74-75	101.85	115.71	11.60	96.6	

Table T13 (continued).

Core, section, interval (cm)	Depth		IC (wt%)	$CaCO_3$ (wt%)	TC (wt%)
	(mbsf)	(mcd)			
12H-3, 74-75	103.36	117.22	10.54	87.8	10.92
12H-4, 74-75	104.87	118.73	11.61	96.7	
12H-5, 74-75	106.38	120.24	11.73	97.7	
12H-6, 74-75	107.89	121.75	11.73	97.7	
12H-7, 20-21	108.86	122.72	11.71	97.5	
13H-1, 74-75	109.84	124.21	11.66	97.1	
13H-2, 74-75	111.35	125.72	11.67	97.2	
13H-3, 74-75	112.86	127.23	11.75	97.9	11.69
13H-4, 74-75	114.37	128.74	11.64	97.0	
13H-6, 74-75	117.39	131.76	11.70	97.5	
13H-7, 40-41	118.06	132.43	11.72	97.6	
14H-1, 120-121	119.80	134.17	11.66	97.1	
14H-2, 100-101	121.11	135.48	11.74	97.8	11.72
14H-3, 100-101	122.63	137.00	11.64	97.0	
14H-4, 74-75	123.88	138.25	11.70	97.5	
14H-5, 74-75	125.39	139.76	11.71	97.5	
14H-6, 74-75	126.90	141.27	11.68	97.3	
14H-7, 20-21	127.87	142.24	11.77	98.0	
15H-2, 74-75	130.35	144.90	11.62	96.8	
15H-3, 74-75	131.86	146.41	11.73	97.7	11.70
15H-4, 74-75	133.37	147.92	11.63	96.8	
15H-5, 74-75	134.88	149.43	11.72	97.7	
15H-6, 74-75	136.38	150.93	11.80	98.3	
15H-7, 20-21	137.35	151.90	11.56	96.3	
17H-1, 74-75	142.34	157.17	11.64	97.0	
17H-2, 74-75	143.85	158.68	11.59	96.6	
17H-3, 74-75	145.36	160.19	11.59	96.6	11.47
17H-4, 74-75	146.88	161.71	11.68	97.3	
17H-5, 74-75	148.38	163.21	11.66	97.1	
17H-6, 74-75	149.89	164.72	11.72	97.6	
17H-7, 20-21	150.66	165.49	11.71	97.5	
18H-1, 74-75	151.84	166.67	11.70	97.5	
18H-2, 74-75	153.35	168.18	11.81	98.4	
18H-3, 74-75	154.86	169.69	11.77	98.0	11.72
18H-4, 11-12	155.71	170.54	8.61	71.7	
18H-4, 74-75	156.34	171.17	11.71	97.5	
18H-5, 74-75	157.85	172.68	11.82	98.5	
18H-6, 74-75	159.35	174.18	11.82	98.5	
18H-7, 20-21	160.12	174.95	11.87	98.8	
19H-1, 74-75	161.34	176.17	11.63	96.9	
19H-2, 74-75	162.85	177.68	11.65	97.1	
19H-3, 74-75	164.36	179.19	11.67	97.2	11.58
19H-4, 74-75	165.87	180.70	11.82	98.4	
19H-5, 74-75	167.37	182.20	11.67	97.2	
19H-6, 74-75	168.89	183.72	11.68	97.3	
19H-7, 20-21	169.86	184.69	11.69	97.4	
20H-2, 74-75	171.46	186.58	11.59	96.5	
20H-3, 74-75	172.72	188.04	11.54	96.2	11.56
21X-1, 74-75	173.84	188.96	11.20	93.3	
21X-2, 30-31	174.91	190.03	11.59	96.5	
21X-3, 20-21	176.32	191.44	11.22	93.4	
22X-1, 74-75	183.54	198.66	10.37	86.4	
22X-2, 74-75	185.05	200.17	9.45	78.7	
22X-3, 74-75	186.55	201.67	9.19	76.6	9.58
22X-1, 30-31	187.62	202.74	5.89	49.0	5.93
22X-4, 74-75	188.06	203.18	10.81	90.0	10.85
22X-5, 74-75	189.57	204.69	7.96	66.3	
22X-6, 74-75	191.08	206.20	8.13	67.8	8.16

Note: IC = inorganic carbon, TC = total carbon.

Table T14. Age-depth model, linear sedimentation rates, and mass accumulation rates, Site 1236.

Age (Ma)	Depth (mcd)	LSR (mcd/m.y.)	mcd growth factor	Corrected LSR (m/m.y.)	Dry density (g/cm^3)	$CaCO_3$ average concentration (wt%)	Total MAR (g/cm^2/k.y.)	$CaCO_3$ MAR (g/cm^2/k.y.)	Noncarbonate MAR (g/cm^2/k.y.)
0.0	0.0								
1.0	3.4	3.4	1.14	3.0	0.89	94.1	0.27	0.25	0.016
2.0	8.0	4.6	1.14	4.0	1.01	93.0	0.41	0.38	0.029
3.0	14.0	6.0	1.14	5.2	1.03	94.8	0.54	0.51	0.028
4.0	21.3	7.3	1.14	6.4	1.04	95.7	0.66	0.63	0.028
5.0	30.7	9.5	1.14	8.3	1.02	95.9	0.85	0.81	0.035
6.0	41.0	10.3	1.14	9.0	1.04	96.6	0.94	0.90	0.032
7.0	49.8	8.7	1.14	7.7	1.07	95.8	0.82	0.78	0.034
8.0	55.3	5.5	1.14	4.9	1.04	96.0	0.51	0.48	0.020
9.0	60.0	4.7	1.14	4.1	0.98	95.2	0.40	0.38	0.020
10.0	64.4	4.4	1.14	3.9	0.99	93.5	0.38	0.36	0.025
11.0	68.7	4.3	1.14	3.8	0.96	96.3	0.36	0.35	0.013
12.0	73.8	5.0	1.14	4.4	0.93	95.5	0.41	0.39	0.018
13.0	80.6	6.9	1.14	6.0	1.02	95.9	0.62	0.59	0.025
14.0	88.3	7.6	1.14	6.7	1.04	94.9	0.70	0.66	0.035
15.0	97.3	9.0	1.14	7.9	1.11	96.1	0.87	0.84	0.034
16.0	107.7	10.4	1.14	9.2	1.06	96.3	0.97	0.93	0.036
17.0	118.5	10.8	1.14	9.4	1.07	95.0	1.01	0.95	0.051
18.0	129.2	10.8	1.14	9.4	1.26	97.4	1.19	1.16	0.031
19.0	140.0	10.8	1.00	10.8	1.30	97.4	1.40	1.36	0.036
20.0	150.8	10.8	1.00	10.8	1.28	97.4	1.38	1.34	0.036
21.0	161.6	10.8	1.00	10.8	1.32	96.9	1.42	1.38	0.044
22.0	172.4	10.9	1.00	10.9	1.32	97.6	1.44	1.41	0.034
23.0	183.5	11.1	1.00	11.1	1.43	97.8	1.58	1.55	0.034
24.0	194.7	11.2	1.00	11.2	1.36	95.8	1.52	1.45	0.064
25.0	206.0	11.3	1.00	11.3	1.29	79.6	1.46	1.16	0.298
26.0	217.4	11.3	1.00	11.3	1.09	67.7	1.24	0.84	0.400

Notes: LSR = linear sedimentation rate, MAR = mass accumulation rate. This table is also available in **ASCII**.